

Aerodynamic Characterization of a Multi-Fan Wind Generator

Experimental Study using PIV

Georgia-Silvia-Maria Bălan

Aerodynamic Characterization of a Multi-Fan Wind Generator

Experimental Study using PIV

by

Georgia-Silvia-Maria Bălan

to obtain the degree of Master of Science

at the Delft University of Technology,

to be defended publicly on Monday March 10, 2025 at 09:00 AM.

Student number:	5863430	
Project duration:	June 3, 2024 – March 10, 2025	
Thesis committee:	Chair: Dr. W. Yu	TU Delft
	Examiner: Dr. ir. B.W. van Oudheusden	TU Delft
	Supervisor: Dr. A. Sciacchitano	TU Delft
	Supervisor: Ir. K. Sripathy	TU Delft

An electronic version of this thesis is available at <http://repository.tudelft.nl/>.

Acknowledgments

This project fulfilled a small dream of mine from 2020, my 3rd year of bachelor's. As part of a course, we simulated a research grant application, designing our own project. The idea came naturally: we had spent three years wishing the closed-loop wind tunnel in our faculty's yard still worked. Since it did not, we proposed building a modern aerodynamic research facility. My role was to select the flow measurement equipment, and that is when I came across PIV. The idea of using a laser to measure velocity felt almost Sci-Fi, and I wondered what it would be like to conduct those measurements myself. However, at that time, it felt out of reach. Until my mother encouraged me to pursue a master's in the Netherlands and experience academia there. I am the most grateful for her love and support. And for my little sister's care and motivation when I needed it the most. Without my girls, frankly, I would not be here.

Being excited to work on this project and coming full circle was one thing, but being part of an encouraging and knowledgeable team made the experience truly enriching. I am deeply grateful to them all. Being supervised by dr. Andrea Sciacchitano and Kiran was an honor. Their guidance not only clarified my understanding and helped me paving the way forward, but also fueled me with confidence when it felt like it was going out. Smooth access to the PIV servers would not have been possible without Gert-Jan, who always found time to help me and my spontaneous technical issues, even though he was fully-booked by bigger problems all the time. During the time spent in the workshop of the HLS, I got to interact more with Peter Duyndam, Dennis Bruikman, and Frits Donker Duyvis, who were always happy to help me, and who probably heard the fans running as much as I did (not the most pleasant sound). From the LSL, Theo Michelis and Stefan Bernardy provided great, quick support for last-minute situations. During the two weeks of measurements, many stopped by to show their curiosity and support, making the dark, foggy W-tunnel room more lively. Last but not least, Jayant, the friend I made along the way, who introduced me to Arduino and taught me how to solder (two things I certainly did not have on my 2024 vision board).

I am deeply grateful to George for standing by me through every high and low, offering the unwavering support of a true best friend. I am the happiest to have had Pin and Matti by my side, sharing good laughs and core memories. I could not have asked for a better study buddy than Madalina, and the library and coffee star could not have asked for a more cheerier duo than us. A heartfelt thank you to Stefana, Prisi, Gusteras, and all my friends here and back home for their encouragement, positivity, and selfless care, not just this past year, but always.

Nu in ultimul rand, un sincer multumesc familiei mele pentru increderea si sprijinul neconditionat. Vreau sa ii multumesc in special mamaitei mele pentru energia, iubirea si intelepciunea pe care mi le-a transmis neincetat. De fiecare data, cele mai bune decizii le-am luat dupa o conversatie cu ea, iar acest proiect nu face exceptie.

This project was a true team effort, and I enjoyed being part of it. Thank you. :)

*Georgia-Silvia-Maria Balan
Delft, February 2025*

Abstract

Understanding atmospheric motion is crucial for analysing wind-structure interactions, particularly within the Atmospheric Boundary Layer (ABL). Traditionally, wind tunnels have simulated unsteady ABL conditions using active and passive devices. Recently, multi-fan wind generators have emerged as a flexible, cost-effective alternative, allowing independent fan control to replicate wind conditions the wind turbines, airborne devices or civil structures are subjected to.

This thesis investigates the capability of a newly manufactured 3 x 3 multi-fan wind generator to produce idealized uniform flow, linear shear flow profiles, and streamwise sinusoidal gusts. The system consists of off-the-shelf computer fans, controlled via open-source software, offering a low-cost and adaptable approach. Particle Image Velocimetry (PIV) measurements show a 96% uniform core region with 11.5% turbulence intensity 1 m downstream from the system. There, the area of the core is reduced to 1/9 of the system's area due to the outer shear layer. The system struggles to replicate linear wind shear, but can generate oscillatory gusts at 0.2 Hz, 0.4 Hz and 0.8 Hz, corresponding to the operating frequency of the fans. Further improvements should focus on extending the configuration to maintain a larger core region, and on reducing swirl dynamics and recirculation to enhance flow quality for wind engineering applications.

Contents

Acknowledgments	i
Abstract	ii
Nomenclature	x
1 Introduction	1
2 Literature Review	3
2.1 An overview of the unsteady wind flow within the ABL	3
2.1.1 Wind shear	3
2.1.2 Gust	4
2.1.3 Turbulence Intensity	5
2.2 Wind tunnels: passive and active methods for wind shear and gust generation	6
2.2.1 Experimental methods for generating unsteady wind shear inflow	6
2.2.2 Experimental generation of gusts	9
2.3 Multi-fan array wind generators	9
2.4 Particle Image Velocimetry	18
2.4.1 Principle of PIV	18
2.4.2 Planar & Stereo PIV	19
2.5 Research questions & Research objectives	20
3 Methodology	21
3.1 Multi-fan System Characteristics & Control	21
3.1.1 Fan & Unit characteristics	21
3.1.2 PWM control with Arduino	23
3.2 Test cases	24
3.2.1 Uniform flow	24
3.2.2 Linear shear flow	24
3.2.3 Gust	25
3.3 Experiment Setup	25
3.3.1 Measurement planes	26
3.3.2 Planar PIV setup	27
3.3.3 Stereo PIV setup	29
3.3.4 Image acquisition parameters & Test matrix	31
3.4 Data processing & analysis tools	32
3.4.1 Data processing: DaVis 8	32
3.4.2 Data analysis	32
4 Results	34
4.1 Uniform flow	34
4.1.1 Vertical streamwise plane	34
4.1.2 Cross-stream planes	39
4.1.3 Discussion	43
4.2 Linear shear flow	44
4.2.1 Baseline 1: 40 % duty cycle	44
4.2.2 Baseline 2: 70 % duty cycle	46
4.2.3 Discussion	49
4.3 Gust	51
4.3.1 Time evolution of the streamwise velocity component	51
4.3.2 Power Spectral Density	55

4.3.3 Discussion	56
4.4 A-posteriori uncertainty quantification between planar and stereo PIV measurements	58
5 Conclusions & Outlook	59
5.1 Conclusions	59
5.2 Limitations, recommendations & outlook	60
Bibliography	61
A Electrical Installation	64
A.1 Circuit diagram	64
A.2 Current & power consumption	65
B Multi-fan System Control	66
B.1 Arduino Sketch for Constant Duty Cycle Control	66
B.2 Sine Wave Definition & Arduino Sketch for Oscillating Duty Cycle Control	69
C Preliminary Speed Approximation	74
D Uniform field results	75
D.1 Vertical streamwise plane	75
D.2 Cross-stream planes	77

List of Figures

2.1	The structure of the troposphere (a) and the ABL (b)	3
2.2	Example of extreme operating gust [20]	5
2.3	Turbulence intensity for the normal turbulence model [20]	5
2.4	Different passive methods of generating unsteady ABL profiles	6
2.5	BLWT configurations: surface elements and spires (a) and wooden rods grid (b)	7
2.6	Wind tunnel jet grid section [28]	7
2.7	Mean velocity profiles that follow a prescribed power law (a) and a prescribed linear function (b) [28]	8
2.8	Turbulence intensity profiles after adding (a) LEGO surface and (b) barrier-plate [28]	8
2.9	Examples of different gust generating devices	9
2.10	The multi-fan wind tunnel setup [14]	10
2.11	Mean wind profiles for a shear flow developed in the tunnel ([14])	10
2.12	Measured and target profiles of mean streamwise velocity, U , turbulence intensity, I_u , and turbulence scale, L_u , obtained by (a) power spectrum modification method and (b) time lag modification method [14]	11
2.13	The multi-fan full-scale facility at the Insurance Institute for Business & Home Safety [15]	11
2.14	The multi-fan system with swivel plates at the Tianjin Key Laboratory of Process Measurement and Control [16]	11
2.15	The multi-fan wind tunnel of State Key Laboratory of Disaster Reduction in Civil Engineering at Tongji University, Shanghai, China (a) and the schematics of the facility (b) [12]	12
2.16	The sinusoidal streamwise gust time history (1) and the corresponding Fourier amplitude spectrum (b) at $U = 10$ m/s, $\sigma = 0.2$, $f = 0.3$ Hz [12]	12
2.17	The lift time history (a) and the corresponding PSD (b) at $U = 10$ m/s, $\sigma = 0.2$	12
2.18	The multi-fan system developed by Johnson & Jacob [17] (a) and the control schematics	13
2.19	Measured mean velocity profiles generated by (a) switching the banks from 0 V to 6 V one by one and (b) adjusting the fans manually (6-6-5-4- v) to generate a linear shear flow [17]	14
2.20	Velocity response to a 2 s ramp up (a) and to turn off (b) [17]	14
2.21	Measured velocity at a low operating frequency (not mentioned) (a) and a high operating frequency of the fans (b) [17]	14
2.22	The multi-fan system of MAV Lab and the ProCap system [13]	15
2.23	The grid of thermistor-based sensors used for the velocity measurement [13]	15
2.24	The mean velocity field measured with (a) ProCap and (b) thermistor-based sensors [13]	15
2.25	The small fan-array wind generator used in [33]	16
2.26	Planar PIV measurements at 100% and 50% duty cycle. Contour plots colored by normalized mean streamwise velocity (first row), normalized mean-squared turbulent velocity (second row), and turbulence intensity (third row) [33]	16
2.27	Contour plots of the near field (a) and far field (b), as assessed by [33]	16
2.28	The WindShaper system [35]	17
2.29	Modulated boundary layer by fine-tuning the bottom row of fans. [34]	17
2.30	Velocity field around the wind when operating in free stream (a) and near the ground (b)	17
2.31	Standard PIV setup consisting of the following subsystems: illumination (laser), imaging device (differs per method), seeding machine (not shown), and data acquisition system. (a) Planar PIV and (b) Stereo PIV. Figures reproduced from [38]	18
2.32	PIV measurement data processing	18
2.33	Scheimpflug arrangement. Figure taken from [39]	19
3.1	The multi-fan system unit and its main dimensions.	21
3.2	The stainless steel housing of the MFS, comprising an inner and an outer case.	22
3.3	Duty Cycle VS Speed at $f_{PWM} = 25$ kHz and $U_n = 24$ V	23

3.4	Example of Serial Monitor input for constant duty cycle. The current requirement is a duty cycle value for Row 3.	23
3.5	Example of Serial Monitor input for the gust case. The duty cycle sequence reconstructs a sine wave with the mean at 50% duty cycle, and amplitude of 10% duty cycle (the max. and min. visible in the sequence are 60% and 40% duty cycle).	24
3.6	Example of sinusoidal profile as prescribed in Matlab and as received in Arduino.	24
3.7	Measurement planes	26
3.8	The planar PIV setup and instrumentation.	27
3.9	Display of the MFS mounted on the support stand with corner brackets	27
3.10	Imaging system & positioning for planar PIV	28
3.11	Planar PIV setup: the FOV after the geometric calibration, scaled with respect to the symmetry axis of the system	28
3.12	The stereo PIV setup and instrumentation	29
3.13	Camera equipment	30
3.14	Stereo PIV setup: the FOV after the geometric calibration, scaled with respect to the symmetry axis of the system	30
3.15	Illustration of the stitched streamwise plane containing details of spatial references and notations used throughout this chapter	32
3.16	Illustration of the stitched streamwise plane containing details of spatial references used in the gust analysis.	33
4.1	Line graph representation of Duty Cycle [%] VS $\overline{U}_{x, \text{far field}}$ [m/s] and fan speed [RPM]. The spatial standard deviation corresponding to each spatially averaged velocity is displayed on top of each data point.	35
4.2	Vertical streamwise plane colored by the normalized mean streamwise velocity field. The normalized streamwise velocity vectors are displayed at different locations downstream. The dotted square represents the area over which the reference velocity was averaged. Cases presented: 50% and 100% duty cycle. For $U_{x, \text{far field}, 50\%} = 4.87$ m/s, the spatial standard deviation is $\sigma = 0.10$ m/s. For $U_{x, \text{far field}, 100\%} = 6.19$ m/s, the spatial standard deviation is $\sigma = 0.12$ m/s.	35
4.3	Vertical streamwise plane colored by the RMS of the streamwise velocity fluctuations, with respect to the reference velocity, $U_{x, \text{far field}}$. The dimensional $U_{x, \text{far field}}$ is also displayed. The normalized streamwise velocity fluctuation vectors are displayed at different locations downstream. The dotted square represents the area over which the reference velocity was averaged. Cases presented: 50% and 100% duty cycle. For $U_{x, \text{far field}, 50\%} = 4.87$ m/s, the spatial standard deviation is $\sigma = 0.10$ m/s. For $U_{x, \text{far field}, 100\%} = 6.19$ m/s, the spatial standard deviation is $\sigma = 0.12$ m/s.	37
4.4	Turbulence intensity profiles at different locations downstream. Comparison between all the uniform modes. The vertical red line marks the 10% turbulence intensity	38
4.5	Cross-stream planes colored by the mean streamwise velocity normalized by the reference velocity, $\overline{U}_{x, \text{far field}}$. The in-plane velocity vectors (scaled down by a factor of 10) are overlapped. On the left: the cross-stream plane at distance D_{MFS} downstream. On the right: the cross-stream plane at distance $2.5D_{\text{MFS}}$ downstream from the MFS.	39
4.6	Cross-stream planes colored by the mean vorticity normalized by the reference velocity, $\overline{U}_{x, \text{far field}}$, and the fan diameter, d_{fan} . The in-plane velocity vectors (scaled down by a factor of 10) are overlapped. On the left: the cross-stream plane at distance D_{MFS} downstream. On the right: the cross-stream plane at distance $2.5D_{\text{MFS}}$ downstream from the MFS.	40
4.7	CP2 plane colored by turbulence intensity for the 50% and 100% duty cycle cases.	41
4.8	Duty cycle VS Turbulence intensity spatially averaged at the core of CP2.	41
4.9	Illustration of an arbitrary cross-plane and the two regions of interest: the core, assumed to be equal with the area of a fan, and the extended core.	42
4.10	Uniformity across the core (purple line) and extended core (green line), at CP1 (x marks) and CP2 (diamond marks), for the entire operating range of duty cycles.	42
4.11	Vertical profiles of the streamwise velocity at different locations in the far field. Comparison between the uniform flow case generated at 40% duty cycle and the baseline 1 case 1 variations: 37.5% (bottom row), 40% (middle row), 42.5% (top row)	44

4.12	Vertical profiles of the streamwise velocity at different locations in the far field. Comparison between the uniform flow generated at 40% duty cycle and the baseline 1 case 2 variations: 35% (bottom row), 40% (middle row), 45% (top row)	45
4.13	Vertical profiles of the streamwise velocity at different locations in the far field. Comparison between the uniform flow generated at 40% duty cycle and the baseline 1 case 3 variations: 30% (bottom row), 40% (middle row), 50% (top row)	46
4.14	Vertical profiles of the streamwise velocity at different locations in the far field. Comparison between the uniform flow case generated at 70% duty cycle and the baseline 2 case 1 variations: 67.5% (bottom row), 70% (middle row), 72.5% (top row).	47
4.15	Vertical profiles of the streamwise velocity at different locations in the far field. Comparison between the uniform flow case generated at 70% duty cycle and the baseline 2 case 2 variations: 65% (bottom row), 70% (middle row), 75% (top row)	48
4.16	Vertical profiles of the streamwise velocity at different locations in the far field. Comparison between the uniform flow case generated at 70% duty cycle and the baseline 2 case 1 variations: 60% (bottom row), 70% (middle row), 80% (top row)	49
4.17	Streamwise velocity signal spatially averaged at each time step, with a comparison to the reference velocity at 40%, 50%, and 60% duty cycle for $A_{\text{mean, MFS}} = 50\%$ and $A_{\text{mean, MFS}} = 10\%$. The comparison is made between the middle field and the far field. The mean velocity of the signal (in red text and symbolized by the red dotted line), the expected mean velocity (in black text and symbolized by the middle black dotted line), and the minimum and maximum expected values (in black text, found above and below the expected mean) are marked. First row: 0.2 Hz. Second row: 0.4 Hz. Third row: 0.8 Hz.	52
4.18	Streamwise velocity signal spatially averaged at each time step, with a comparison to the reference velocity at 40%, 60%, and 80% duty cycle for $A_{\text{mean, MFS}} = 60\%$ and $A_{\text{mean, MFS}} = 20\%$. The comparison is made between the middle field and the far field. The mean velocity of the signal (in red text and symbolized by the red dotted line), the expected mean velocity (in black text and symbolized by the middle black dotted line), and the minimum and maximum expected values (in black text, found above and below the expected mean) are marked. First row: 0.2 Hz. Second row: 0.4 Hz. Third row: 0.8 Hz.	53
4.19	Streamwise velocity signal spatially averaged at each time step, with a comparison to the reference velocity at 20%, 50%, and 80% duty cycle for $A_{\text{mean, MFS}} = 50\%$ and $A_{\text{mean, MFS}} = 30\%$. The comparison is made between the middle field and the far field. The mean velocity of the signal (in red text and symbolized by the red dotted line), the expected mean velocity (in black text and symbolized by the middle black dotted line), and the minimum and maximum expected values (in black text, found above and below the expected mean) are marked. First row: 0.2 Hz. Second row: 0.4 Hz. Third row: 0.8 Hz.	54
4.20	PSD for the gust case: $A_{\text{mean, MFS}} = 50\%$ and $A_{\text{mean, MFS}} = 10\%$, and uniform case: 50%. The left figure shows the energy distribution of the middle field signal at 0.2 Hz, 0.4 Hz, 0.8 Hz, and the uniform case. The right figure shows the energy distribution of the far field signal at 0.2 Hz, 0.4 Hz and the uniform case.	55
4.21	PSD for the gust case: $A_{\text{mean, MFS}} = 60\%$ and $A_{\text{mean, MFS}} = 20\%$, and uniform case: 60%. The left figure shows the energy distribution of the middle field signal at 0.2 Hz, 0.4 Hz, 0.8 Hz, and the uniform case. The right figure shows the energy distribution of the far field signal at 0.2 Hz, 0.4 Hz and the uniform case.	56
4.22	PSD for the gust case: $A_{\text{mean, MFS}} = 50\%$ and $A_{\text{mean, MFS}} = 30\%$, and uniform case: 50%. The left figure shows the energy distribution of the middle field signal at 0.2 Hz, 0.4 Hz, 0.8 Hz, and the uniform case. The right-hand side figure shows the energy distribution of the far field signal at 0.2 Hz and the uniform case.	56
4.23	The vertical profiles of mean the streamwise velocity at the center of CS2 (blue) and at the corresponding location on the vertical streamwise plane (red)	58
4.24	The absolute error [m/s] between the mean streamwise velocity vertical profiles measured with planar and stereo PIV at $2.5D_{\text{MFS}}$, at the center of the system	58
A.1	Circuit diagram of the 9 fans and Arduino	64
C.1	Duty Cycle [%] vs Flow Speed [m/s] (measurements with Pitot-static probe)	74

D.1	Vertical streamwise plane colored by the mean streamwise velocity normalized by $\overline{U}_{x, \text{far field}, 100\%}$. The normalized streamwise velocity vectors are displayed at different locations downstream. Duty cycles: 10%-40%	75
D.2	Vertical streamwise plane colored by the mean streamwise velocity normalized by $\overline{U}_{x, \text{far field}, 100\%}$. The normalized streamwise velocity vectors are displayed at different locations downstream. Duty cycles: 50%-100%.	76
D.3	Cross-stream planes colored by the mean vorticity normalized by the reference velocity, $\overline{U}_{x, \text{far field}}$, and the fan diameter, d_{fan} . The in-plane velocity vectors (scaled down by a factor of 10) are overlapped. On the left: the cross-stream plane at distance D_{MFS} downstream. On the right: the cross-stream plane at distance $2.5D_{\text{MFS}}$ downstream from the MFS. Duty cycles: 10%-30% . . .	77
D.4	Cross-stream planes colored by the mean vorticity normalized by the reference velocity, $\overline{U}_{x, \text{far field}}$, and the fan diameter, d_{fan} . The in-plane velocity vectors (scaled down by a factor of 10) are overlapped. On the left: the cross-stream plane at distance D_{MFS} downstream. On the right: the cross-stream plane at distance $2.5D_{\text{MFS}}$ downstream from the MFS. Duty cycles: 40%-60% . . .	78
D.5	Cross-stream planes colored by the mean vorticity normalized by the reference velocity, $\overline{U}_{x, \text{far field}}$, and the fan diameter, d_{fan} . The in-plane velocity vectors (scaled down by a factor of 10) are overlapped. On the left: the cross-stream plane at distance D_{MFS} downstream. On the right: the cross-stream plane at distance $2.5D_{\text{MFS}}$ downstream from the MFS. Duty cycles: 70%-90% . . .	79

List of Tables

2.1	Typical surface roughness lengths. Source: [19]	4
3.1	The multi-fan system dimensions	21
3.2	Electrical & mechanical operating features of one fan at 100 % duty cycle. Information taken from the product data sheet [42]	22
3.3	Test cases of the MFS boundary layer mode: the two baseline cases and the test ranges corresponding to the duty cycle increments.	25
3.4	Test cases of the MFS gust mode. The operating conditions of the fans are given by three frequencies: 0.2Hz, 0.4Hz and 0.8Hz, and three amplitudes: 10 %, 20% and 30%. The mean and range of the amplitudes are also provided.	25
3.5	Planar PIV setup: camera parameters	28
3.6	Stereo PIV setup: camera parameters	30
3.7	Uniform flow test matrix showing the duty cycle values, the time step between pulses for the corresponding PIV method, the number of samples acquired and the measurement planes	31
3.8	Boundary layer test matrix showing the baseline cases and their corresponding steps, the time step between pulses for the corresponding PIV method, the number of samples acquired and the measurement planes	31
3.9	Gust test matrix showing the operating frequency, mean operating amplitude, operating amplitude, time steps, and measurement planes	31
4.1	Baseline 1, case 1: duty cycle variations (first column), expected streamwise velocity (dimensional, second column), expected streamwise velocity (normalized, third column), expected relative variation from the baseline 1 reference velocity (fourth column)	45
4.2	Baseline 1, case 2: duty cycle variations (first column), expected streamwise velocity (dimensional, second column), expected streamwise velocity (normalized, third column), expected relative variation from the baseline 1 reference velocity (fourth column)	45
4.3	Baseline 1, case 3: duty cycle variations (first column), expected streamwise velocity (dimensional, second column), expected streamwise velocity (normalized, third column), expected relative variation from the baseline 1 reference velocity (fourth column)	46
4.4	Baseline 2, case 1: duty cycle variations (first column), expected streamwise velocity (dimensional, second column), expected streamwise velocity (normalized, third column), expected relative variation from the baseline 1 reference velocity (fourth column)	47
4.5	Baseline 2, case 2: duty cycle variations (first column), expected streamwise velocity (dimensional, second column), expected streamwise velocity (normalized, third column), expected relative variation from the baseline 1 reference velocity (fourth column)	48
4.6	Baseline 2, case 3: duty cycle variations (first column), expected streamwise velocity (dimensional, second column), expected streamwise velocity (normalized, third column), expected relative variation from the baseline 1 reference velocity (fourth column)	49
A.1	Current and power consumption of the prototype	65

Nomenclature

Abbreviations

Abbreviation	Definition
ABL	Atmospheric Boundary Layer
BLWT	Boundary Layer Wind Tunnel
EOG	Extreme Operating Gust
HWA	Hot Wire Anemometry
MAV	Micro Air Vehicle
MFS	Multi-Fan System
NAV	Nano Air Vehicle
PIV	Particle Image Velocimetry
PSD	Power Spectral Density
PWA	Pulse-Width Modulation
RPM	Rotations Per Minute
SL	Surface Layer
UAV	Unmanned Aerial Vehicle

Symbols

Symbol	Definition	Unit
d_{fan}	The diameter of the fan	[mm]
d_{hub}	The diameter of the hub	[mm]
D_{MFS}	The length of the multi-fan system	[mm]
f_{PWM}	The pulsing frequency of the PWM	[kHz]
f_{MFS}	The operational frequency of all the fans	[Hz]
N	Number of fans per row or column	
M	Mach number	
\bar{U}_x	Mean Streamwise Velocity	[m/s]
$\sqrt{\overline{U_x'^2}}$	RMS of the Streamwise Velocity Fluctuations (standard deviation)	[m/s]
U_x	Spatially Averaged Streamwise Velocity at an arbitrary location	[m/s]
$U_{x, far\ field}$	reference velocity; the mean streamwise velocity spatially averaged at the far field location	[m/s]
U_n	Nominal voltage	[V]
σ	Spatial Standard Deviation	[m/s]
$\bar{\omega}$	Mean vorticity in the x direction	[1/s]

1

Introduction

Wind is one of the few perpetual natural resources on Earth, continuously sparking the interest of humankind throughout history up to the present day. Its impact have always had both favorable and disastrous outcomes in our daily lives. Harnessing its potential for positive use while mitigating its destructive forces requires a deep understanding, achieved through meticulous observation, theoretical exploration, and experimental study.

The earliest recordings of harnessing wind date back to antiquity, when Egyptians built the first wind-powered sails to navigate the waters, around 3000 BC, and when windmills were created for grain grinding in the Middle East, in the first centuries AD [1]. Their development continued through the Middle Ages and spread to Europe as well, due to the expansion of early industrial processes and maritime exploration. Then the Renaissance bloomed in Europe, when early observations on flow over rigid bodies and studies on atmospheric instrumentation were conducted by Leonardo da Vinci and Galileo Galilei, setting the starting points of aerodynamics and meteorology. In the 17th and 18th centuries, scientists and astronomers used their observations to investigate the origins of wind, the global atmospheric motions, and climate, through works like Edmund Halley's, who was the first to point out that wind is generated because of 'the action of the sun's beams upon the air and water, as he passes every day over the oceans' [2]. Moreover, in 1749, the first experiments with kites were performed, as means to access higher altitudes for atmospheric temperature measurements [3]. These studies shaped the fundamentals of meteorology, which aided in agricultural and military advancements at that time.

Later on, the rapidly growing demands of humanity set a high-paced development of new technologies and theoretical knowledge. At the end of the 19th century, due to the increased used of electricity, the first attempts to create electricity from wind were documented, with Charles F. Brush and his 'Brushmill' as one of the pioneers. Concurrently, Douglas Archibald used kites to study the profile of the mean wind speed in the atmosphere, expressing it through the power law [4], contributing to the early efforts of addressing the similarities between the boundary layer of a fluid flowing over a rigid body, and the air masses flowing over the Earth's surface. In the 20th century, the research and development of combat and commercial aircraft led to crucial insights regarding the aerodynamic performance, through lift and drag analysis, and the aeroelastic behavior, through flutter [5]. In the civil engineering sector, this dynamic instability phenomenon was reported for the first time when the Tacoma Bridge collapsed in 1940 [6]. The study of flutter and airflow-structure interactions evolved in the 20th century, subjecting not only aircraft and civil structures, but also multi-megawatt wind turbines, whose emergence was triggered by the 1970's oil crisis. Today, global efforts to mitigate climate change and achieve carbon neutrality are driving advancements in wind turbine technology, airborne wind energy systems, and unmanned aerial vehicles, with the research focused on enhancing the structural, aerodynamic, and operational performance under different unsteady inflow conditions, such as wind gusts and shear layers.

As history has shown, understanding atmospheric motion has always been crucial in meeting the evolving needs of each era. The majority of the activities discussed above occur within the atmospheric boundary layer (ABL), the lowest layer of the troposphere, a region that has been extensively studied and well-characterized

over the years. The ABL is formed due to the interaction between the motion of air and the surface of the Earth, extending for 1-2 km above the ground [7]. Highly unsteady, wind within the ABL is influenced by surface conditions, diurnal and seasonal radiative heating over the ground and large-scale pressure fields dominating the layer above [8]. Understanding the impact of the random and complex motions within the ABL on different structures is not trivial, but it is significantly more feasible than two decades ago. This is because of the advanced numerical models, powerful computational resources and more precise measurement techniques used nowadays. Experimental research remains a crucial approach in providing direct insights into wind-structure interactions and enhancing our ability to predict and mitigate their effects.

Traditionally, wind tunnels have been a reliable tool for simulating real-world wind conditions as means of measuring the aerodynamic forces acting on the given structure. As different types of wind tunnels are employed for specific applications, low-speed wind tunnels are naturally suitable for reproducing idealized uniform flows, gusts or shear layers. In standalone configuration, they are able to generate uniform flow of high uniformity (0.3, 0.4 %) and low turbulence intensity (> 0.2 %) [9]. Depending on the wind flow conditions, additional passive and/or active devices are employed. Furthermore, a measurement technique is chosen based on the objectives of the experiment, and based on the accessibility to the necessary equipment. Particle Image Velocimetry (PIV) is, at the moment, the most popular measurement technique that offers a quantitative understanding of the instantaneous flow fields.

Recently, a new wind generation system has drawn attention within the engineering communities: the multi-fan wind generator. Consisting of multiple fans arranged in a desired rectangular layout, the system allows for the individual control of each fan, usually by varying the voltage via a computer interface. This specification allows for the generation of a wide range of unsteady wind conditions experienced within the ABL, and also idealized uniform conditions with low turbulence intensity and high uniformity. Currently, a high-performance, thoroughly characterized, but costly system is commercially available and can be employed to produce complex wind patterns: WindShaper [10]. The turbulence intensity of the generated uniform flow is of 5%, and the uniformity, although not quantified, is observed to be high through mean velocity color maps. In unsteady conditions, the turbulence intensity reflects the real values of ABL conditions [11]. However, considering a multi-fan system could be a low-cost and reliable alternative to the wind tunnel, many research groups opted for developing in-house multi-fan systems placed either upwind of the test section, in a tunnel [12], or set as an open facility to enable real-scale experiments [13]. Each available facility has been characterized from an aerodynamic point of view, but at the level of detail and completeness based on the application and the measurement equipment at hand. Most of them used pointwise measurements due to the sole interest on wind speed time-history reproduction for different vertical profiles, thus the turbulence intensity and scales are reported, along with the validation of reproduction capabilities [14], [15], [16]. The spatial uniformity over the cross-section of the field was additionally assessed in the case of drones testing, with full-field measurement techniques, but in the same manner as for the WindShaper. Regarding shear wind profiles, they could be reproduced within multi-fan wind tunnels or with passive surface roughness elements, whereas the in-house open facilities lack such reports. Finally, gusty conditions could also be reproduced, from sudden step increase (extreme gusts) [17], to streamwise sinusoidal gusts [12], although limitations due to fans inertia were reported. These investigations provide both common and specific insights into the flow fields. Therefore, conducting a thorough aerodynamic characterization of a newly developed multi-fan system, regardless of its application, is a top priority.

The motivation behind this master thesis project is to manufacture a unit of 3 x 3 fans and test its capability to generate uniform flow, linear wind shear profiles, and streamwise sinusoidal gusts. The system consists of off-the-shelf computer fans that are controlled through open-source codes. The aerodynamic characterization of the flow field is conducted with PIV.

The thesis is structured into four chapters, as follows. In chapter 2, the literature is reviewed to gain insights into existing multi-fan wind generation systems and their manufacturing, control, and characterization. After that, the research questions are formulated, along with the objectives set to address them. Next, chapter 3 highlights the methodology used to achieve these objectives. It guides the reader through the stages of setting up the multi-fan system (subsection 3.1.1), selecting the test cases (section 3.2), and preparing the environment of the experiment (section 3.3). chapter 4 presents the results and discusses the findings for each flow case: uniform flow (section 4.1), linear wind shear (section 4.2), and gust (section 4.3). Finally, chapter 5 provides an overview of the work completed in this project, highlights the key conclusions, and offers recommendations on approaching and enhancing the workflow for future investigations.

2

Literature Review

This chapter begins by defining the atmospheric boundary layer (ABL) and the unsteady flow conditions that are most frequently reproduced in aerodynamic experiments. Then, it offers a comprehensive review of the existing literature on wind generators used in engineering experiments, with a specific emphasis on multi-fan arrays. Next, the chapter introduces the Particle Image Velocimetry (PIV) technique, which has been selected for flow measurement in this study. The chapter concludes by highlighting gaps in the current literature, formulating the research questions, and outlining the objectives of the research.

2.1. An overview of the unsteady wind flow within the ABL

This section provides a general introduction to the characteristics of the flow experienced in the ABL. It describes the wind shear and gust within the ABL and the engineering models used to simulate them. It also mentions the typical values of turbulence intensity that characterize the unsteady nature of the wind within the ABL.

2.1.1. Wind shear

The troposphere is the lowest part of Earth's atmosphere, extending around 11 km altitude and capped by the tropopause, above which commercial airplanes operate. As we get closer to the Earth's surface, the atmospheric motions become more influenced by the surface conditions. Depending on the proximity to the ground, two different layers are defined within the troposphere: the free atmosphere, and the atmospheric boundary layer (Figure 2.1a). Most of the weather occurs in the free atmosphere, where large-scale circulation patterns rule, while the ABL is the region that more directly affects our daily activities and engineering applications.

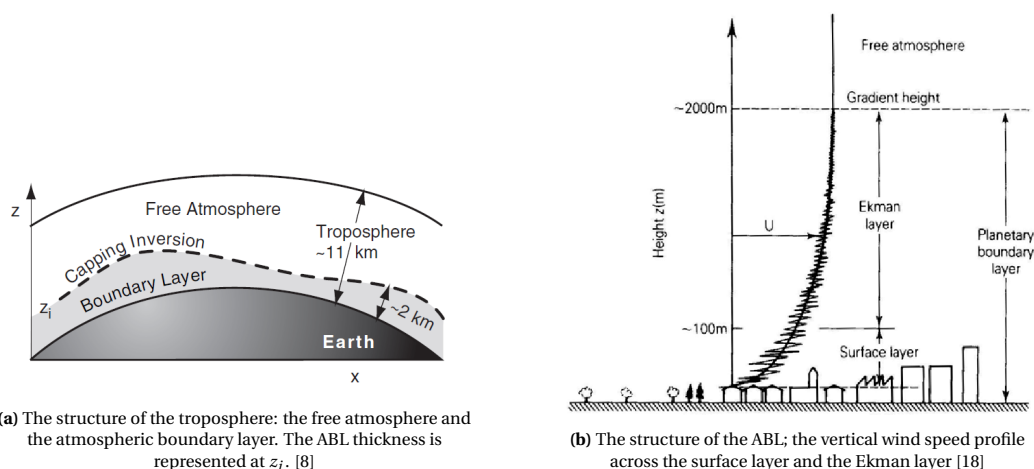


Figure 2.1: The structure of the troposphere (a) and the ABL (b)

The atmospheric boundary layer, or the planetary boundary layer, is the lowest region of the troposphere where surface roughness is the primary influence on the wind behavior, along with the diurnal and seasonal radiative heating. Its thickness spans 1-2 km above the ground [7], and the flow within is characterized by turbulence mixing and wind shears, resulting in strong variations of the wind magnitude. This strong non-uniformity is more characteristic to the lower region of the ABL, known as the surface layer (SL). The outer region of the ABL is the Ekman layer, where the wind shows both variations of magnitude (however, less), and direction, due to Earth's rotation. The structure of the ABL is depicted in Figure 2.1. The SL is the region of greater interest, since the wind resource there influences the performance and loading of wind turbines, the operation of UAVs, the urban aerodynamics studies, and how we experience the local environment, in general. The cause of this influence comes from the variation of wind with altitude, and from the short time-scale flow structures that load the structures unevenly in time and space. At amplitudes above 100 m, airborne wind energy systems, like kites, are employed to harness the energy of the wind. Above the ABL, the free atmosphere layer is characterized by balance between pressure gradient and Coriolis force, the wind here being horizontally homogeneous and friction-free [8].

To describe how the mean wind varies with height above the ground in the ABL, two models are usually employed: the logarithmic wind profile, or the power law. The log law offers a more theoretical approach to explore the relation between the horizontal mean wind speed and height, because it expresses the mean wind variation with height based on the local surface roughness, friction velocity, and the stability of the ABL. Equation 2.1 represents the logarithmic wind profile for neutral atmospheric conditions.

$$u(z) = \frac{u_*}{k} \ln\left(\frac{z}{z_0}\right) \quad (2.1)$$

where u_* [m/s] is called the friction velocity; k is the von Karman constant; z [m] is the height above the ground; z_0 [m] is the roughness length.

The roughness length is used to classify different types of landscape that give the best fit of the measurements of the ABL. The typical surface roughness lengths are shown in Table 2.1:

Type of Terrain	Roughness length z_0 [m]
Cities, forests	0.7
Suburbs, wooded countryside	0.3
Villages, countryside with trees and hedges	0.1
Open farmland, few trees and buildings	0.03
Flat grassy plains	0.01
Flat desert, rough sea	0.001

Table 2.1: Typical surface roughness lengths. Source: [19]

The power law is an engineering model used to describe the variation of wind speed with height using a reference wind speed at a reference height, and a wind shear exponent α . The relation is translated as:

$$u(z) = u_0 \left(\frac{z}{z_0}\right)^\alpha \quad (2.2)$$

The exponent α also varies with the type of terrain, with typical values of 0.2 and 0.14 for open wind conditions onshore and offshore, respectively [19].

2.1.2. Gust

Due to the unsteady nature of the flow within the atmospheric boundary layer (ABL), sudden time variations of wind speed, known as gusts, frequently occur. These random perturbations impose abrupt additional structural loads on machines, devices, and structures that continuously interact with the wind, increasing the complexity of wind-structure coupling and reducing their operational lifespan.

In the certification phase of a wing or rotor design, the models are simulated numerically and in wind tunnels under extreme wind conditions. For instance, one of the requirements of validating the structural integrity of a wind turbine is to evaluate its response under extreme operating gust, as seen in Figure 2.2, as requested by

the international standard [20]. Extensive experiments are carried out for UAVs as well, since their stability can be heavily affected by wind gusts.

In a more broad sense, engineers have used simple periodic free-stream models when studying the response and wake of different structures in gusty winds, like sinusoidal oscillations. A sinusoidal fluctuation flow was first analytically employed by R. Isaacs [21], who superimposed a velocity constant with the sinusoidal streamwise gust. This practical approach, expressed in Equation 2.3, was later used in several studies, such as the numerical investigation of loads on helicopter blades [22] or the experimental study of unsteady lift on an airfoil [12] operating in gusty conditions, as well as in the study of wind generators to produce unsteady flows [23].

$$U(t) = \bar{U}(1 + \sigma \sin(2\pi f t)) \quad (2.3)$$

where \bar{U} [m/s] is the mean free-stream speed, f [Hz] is the flow oscillation frequency, and σ is the normalized velocity oscillation amplitude relative to \bar{U} [23].

The degree of unsteadiness can be quantified by computing the reduced frequency [5] (Equation 2.4), a dimensionless parameter that relates the oscillatory motion of a body to the convective flow. A higher reduced frequency indicates a greater influence of unsteady effects, making it a crucial parameter in analyzing unsteady aerodynamic effects, such as gust responses, or flutter.

$$k = \frac{\pi f c}{U_x} \quad (2.4)$$

where c [m] is the chord length (in the case of blade-level dynamics; for rotor-level, or dynamic inflow, the rotor radius R is used), and U_x is the free-stream reference velocity.

When $k = 0$, the flow is steady; when $0 \leq k \leq 0.05$, the flow is considered quasi-steady; if $0.05 \leq k \leq 0.2$, the flow is considered unsteady, while if $k > 0.2$, the flow is highly unsteady.

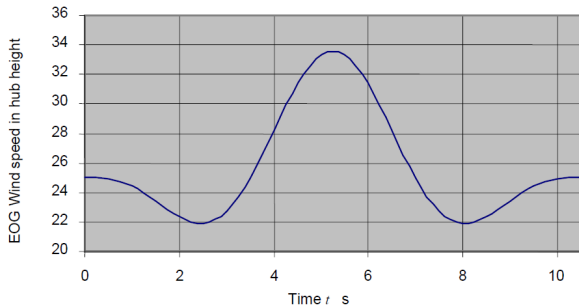


Figure 2.2: Example of extreme operating gust [20]

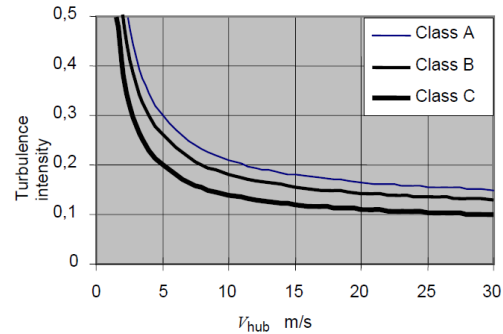


Figure 2.3: Turbulence intensity for the normal turbulence model [20]

2.1.3. Turbulence Intensity

As previously mentioned, the flow within the ABL is turbulent. The experimental and numerical simulation of the wind conditions in the study of the wind-structure interference requires that real values of turbulence intensity should be obtained. For instance, the standard for wind turbine design certification specifies the turbulence intensity values for each wind turbine class as a function of the velocity experienced at the hub (Figure 2.3).

The wind shear and gust conditions introduced in this section can be experimentally reproduced in controlled facilities. The next section presents different solutions of achieving this.

2.2. Wind tunnels: passive and active methods for wind shear and gust generation

Low-speed wind tunnels are essential tools in aerodynamic research, providing valuable insights into low-speed fluid dynamics and performance characteristics. By replicating real-world conditions of wind speeds up to $M = 0.3$ in a controlled setting, they allow researchers to assess lift, drag, and flow separation, which are critical factors in aircraft, vehicle or wind turbine research and development, as well as to study the impact of wind on buildings and bridges. The free stream at the test section is reported to be characterized by values of turbulence intensity below 0.2, and spatial uniformity of 0.2-0.3 [9]. Over time, advancements in flow control technology have enabled a wide variety of methods to generate specific flow conditions, such as atmospheric boundary layer profiles and gusts. These devices can trigger the flow in passive or active ways, or by a combination of both.

2.2.1. Experimental methods for generating unsteady wind shear inflow

Some of the most common passive methods employed to generate steady or unsteady ABL profiles in the test section of a general-purpose wind tunnel are presented as follows. Roughness elements, such as arrays of blocks and ridges placed on the wind tunnel floor, determine the resulting roughness length and turbulence intensity. Placed at the tunnel inlet, spires, barrier walls (Figure 2.4b) and circular or rectangular rods (Figure 2.4a) are structures used to induce local vertical velocity gradients that develop downstream into a profile with a specific depth modeled after the height of the grid they form. These elements are often combined to trigger turbulence production, leading to turbulence intensities and scales typical to ABL conditions. An example is the ABL outlet attachment with spires and roughness elements (Figure 2.4c) developed by the PhD candidate Brian D'Souza from the Aerodynamics Department of the Faculty of Aerospace Engineering, TU Delft.

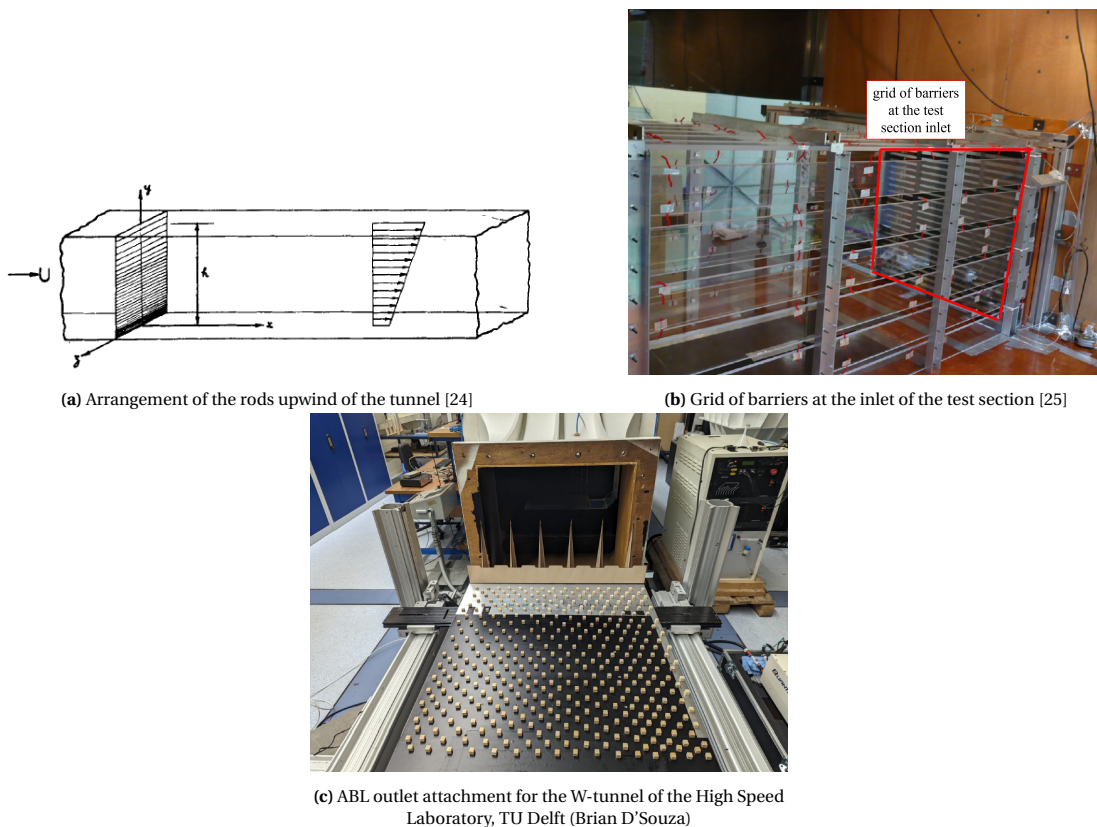


Figure 2.4: Different passive methods of generating unsteady ABL profiles

The same elements are found in boundary layer wind tunnels (BLWT), developed for wind engineering purposes. They usually consist of long test chambers along the span of which large-scale boundary layers can

develop. The main requirement of these tunnels is to ensure zero pressure gradient. Two examples of BLWTs are shown in Figure 2.5.

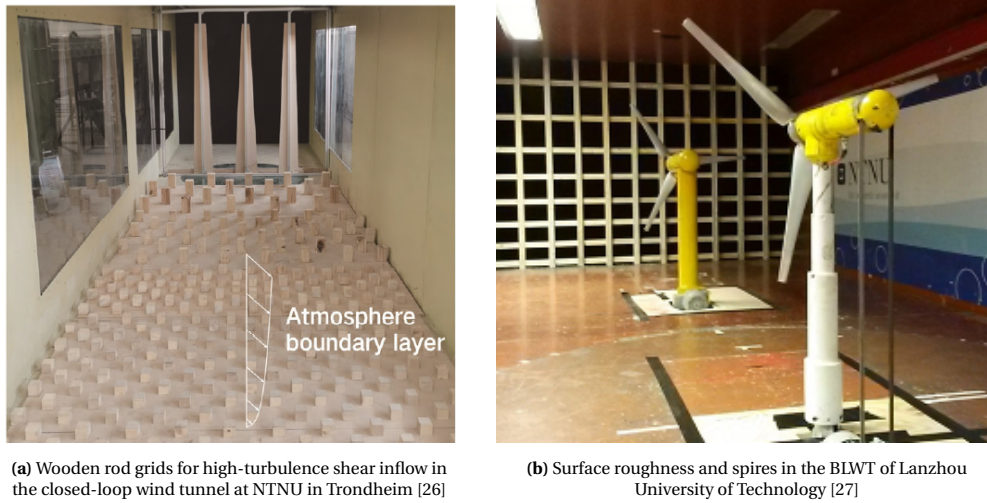


Figure 2.5: BLWT configurations: surface elements and spires (a) and wooden rods grid (b)

An active method to generate unsteady ABL profiles could be the multi-jet wind tunnel [28], intended to be used for aerodynamic studies of aircraft, vehicles and other structures. The flow is generated by an array of 8 x 8 jets individually controlled through the air supply system. The flow characterization was conducted with a vertical array of hot wire probes at different distances downstream, to reproduce the mean vertical velocity profile.

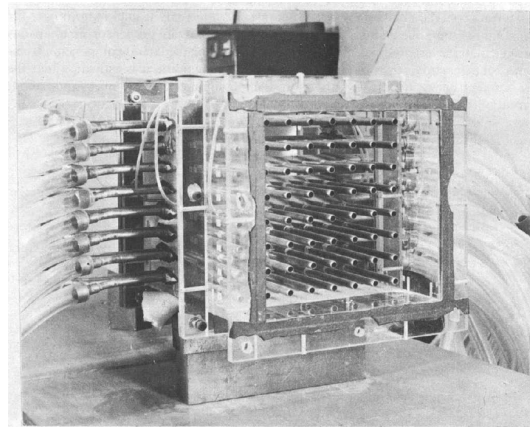
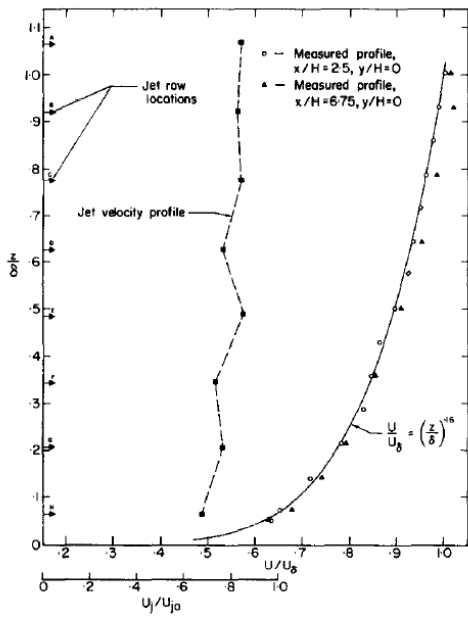
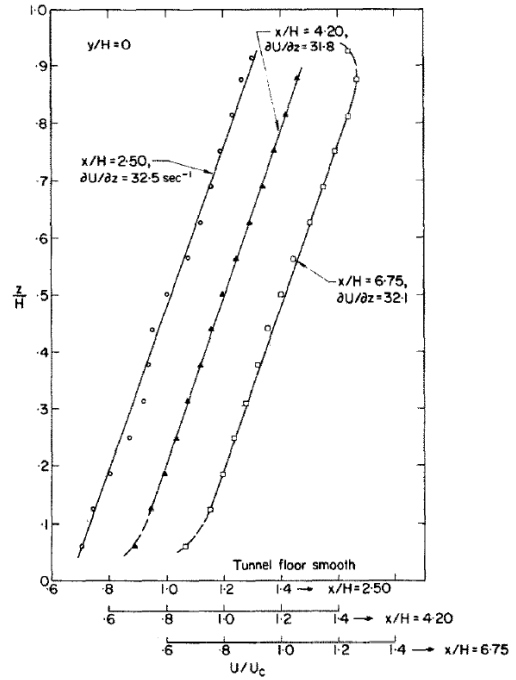


Figure 2.6: Wind tunnel jet grid section [28]

Initially, the goal was to obtain ABL profiles by setting the jets to obey a predefined mean velocity power law profile. However, the jets failed to reproduce the desired profile, and the author attributes this to the interaction of the jets and wall effects. In consequence, the solution was to adjust the jets until the prescribed velocity profile was obtained. By multiple combinations of jet adjustments, and several repetitions of the same combination it was established that the jet profiles uniquely correspond to a particular ABL profile. One example is the mean velocity profile shown in Figure 2.7a. The profile on the left corresponds to the velocity of the jets after adjustments, while the one on the right reflects the measured profile, which fits neatly the prescribed one. Moreover, linear shear flows were tested by following the same procedure, and the resulting profiles are shown in (Figure 2.7b). It was found that the measured profiles maintain the same prescribed mean velocity, and the gradients are 0.37 - 0.44 times the prescribed gradients. Finally, a key observation was that the desired ABL flow characteristics could be obtain within 11-12 boundary layer heights downstream of the jets, half the length needed in typical BLWTs.



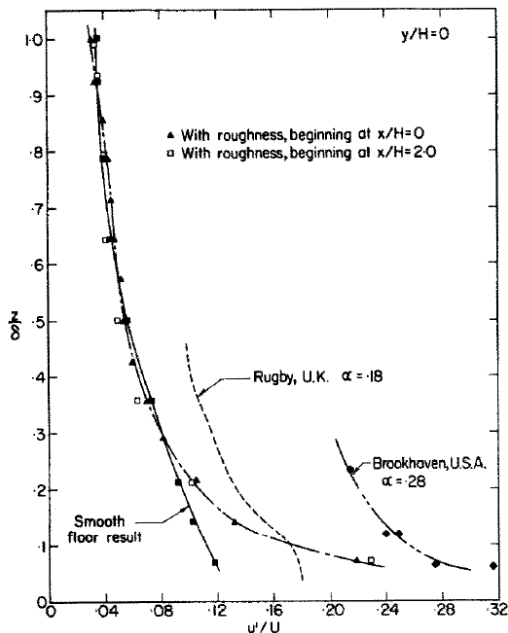
(a) Mean velocity profile. The jets are set to obtain $\alpha = 0.16$, at $x/H = 2.5$; smooth tunnel floor conditions



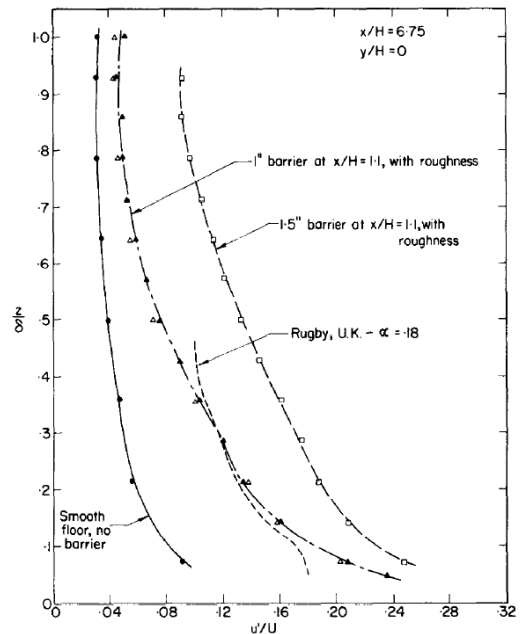
(b) Development of mean velocity profile in linear shear flow, at $x/H = 2.5, 4.2, 6.75$; smooth tunnel floor conditions

Figure 2.7: Mean velocity profiles that follow a prescribed power law (a) and a prescribed linear function (b) [28]

The turbulence intensity, below 10% in smooth-floor conditions, was regarded as too weak to mimic ABL conditions. Therefore, to increase the turbulence production, LEGO base plates (Figure 2.8a) and flat-barrier plates (Figure 2.8b) were added on the tunnel floor. The latter shows a better agreement between the resulting turbulence intensity and the real ABL conditions, with values between 10% and 20% across the height.



(a) Turbulence intensity profiles at $x/H = 6.75$ for $\alpha = 0.25$ velocity profiles; LEGO surface effect. Comparison with smooth floor, no surface roughness conditions.

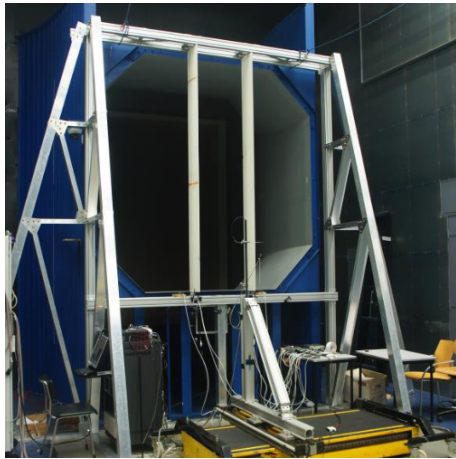


(b) Turbulence intensity profiles at $x/H = 6.75$ for $\alpha = 0.16$ velocity profiles; barrier-plate effect. Comparison with smooth floor, no barrier conditions.

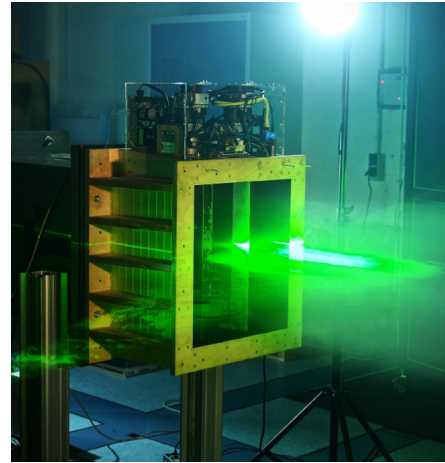
Figure 2.8: Turbulence intensity profiles after adding (a) LEGO surface and (b) barrier-plate [28]

2.2.2. Experimental generation of gusts

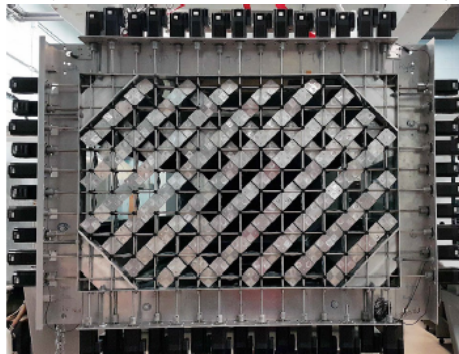
Different experimental techniques of generating gusts have been investigated. Most of them consist of single or multiple oscillating vanes. The gust generators developed within the Faculty of Aerospace Engineering at TU Delft present two oscillating vanes that differ in scale: one serves for a large aerodynamic testing facility, the Open Jet Facility (Figure 2.9a), while the other serves as attachment to the test section of the W-tunnel (Figure 2.9b). They can operate for reduced frequencies of the unsteady regime, up to $k = 0.2$, and produce both sinusoidal and 1-cos gust types. Figure 2.9c shows another gust-generating method: an active grid consisting of rotating wings, mounted at the test section of the wind tunnel at the University of Toronto Institute for Aerospace Studies. It enables more actuation modes than the simple oscillating vanes, such as one-direction rotation of the wings, continuous two-directions rotation (open-close), instantaneous motion and user-defined motion. They can all occur in or out of phase with each other.



(a) Gust generator with 2 oscillating vanes for the Open Jet Facility of the High Speed Laboratory, TU Delft [29]



(b) Gust generator with 2 oscillating vanes for the W-tunnel of the High Speed Laboratory, TU Delft [30]



(c) Active grid [23]

Figure 2.9: Examples of different gust generating devices

Apart from the wind tunnel technologies and the active and passive devices that aid in modeling the flow, another wind generation facility has been developed and used in the simulation of unsteady ABL conditions - the multi-fan wind generation system. The next section provides an overview of the variety of such systems and the applications they have been involved in.

2.3. Multi-fan array wind generators

A multi-fan wind generator is a system composed of fans stacked in a customizable arrangement and that can be individually controlled to generate specific wind conditions. Its modular design allows for flexible configurations, making it easy to assemble and disassemble, transport, and scale depending on the model tested. Each fan can be controlled by varying the rotational speed, allowing for the reproduction of wind conditions with spatial and temporal resolutions as per the capabilities of the fan models. Considering this, it is of interest to assess the capacity and limitations of the multi-fan systems and the flow they generate.

In the rest of the section, several existing multi-fan array wind generators attached to a tunnel or in open environment are presented. We are interested in learning about their configurations, the mode of operation, the aerodynamic properties of the flow they generate and the flow measurement method, and the purpose for which they were developed.

The idea of employing multiple fans to drive the flow in aerodynamic experiments was first applied by A. Nishi [14], who aimed to control the turbulence intensity of the ABL profiles resulted by the individual operation of the fans. The motivation is somewhat similar to the control of turbulence by employing jets [28]. Two setups were placed upstream of a tunnel, a 2D one consisting of 11 fans stacked vertically, driven by AC servo-motors, and a 3D setup made of 6 x 11 fans, driven by AC induction motors. A honeycomb and vortex-generating bars were added downstream of the convergent part to eliminate the effects of the secondary flow and the boundary layer induced by the channels connected to the fans. Vibrating blades were placed further downstream to aid in the turbulence production. The fans and the blades were all controlled from a computer. The schematics of the wind tunnel is presented in Figure 2.10.

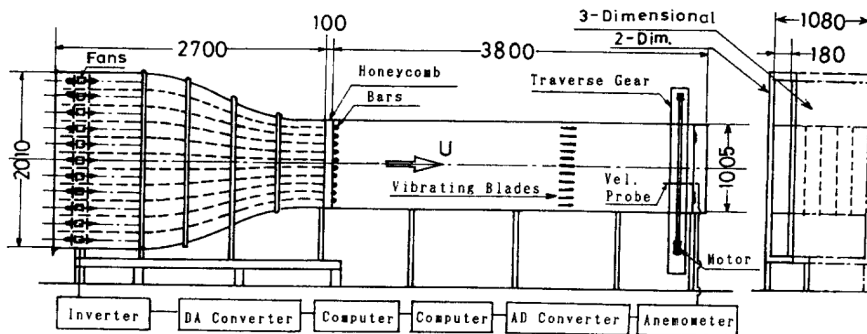


Figure 2.10: The multi-fan wind tunnel setup [14]

The mean wind profiles measured upstream of the blades by a hot wire probe is depicted in Figure 2.11. The first two profiles present equally distant velocity deficits at locations that might correspond to the hub of the fans. As the flow evolves downstream, the profiles seem to develop into smooth shear profiles.

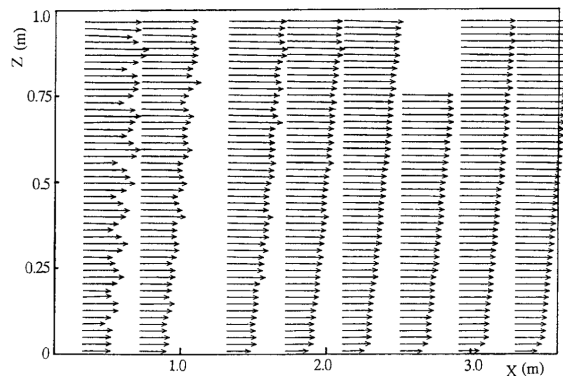


Figure 2.11: Mean wind profiles for a shear flow developed in the tunnel ([14])

As mentioned, the purpose of the experiment was to test the fidelity of the fans to generate a predefined wind time history. For this, two open-loop feedback methods were created: the calibration of the measured power spectrum, and the calibration of the time lag induced by the low inertia of the fans. In both methods, the velocity history was converted into voltage data and fed to the fans. Then, the velocity was measured with a probe, and one of the two methods was applied to correct the resulted data and send it back as new input time series. The resulting normalized profiles of mean streamwise component velocity, $U(z)$, turbulence intensity, $I_u(z)$, and turbulence scale, $L_u(z)$, corresponding to each flow control method can be visualized in Figure 2.12. The flow was modeled after the power law, with $\alpha = 0.3$, and reached after a shorter distance

from the fans than in an ABL wind tunnel - the same conclusion given for the multi-jet wind generator [28]. Both methods were reported to show good agreements between the measured velocity and corresponding turbulence velocity profiles and the target ones.

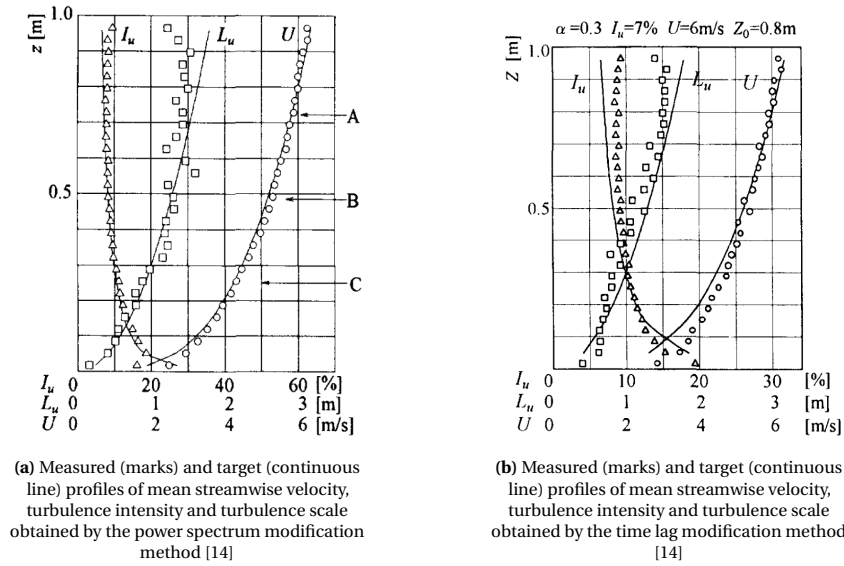


Figure 2.12: Measured and target profiles of mean streamwise velocity, U , turbulence intensity, I_u , and turbulence scale, L_u , obtained by (a) power spectrum modification method and (b) time lag modification method [14]

Optimizing the flow control techniques of the multi-fan system to modulate turbulent ABL characteristics has later become the main objective for other studies. The motivation behind this research ranges from monitoring the air quality to analyzing isolated buildings in rough wind conditions. The first one is invoked by [15], whose work focuses on a closed-loop feedback method used to control the recorded outdoor signal fed to the fans. The second one is attributed to [16], who simulated the effectiveness of the fans in changing both the speed and the direction of the wind, by mounting them on swivel plates. Both facilities can be seen in Figure 2.13 and Figure 2.14, respectively. Moreover, they both share a novel means of controlling the rotational speed of the fans, compared to Nishi: pulse-width modulation (PWM).



Figure 2.13: The multi-fan full-scale facility at the Insurance Institute for Business & Home Safety [15]

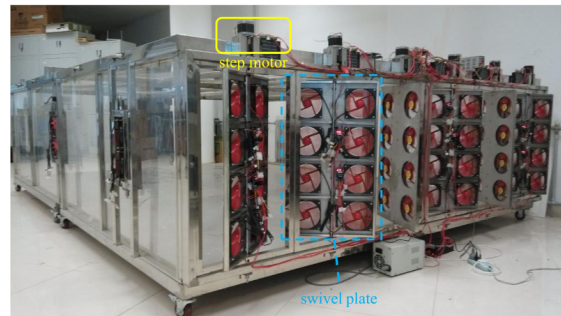


Figure 2.14: The multi-fan system with swivel plates at the Tianjin Key Laboratory of Process Measurement and Control [16]

Apart from developing more simple and accurate ways of reconstructing the complex wind field for large-scale applications, like building aerodynamics or air quality assessment, other studies focused on the generation of simplified conditions and their effect on airborne models, such as aircraft wings and UAVs. For instance, [12] investigated the lift unsteadiness over a stationary airfoil in a sinusoidal streamwise gust attached to the airfoil, using the multi-fan wind tunnel in Figure 2.15, and compared the results with theoretical models. The control of the fans was facilitated by AC servo-motors.

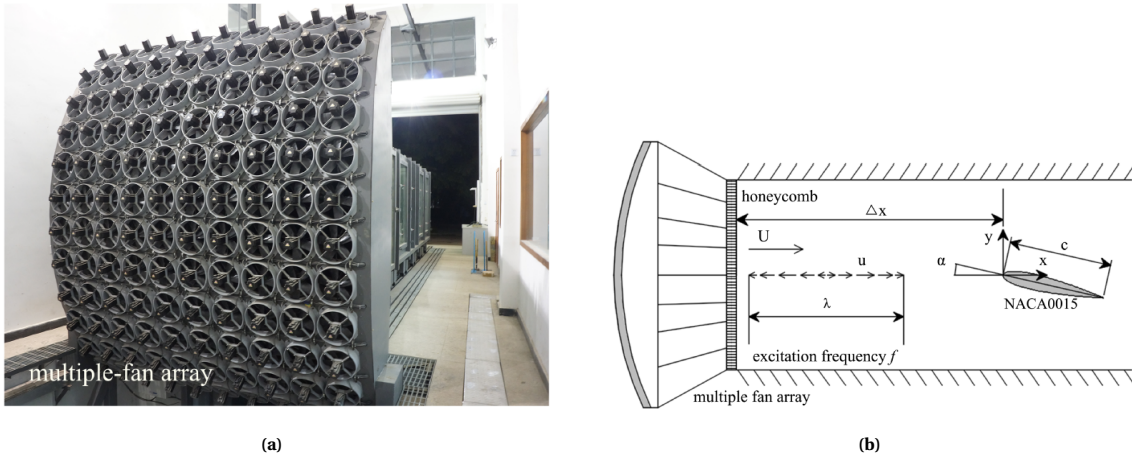


Figure 2.15: The multi-fan wind tunnel of State Key Laboratory of Disaster Reduction in Civil Engineering at Tongji University, Shanghai, China (a) and the schematics of the facility (b) [12]

The model was a NACA 0015 profile of chord length $c = 0.3$, tested under gusts with mean velocity of 10 m/s, a gust amplitude to mean velocity ratio of 0.2, and modeled after Equation 2.3 at 0.3 Hz, 0.6 Hz, 0.9 Hz, and 1.2 Hz. These values correspond to reduced frequencies of $k = 0.0471, 0.0942, 0.1413,$ and 0.1884 ; the first one is considered to describe a quasi-steady flow, while the other three, an unsteady flow. Figure 2.15a presents the time history of the measured gust, and its amplitude spectrum, showing a peak at the given frequency of 0.3 Hz and proving that the flow field is oscillating at the operating frequency of the fans. However, the time series and amplitude spectrum of the other tested frequencies are not shown.

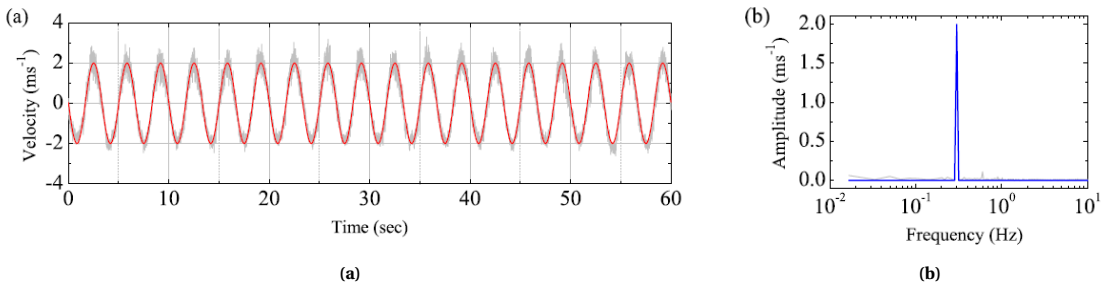


Figure 2.16: The sinusoidal streamwise gust time history (a) and the corresponding Fourier amplitude spectrum (b) at $U = 10$ m/s, $\sigma = 0.2, f = 0.3$ Hz [12]

After measuring the inflow velocity with anemometer probes and the pressure at the airfoil surface with pressure scanners, the resulting lift was computed. Based on Figure 2.17, the authors concluded that the lift fluctuation reduces as the frequency increases, reasoning that this might occur due to the reduction in the fluctuating pressure difference over the front half of the airfoil. The experimental results closely resemble the theoretical predictions at low frequencies, but diverge as the frequency increases.

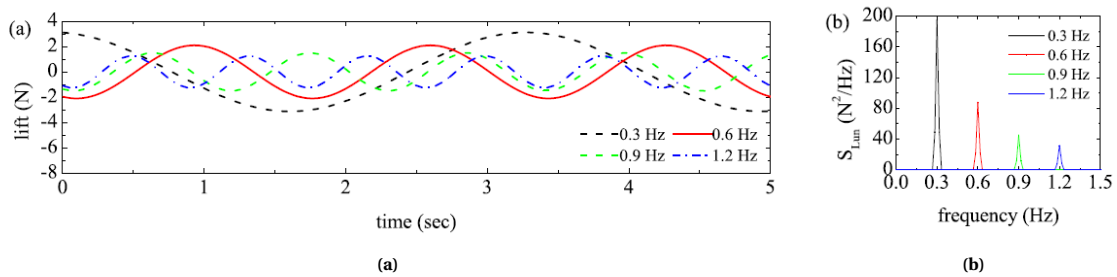


Figure 2.17: The lift time history (a) and the corresponding PSD (b) at $U = 10$ m/s, $\sigma = 0.2$

As previously mentioned, multi-fan systems are also employed in research on drone control under unsteady wind conditions characteristic of the surface layer. Several systems have been developed for this purpose in open environments, and are presented below.

In their work, [17] attempted the development and characterization of a 11 x 10 fan array of 80 mm computer cooling fans (Figure 2.18a). The ultimate aim is to simulate gust and shear layer flow for micro & nano air vehicles (MAVs and NAVs), and evaluate their response. The particularity of this system is given by the control strategy of the fans: not individual, but collective. The fans are grouped in "banks" of 2 or 3 rows, as shown in Figure 2.18b. However, this is only a matter of choice and does not differ qualitatively from the other systems presented so far. The data of the results discussed below were measured with a hot wire probe.

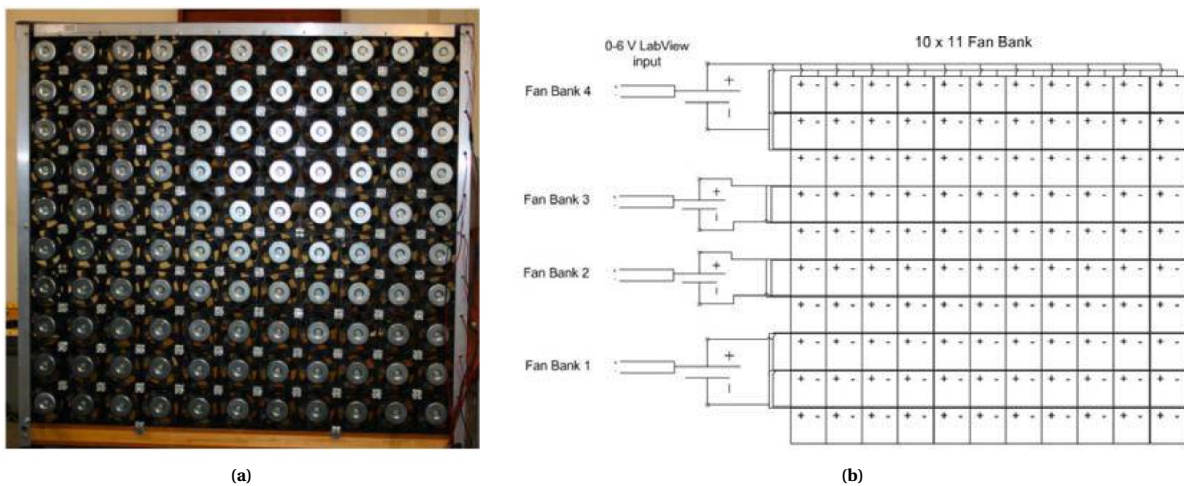


Figure 2.18: The multi-fan system developed by Johnson & Jacob [17] (a) and the control schematics (b)

Arbitrary ABL profiles and single step-change gusts were simulated to test the capabilities of the system. For the first mentioned, a series of tests were conducted. The first option was to switch the fans from 0 (off mode) to 6V (on mode) in different scenarios, such as arbitrary banks turned on, 2 neighboring banks turned on, or 1 bank turned on (Figure 2.19a). In this scenarios we distinguish peaks in velocity at the level of the corresponding banks, while the ones turned off reflect flat profiles that suggest backflow. The other option was to adjust each bank at a different voltage and notice the resulting mean velocity profile (Figure 2.19b). In this case, a decay in velocity is observed at the upper edge of the fans, where the banks both operate at 6V, and thus the velocity should be equal. The reason might be the interaction of the flow with the ambient air, leading to shear flow. Although only these two scenarios are presented here, many other profiles were simulated and reported in the work.

The generation of gust focused on sudden step changes in the voltage input, referred by the authors as sharp-edged gust, that should lead to gust profiles similar to the EOG, or ramp increase in the voltage input followed by sudden turn off, resulting in constant acceleration of the flow succeeded by momentum loss. Figure 2.20 is an example for the latter-mentioned gust modulation, in which the voltage variation is represented by the continuous blue line, while the corresponding velocity fluctuations by the red line. It can be inferred that the acceleration relatively follows the increasing ramp of 2s, while the deceleration of the flow to rest takes around 7 s. The results of the sharp-edged gusts (not shown here, but available in the original project) point to the same characteristic: the decay time of the flow velocity is usually longer than the voltage input.

The authors tested two sinusoidal variations in voltage as well, one at a "low frequency", and one at a "high frequency", but they are not mentioned. The flow response can be seen in Figure 2.21. It seems that, for the same voltage amplitude range, if the input frequency is increased, the mean velocity decreases, and the velocity fluctuations shrink: in Figure 2.21a the variations seems to be of 1 m/s, whereas in Figure 2.21b of 0.5 m/s. Although the tested frequency values are not provided, the authors conclude that the fan frequency response is of the order < 1 Hz.

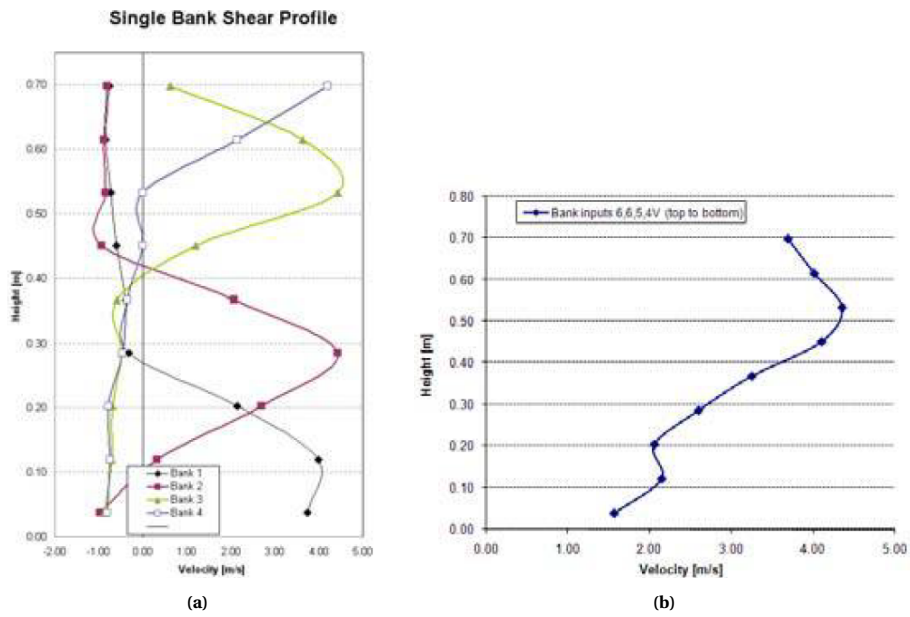


Figure 2.19: Measured mean velocity profiles generated by (a) switching the banks from 0 V to 6 V one by one and (b) adjusting the fans manually (6-6-5-4- v) to generate a linear shear flow [17]

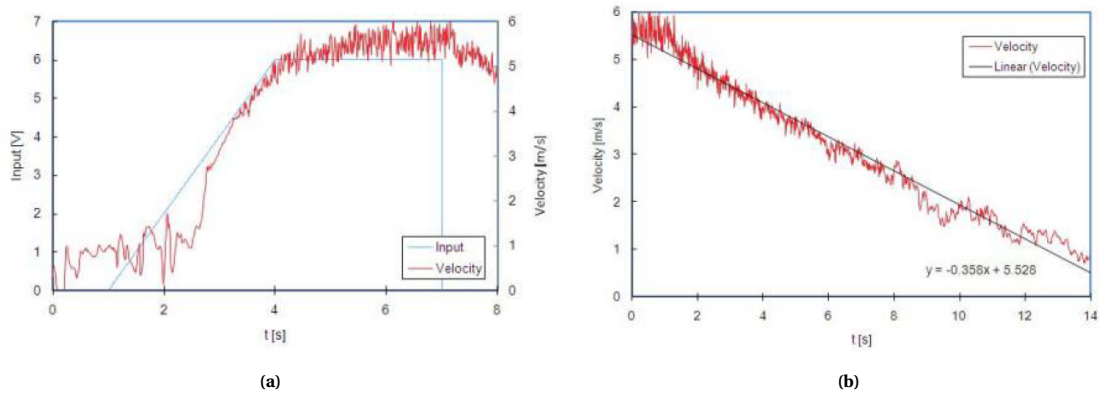


Figure 2.20: Velocity response to a 2 s ramp up (a) and to turn off (b) [17]

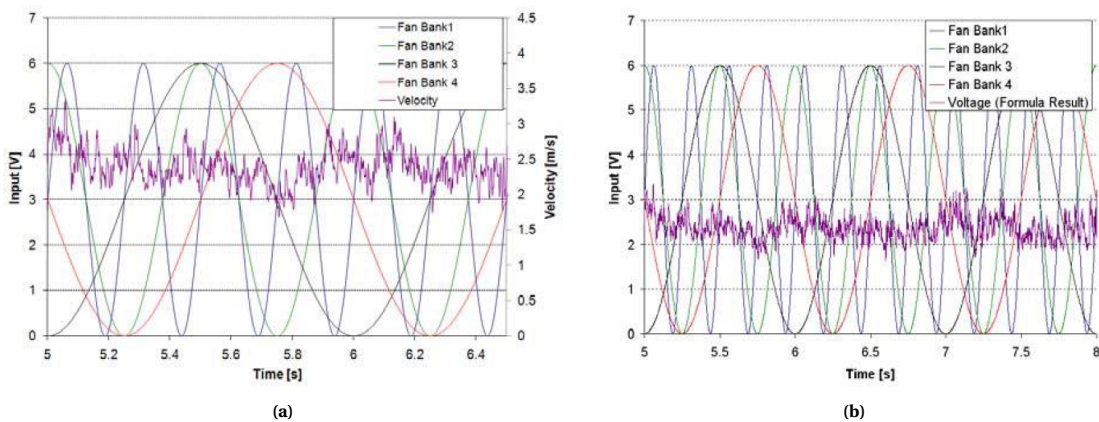


Figure 2.21: Measured velocity at a low operating frequency (not mentioned) (a) and a high operating frequency of the fans (b) [17]

A more recent multi-fan wind generation facility (Figure 2.22) was developed by the MAV Lab of TU Delft [13], in order to assess the wind resistance and power consumption of two MAVs in gusty conditions. It consists of 135 computer fans arranged in 15 modules of 9 fans each, controlled by PWM signal. They simulated simple sinusoidal gusts at 0.5 Hz, 0.25 Hz and 0.125 Hz by continuously changing the duty cycles from 50% to 100%. No reports on the properties of the resulted signal were provided.

Before conducting the experiments with the two flying models, the flow field uniformity and turbulence were preliminarily examined 1 m away from the system, first with the ProCap system [31], by instantly scanning the cross-section with an optical probe, then with 15 airflow thermistor-based sensors [32] positioned as depicted in Figure 2.23. Overall, the maximum velocity reached is 3.4 m/s. The results of the flow characterization are reported as follows.



Figure 2.22: The multi-fan system of MAV Lab and the ProCap system [13]

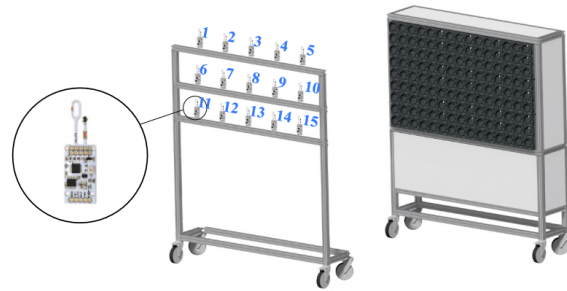


Figure 2.23: The grid of thermistor-based sensors used for the velocity measurement [13]

Figure 2.24a shows the flow envelope after scanning it with the ProCap system, when all the fans operate at full rotational speed. The mapped field 1 m downstream from the system shows an extended area of flow around 3 m/s, and reduced velocity at the boundaries, due to the mixing with the ambient air. On the other hand, the velocity measured with the sensors, plotted in Figure 2.24b, shows otherwise. Only the velocity at points 7, 8, 9 (corresponding to the middle of the system, as sketched in Figure 2.23) seem to present consistent values for almost all duty cycle but 100 %, suggesting that this is the sole uniform region. The velocity at the other points forming the upper edge (1, 2, 3, 4, 5), the lower edge (11, 12, 13, 14, 15), the left-side edge (1, 6, 11) and the right-side edge (5, 10, 15) exhibit fluctuations, marking the presence of the shear layer (similar to the observations made for [17]).

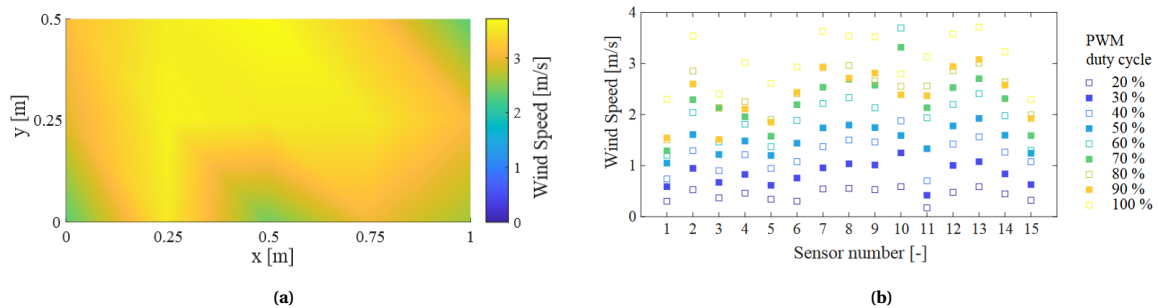


Figure 2.24: The mean velocity field measured with (a) ProCap and (b) thermistor-based sensors [13]

One work that, besides assessing the temporal scales of the flow through pointwise measurements, also characterizes the spatial scales of the full flow field at several location downstream to the system using the particle image velocimetry (PIV) technique was conducted by [33]. They developed a multi-fan system to investigate drone stability under gusty conditions, but the initial milestone was to analyze the aerodynamic characteristics of the full flow field generated by operating the fans at the same speed. The system consisted of 10 x 10 small axial-flow, dual-stage counter-rotating fans arranged in 25 x 4 modules (Figure 2.25). Each fan in controlled by regulating the PWM signals through an Arduino Mega host controller. The flow was measured

using three techniques: planar 2D2C PIV on a vertical streamwise plane of length $0.1 \leq X/h \leq 3$, where H is the width of the system; stereo 2D2C PIV on two cross-sections located at H and $2H$ downstream; hot-wire anemometry (HWA) at four cross-sections close to the system, with a spatial resolution of 5 mm in both directions. The two flow fields generated by controlling all the fans at 50% and 100% duty cycle were compared. Only for the hot-wire measurements, the fans were set at 80%, to avoid overheating the wire.



Figure 2.25: The small fan-array wind generator used in [33]

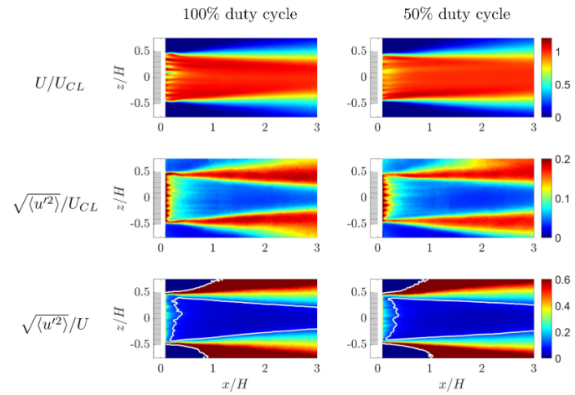
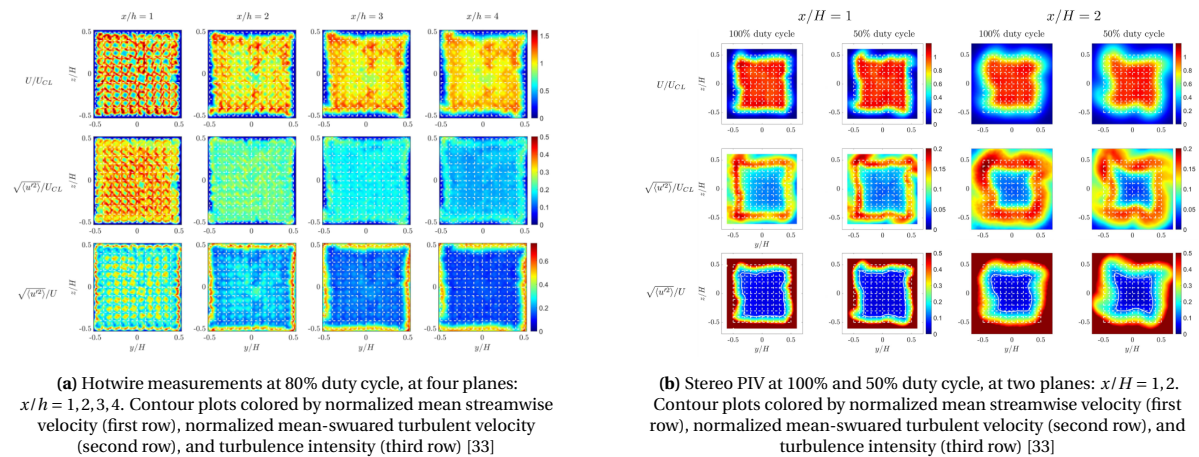


Figure 2.26: Planar PIV measurements at 100% and 50% duty cycle. Contour plots colored by normalized mean streamwise velocity (first row), normalized mean-squared turbulent velocity (second row), and turbulence intensity (third row) [33]

The maximum speed attained by the system is 12.24 m/s at 100% duty cycle, and 4.43 m/s at 50% duty cycle. Based on the contour plots shown in Figure 2.26, Figure 2.27a and Figure 2.27b, the following observations were made. First of all, the flow generated at 50% and 100% show similar characteristics, which can be assumed to be true for any other duty cycle. Then, in the field close to the system, "swirling jets" of high momentum form due to the rotation of the fans, while the far field presents characteristics similar to the subsonic jet: the decay of the core region due to the expansion and distortion of the outer shear layer. The core presents turbulence intensity around 10%, over an area about 36% of the cross-stream plane at $2H$, dropping at 25% at $3H$ downstream. There are no indications on the spatial uniformity of the flow. The study also presents the energy spectra of the velocity signal, showing that the flow produced by the fans exhibits a wide range of turbulent scales (not shown here).



(a) Hotwire measurements at 80% duty cycle, at four planes: $x/h = 1, 2, 3, 4$. Contour plots colored by normalized mean streamwise velocity (first row), normalized mean-squared turbulent velocity (second row), and turbulence intensity (third row) [33]

(b) Stereo PIV at 100% and 50% duty cycle, at two planes: $x/H = 1, 2$. Contour plots colored by normalized mean streamwise velocity (first row), normalized mean-squared turbulent velocity (second row), and turbulence intensity (third row) [33]

Figure 2.27: Contour plots of the near field (a) and far field (b), as assessed by [33]

The authors conclude that the flow quality should be improved. More specifically, the turbulence intensity and the annular shear layer should be reduced by adding honeycomb meshes in cross-planes and vortex generators at the edges to reduce the outer shear layer.

All of the multi-fan array wind generators introduced so far were developed in-house. Since most of the elements (fans, control units, structure) are off-the-shelf and accessible, the system is a low-cost alternative to the traditional wind tunnel. The knowledge transparency within the community of multi-fan system users could only enhance its capabilities of reproducing unsteady flow. Simultaneously, WindShaper [10], an open-facility multi-fan system, was patented and launched in 2017 for commercial use. The motivation was the same as per the other systems discussed so far: free flight drone testing in controlled conditions that could mimic the environmental unsteadiness drones are normally subjected to.

The WindShaper facility (Figure 2.28) consists of other elements apart from the fan modules, such as the motion tracking camera system, the user interface, the sensors, the drone. The uniqueness of this technology is given by the inter-connectivity between all these elements through a network that facilitates the storage and handling of the test data. WindShaper itself comes in various custom sizes and layouts, depending on the requirements of the experiment. The wind profiles it is capable to replicate span from uniform to shear flow [34], and gusts (constant sinusoidal or semi-random, arbitrarily distributed among the fans [35]), with a maximum operating frequency of the fans of 0.5).

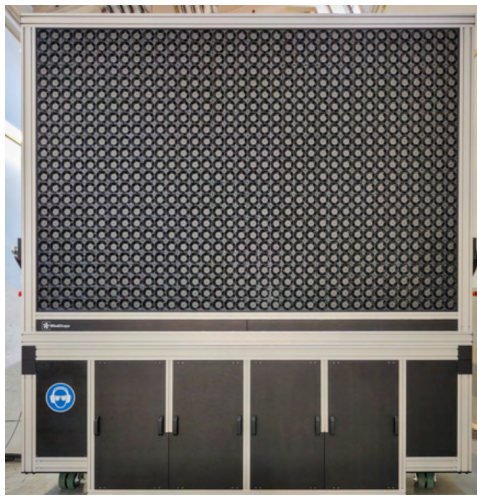


Figure 2.28: The WindShaper system [35]

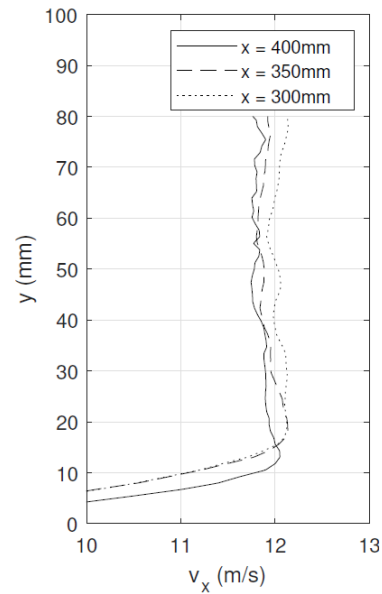


Figure 2.29: Modulated boundary layer by fine-tuning the bottom row of fans. [34]

The experimental applications that use its capabilities range from free flight testing of drones, propeller testing, weather testing, and combinations of those [36]. More recently, the utility of the system was highlighted through works such as the investigation of the ground effect on a finite-span wing and boundary layer modulation by tuning the fans [37]. The boundary layer generated [34] is reported to closely resemble the profile predicted by the boundary layer theory. The results shown in Figure 2.30 are a valid demonstration not only of the capabilities of WindShaper, but of multi-fan systems in general.

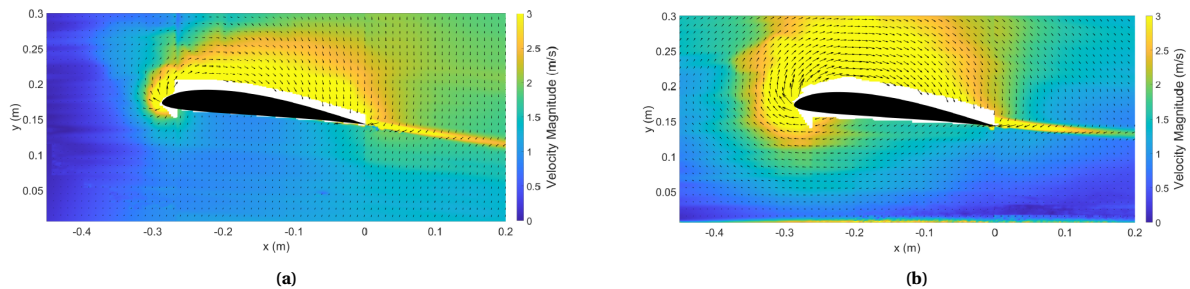


Figure 2.30: Velocity field around the wind when operating in free stream (a) and near the ground (b)

2.4. Particle Image Velocimetry

PIV is a widely used measurement technique that offers a quantitative understanding of the velocity field. Although it involves a complex setup consisting of different subsystems that require specific know-how, equipment calibration is not necessary, and the measurements are non-intrusive.

Depending on the purpose of the experiment, different setups can be employed. To measure the 2 velocity components in a 2D domain, a planar PIV layout is used, while the 3 velocity components of a 2D field can be obtained with a stereoscopic arrangement. If the output is desired to give information on the 3 velocity components of a 3D fluid domain, then tomographic PIV is chosen. The following subsection introduces the general working principle, while the second subsection emphasizes the characteristics of the two methods.

2.4.1. Principle of PIV

With PIV, the velocity field is obtained indirectly by measuring the displacement of tracer particles within a laser sheet. The process and apparatus are displayed in Figure 2.31 and are similar for both methods. Discharged in the moving fluid by a seeding machine (not shown), the tracer particles are illuminated twice by a laser, which is synchronized with the imaging device to obtain the position of the particles at two instances in time. Once the image pairs are acquired by the data acquisition system, (Figure 2.32 (1)), a cross-correlation algorithm is applied locally between two frames of a pair (2). The correlation map unveils the local displacement of the particles, which is further processed to obtain the velocity vector (3).

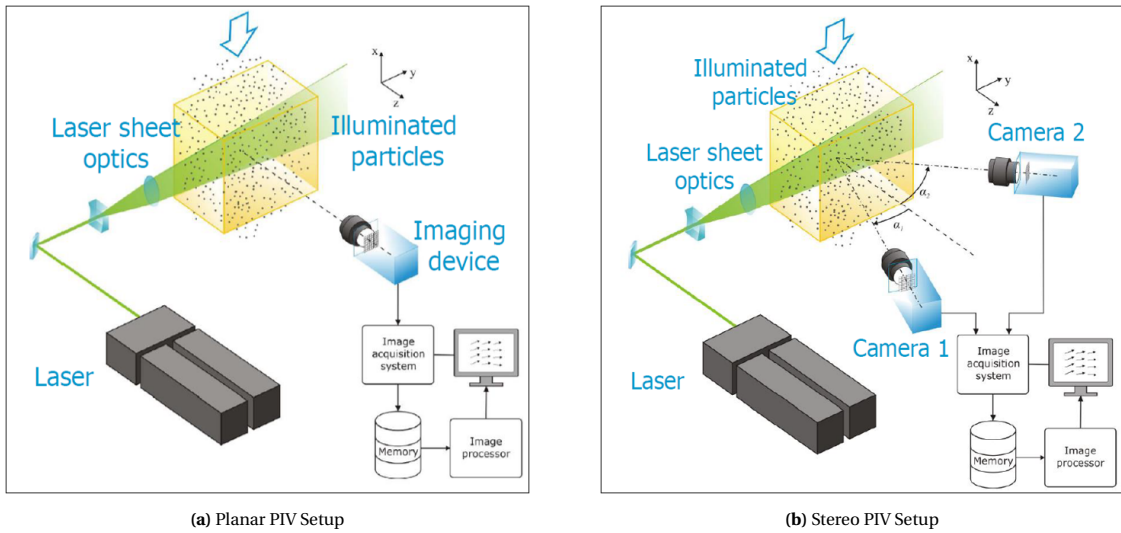


Figure 2.31: Standard PIV setup consisting of the following subsystems: illumination (laser), imaging device (differs per method), seeding machine (not shown), and data acquisition system. (a) Planar PIV and (b) Stereo PIV. Figures reproduced from [38]

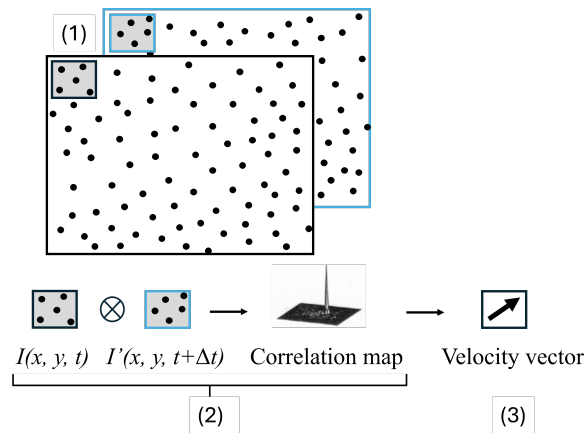


Figure 2.32: PIV measurement data processing

2.4.2. Planar & Stereo PIV

Camera arrangement

If we look again at Figure 2.31, we see that on the left-hand side there is only one camera facing the flow illuminated by the laser sheet, i.e the lens plane is parallel to the flow direction. With this positioning, the camera is able to capture the in-plane displacement vector field of the 2D flow domain, which is further processed into two velocity components. On the right-hand side, two cameras are placed under different angles, providing stereoscopic viewing. The images captured by them are processed separately to retrieve the two-component vector fields, which are then combined to obtain the out-of-plane vector as well. Thus, this method allows also for the calculation of the 3rd velocity component of the 2D domain.

In the stereo arrangement, since the cameras are obliquely positioned with respect to the object plane, the latter will be out of focus. The lenses are therefore adjusted with a Scheimpflug adaptor, according to the Scheimpflug principle: the object plane, the lens plane, and the image plane should all intersect along same line (Figure 2.33, [39]).

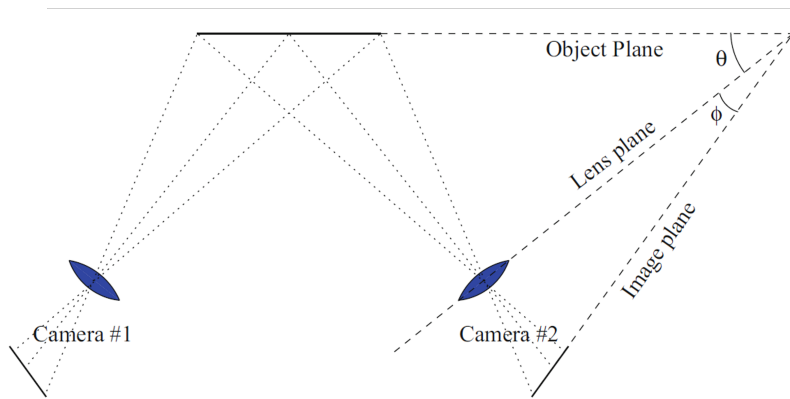


Figure 2.33: Scheimpflug arrangement. Figure taken from [39]

Image calibration

A mandatory step prior to any measurement campaign using PIV is the geometric camera calibration, done to correct the distortions induced by the lens or by the viewing position. Another functionality is to determine the physical parameters of the camera, like the position relative to the object plane, or the viewing angle. This step assures that the velocity components are properly projected and scaled on the illuminated measurement plane.

In addition to this, stereo PIV requires a correction of the misalignment between the laser sheet and the de-warped images, called disparity correction, or self-calibration [40]. This step reduces the overlap discrepancy between the same particle seen by the two cameras with respect to the illuminated object plane.

Optimization rules for particle image displacement

To obtain a valid displacement vector by cross-correlating the window sizes of a two-image pair, a sufficient and consistent number of image particles should exist within the window during both exposures. This can be achieved by applying the one-quarter rule [41]. With the optimized particle image displacement, the time separation between the two pulses (or two exposures) could be approximated.

Concerning the two-component velocity field obtained with planar PIV, the maximum in-plane displacement should be smaller than 1/4 of the window size. The time separation Δt in the x-direction is then:

$$\Delta t = \frac{1}{M} \frac{1}{4} \frac{\text{pixel size} \cdot \text{window size}}{u}$$

where M is the magnification factor (relating the dimension of the physical particle to the imaged one), and u is the velocity component in the x-direction.

Regarding the third velocity component measured with stereo PIV, the out-of-plane displacement should be less than 1/4 of the light sheet thickness. The time separation Δt in the x-direction should be:

$$\Delta t = \frac{1}{4} \frac{\Delta z_0}{u}$$

where Δz_0 is the light sheet thickness.

The implementation of PIV for the purpose of this thesis is exemplified in section 3.3.

2.5. Research questions & Research objectives

The literature review shed a light on the available multi-fan systems and the aerodynamic characterization of the flow to demonstrate their capabilities in producing unsteady flow typical to the ABL. Apart from the WindShaper, which has been exhaustively characterized, the in-house developed open-environment multi-fan systems lack such detailed assessments of the flow properties, since they were conducted at the level of detail and completeness based on the application and the measurement equipment at hand. Moreover, if the turbulence intensity was reported in almost all the reports, the cross-sectional uniformity was not mentioned for any of the systems.

Before the start of this project, a configuration of 3 x 3 fans and the fans type have already been decided upon. Considering the uniqueness of the systems in terms of mechanical properties of the fans, configuration, and flow control, an aerodynamic characterization of the full flow field produced by this system should be conducted, to assess its potential in generating flow fields for wind engineering applications. Therefore, through this project, we are curious about and intend to answer the following questions:

1. What are the properties (velocity and vorticity distributions, turbulence intensity, and uniformity) of the flow produced by the 3 x 3 multi-fan system with all the fans operating at the same rotational speed?

1.1 How do these properties vary at different distances downstream from the system?

2. Is the 3 x 3 multi-fan system able to produce different predefined linear wind shear profiles?

3. To what extent could the 3 x 3 multi-fan system generate a flow field that oscillates at the same operating frequency and amplitude of the fans?

3.1 How does the uniformity change depending on the frequency and amplitude?

To address these questions, the study sets the following objectives:

1. To assess the aerodynamic properties (velocity and vorticity distributions, turbulence intensity, and uniformity) of the mean flow field generated by a 3 x 3 multi-fan system operating at a constant rotational speed, by means of PIV measurements, at various downstream locations.

2. To assess whether the 3 x 3 multi-fan system is able to reproduce different linear wind shear profiles, by means of PIV measurements.

3. To investigate whether the amplitude and frequency characteristics of the induced velocity fluctuations respect the selected operating amplitude and frequency characteristics of the motion of the fans, and how these affect flow uniformity, by means of PIV measurements.

Now that the research questions and objectives have been clearly defined, the next chapter will outline the methodology used to address them, providing a structured approach for the reader to follow. Following this, chapter 4 will showcase the results of the investigation.

3

Methodology

The aim of this chapter is to guide the reader through the methodology used to achieve the research objectives. It begins by introducing the multi-fan system in the first section. The focus falls on its relevant characteristics, and also on how it can be controlled to generate the desired types of flow. These are: the uniform flow, the boundary layer flow, and the gust, defined in the second section, along with the test cases. The measurement planes are explained and illustrated in the third section. Then, the fourth section presents the PIV experiment setup and its instrumentation, along with the test matrix of each flow case. Finally, the measurement data processing and analysis tools are unveiled in the fifth section.

3.1. Multi-fan System Characteristics & Control

This section underlines the main object of this thesis: the multi-fan system wind generator prototype. The first subsection introduces the elemental design, electrical and operational characteristics of the multi-fan system, while the second subsection explains how the fans are controlled as a unit in Arduino, to generate the desired flow.

3.1.1. Fan & Unit characteristics

Design characteristics

We define the multi-fan system (MFS) unit, or prototype, as a 3 x 3 grid of axial, clockwise rotating fans, as seen in Figure 3.1, along with the essential dimensions in Table 3.1. The fan model is ebm-papst 4314 N/2HRP [42].

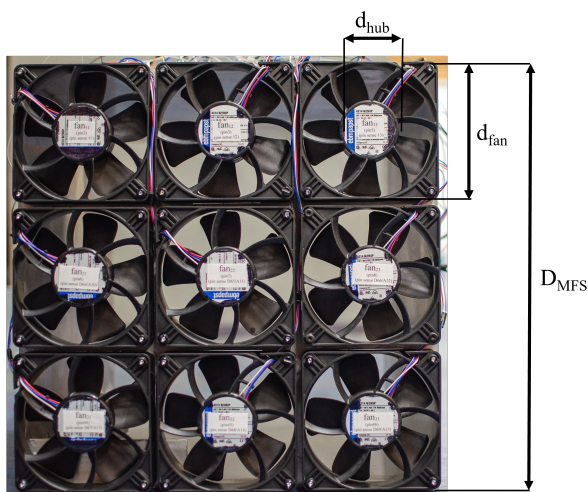


Figure 3.1: The multi-fan system unit and its main dimensions.

Table 3.1: The multi-fan system dimensions

Parameter	Length [mm]
Fan diameter, d_{fan}	119
MFS length, D_{MFS}	360
Hub diameter, d_{hub}	50

A stainless steel housing was custom-made as support structure for the fans, containing an inner and an outer case (Figure 3.2). The fans are fixed to the inner case, which can, if needed, be slid within the outer case. Besides this functionality, the entire structure can also be attached to and stabilized on the experiment stand, as seen later in section 3.3.

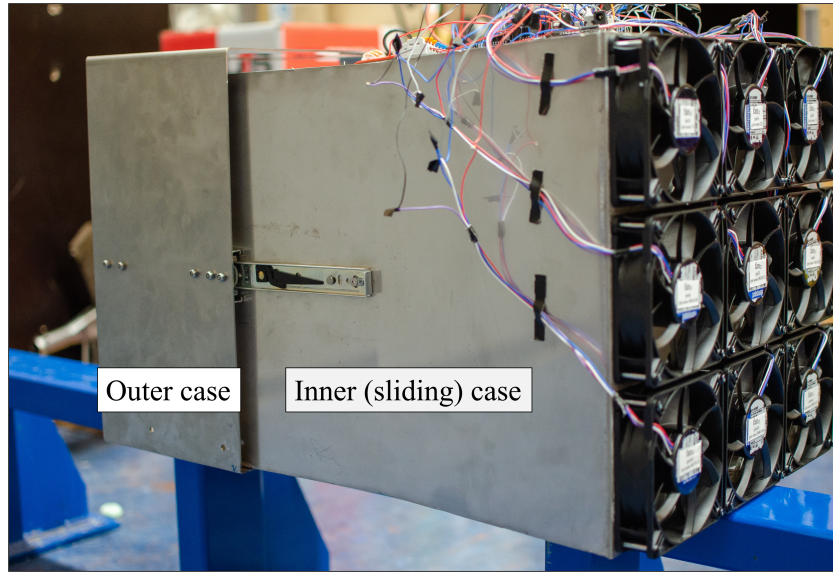


Figure 3.2: The stainless steel housing of the MFS, comprising an inner and an outer case.

Electrical & operational characteristics

In order for the fans to function independently, but also as a unit, they have to be connected to a power supply through an electrical installation. Since a description of it is beyond the scope of the thesis, the wiring diagram can be consulted in the appendix, section A.1.

To ensure the correct functioning of the system during the experiment, the electrical and mechanical capabilities of the fans after being connected to the circuit were checked. The control of the fans is facilitated through an Arduino Mega 2560 board by pulse-width modulation (PWM) electrical signal, modulated by giving the duty cycle (percentage of the nominal voltage) as input in the Arduino IDE software. Therefore, power, current and speed readings were conducted for each fan operating under 10 duty cycles, from 10% to 100%, at the typical PWM frequency of 25kHz and the nominal voltage of 24V. The power and current drawn by each fan were compared with the reference values of a fan functioning at the maximum duty cycle of 100 % (Table 3.2), and validated. The power and current consumption of the entire unit can be found in appendix, section A.2. The speed reading tests are explained in the following.

Parameter	Value/Description
Typical PWM Frequency	25kHz
Nominal Voltage	24 V
Power Consumption	11 W
Tolerance	$\pm 12.5\%$
Current Consumption	460 mA
Tolerance	$\pm 12.5\%$
Maximum Speed	4050 RPM
Tolerance	$\pm 7.5\%$

Table 3.2: Electrical & mechanical operating features of one fan at 100 % duty cycle. Information taken from the product data sheet [42]

In Arduino IDE, the RPM value sent back to the board by the tachometer of each fan was read. In this way, the response of each fan could be correlated to the duty cycle input and checked with the product data sheet

[42]. Figure 3.3 is the resulting dependency, which fully matches the one provided by the product data sheet. The sole observation is the slight change in the startup duty cycle value, compared to the documentation: according to it, the startup of the fans occurs at 15%, while our observations suggest it is at 10% of the nominal voltage. The specific reasoning is uncertain, but it might be due to systematic differences. However, the RPM readings were found to be fully consistent with the readings in the documentation at all the mentioned duty cycles, thus the wiring setup was validated. Moreover, considering the 10% duty cycle is viable, we included it in the operational range and used it as a test case in the measurement campaign.

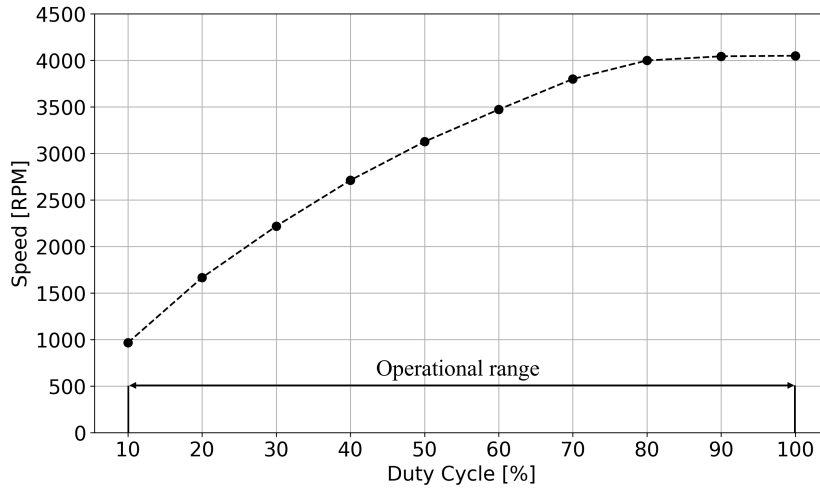


Figure 3.3: Duty Cycle VS Speed at $f_{PWM} = 25$ kHz and $U_n = 24$ V

The following subsection focuses on the user control over the rotational speed of the fans.

3.1.2. PWM control with Arduino

To facilitate user control in operating the fans at different duty cycles, the fans are connected to an Arduino Mega 2560 board, and controlled through Arduino IDE on a computer. As this project is the first iteration in manufacturing and characterizing the multi-fan system, it was decided to have a simple starting point in controlling the fans for the different flow cases. Because of this, two main codes, or sketches, were developed in Arduino IDE: one sets the constant rotation of the fans, needed for the steady-state uniform and boundary layer flows; the second one varies the duty cycle in time, respecting a predefined discrete sinusoidal profile used to generate gust. In both codes the user communicates with the Arduino board by sending duty cycle values as input through the Serial Monitor. Depending on the flow case, the input requirements differ. A detailed explanation of the flow cases is given in section 3.2.

Constant duty cycle: uniform mode & boundary layer mode

Figure 3.4 represents a screenshot of the Serial Monitor used to send commands to the Arduino board for both the uniform and shear flow cases. As indicated, it requires separate input for each row of fans. To set all the fans at the same speed, the same duty cycle value is given each time. Otherwise, for boundary layer flow generation, each row is given a different value. The full sketch can be checked in section B.1.

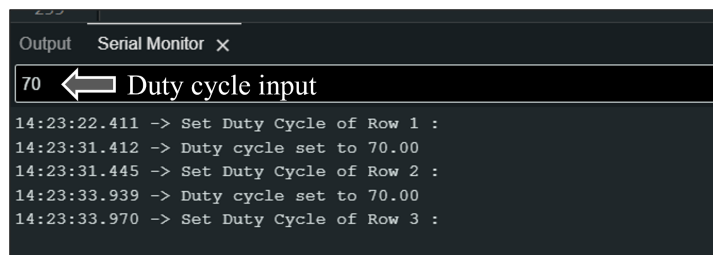


Figure 3.4: Example of Serial Monitor input for constant duty cycle. The current requirement is a duty cycle value for Row 3.

Time-varying duty cycle: gust mode

The sinusoidal duty cycle variation which generates gust is implemented in a similar straightforward manner in the Serial Monitor. Additionally, it demands predefining the sinusoidal profile (Equation 3.1) in another programming language (Figure 3.6a). In the serial monitor, the user needs to input a single line containing a sequence of the duty cycle values, as exemplified in Figure 3.5. The last value of the line is the time step between the samples, or the sampling period of one cycle. Once the sequence is sent to the Arduino board, the profile can be visualized in the Serial Plotter (Figure 3.6b). The Arduino sketch is provided in section B.2.

$$\text{duty cycle}(t) = \text{duty cycle}_{\text{mean}} + \text{duty cycle}_{\text{amplitude}} \sin(2\pi f_{\text{MFS}} t) \quad (3.1)$$

where f_{MFS} is the selected operational frequency of all the fans.

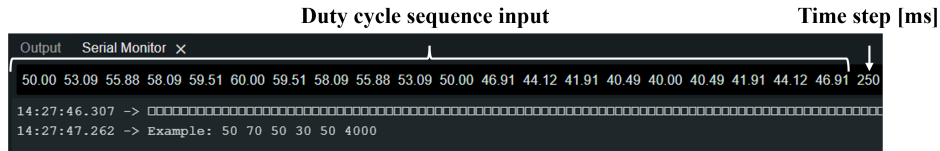
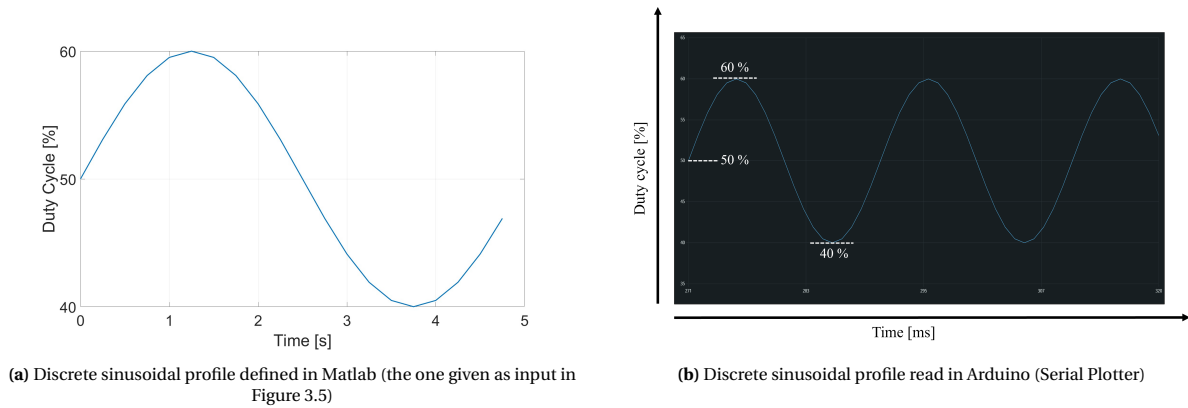


Figure 3.5: Example of Serial Monitor input for the gust case. The duty cycle sequence reconstructs a sine wave with the mean at 50% duty cycle, and amplitude of 10% duty cycle (the max. and min. visible in the sequence are 60% and 40% duty cycle).



(a) Discrete sinusoidal profile defined in Matlab (the one given as input in Figure 3.5)

(b) Discrete sinusoidal profile read in Arduino (Serial Plotter)

Figure 3.6: Example of sinusoidal profile as prescribed in Matlab and as received in Arduino.

3.2. Test cases

Now that the prototype is set up, the attention shifts on the selection of the test cases. These represent the experimental duty cycle conditions under which the MFS operates to generate the desired flow, and will be referred to as uniform mode, boundary layer mode, and gust mode. The following sections establish the test cases of each flow case corresponding to the MFS mode.

3.2.1. Uniform flow

We are interested in characterizing the flow generated by setting all the fans of the MFS at equal, constant duty cycles in time. This condition is defined as the *uniform mode* of the MFS. The entire operational range is chosen, thus the experiments for uniform flow generation are conducted at 10 duty cycles, from 10% to 100%.

3.2.2. Linear shear flow

The second objective of this research is to determine whether the prototype can generate linear shear profiles. To achieve this, each row of fans operates at a distinct duty cycles, increasing from the bottom to top while remaining constant in time. For the experiment, two group cases are established: baseline 1, and baseline 2, both modeled by a number of variations. They represent the uniform mode of the MFS at 40% and 70% duty cycle, respectively. To induce shear flow, the duty cycles of the top and bottom fan rows are adjusted relative

to the middle row, set at the corresponding baseline value. Specifically, the duty cycle of the upper and lower rows is chosen to be increased or decreased in increments of 2.5%, 5% and 10%. With these variations, the two baseline group cases span from 30% to 50% for baseline 1, and from 60% to 80 for baseline 2, covering the lower-to-middle, and higher duty cycle regimes.

Active fans	Baseline 1: 40%			Baseline 2: 70%		
	Step 2.5%	Step 5%	Step 10%	Step 2.5%	Step 5%	Step 10%
Top row	42.5	45	50	72.5	75	80
Middle row	40	40	40	70	70	70
Bottom row	37.5	35	30	67.5	65	60

Table 3.3: Test cases of the MFS boundary layer mode: the two baseline cases and the test ranges corresponding to the duty cycle increments.

3.2.3. Gust

The third point of interest is to assess whether the frequency of the generated gust respects the frequency of the motion of the fans, and whether the velocity signal of the gust matches the velocity amplitude corresponding to the given duty cycles. The selection of the test cases is presented in Table 3.4. All the fans follow simultaneously the input duty cycle sequence.

f_{MFS} [Hz]	$A_{\text{mean, MFS}}$ [%]	A_{MFS} [%]	$A_{\text{range, MFS}}$ [%]
0.2, 0.4, 0.8	50	10	40 - 60
0.2, 0.4, 0.8	60	20	40 - 80
0.2, 0.4, 0.8	50	30	20 - 80

Table 3.4: Test cases of the MFS gust mode. The operating conditions of the fans are given by three frequencies: 0.2Hz, 0.4Hz and 0.8Hz, and three amplitudes: 10 %, 20% and 30%. The mean and range of the amplitudes are also provided.

The maximum operating frequency of the fans was limited due to the low acquisition frequency of the PIV measurements (8Hz - detailed later, in subsection 3.3.4). Using a measurement technique with a higher sampling frequency, like hot wire anemometry, would allow the extension of the f_{MFS} to higher frequencies. However, the literature review has shown that studies reported frequencies of up to 1 Hz, with lower values being relatively unaffected by fans inertia. Thus, until a thorough mechanical characterization of the fans is conducted to map the entire range of operating frequencies, the chosen ones could be considered within the range and useful for testing. Another aspect to be mentioned is that although the minimum and maximum duty cycles are equally distanced from the mean, the resulting velocities might be slightly disproportional, due to the nonlinearity of the relation between the duty cycles and the rotational speed. This will be verified in chapter 4.

3.3. Experiment Setup

The High Speed Laboratory of the Faculty of Aerospace Engineering offers the necessary equipment and technical expertise to undergo experiments using PIV. The measurement campaign was performed in the room of the W-tunnel. However, since the MFS is mobile and independent of a wind tunnel, any room large enough that complies to a number of safety requirements, depending on the measurement technique used, can also be considered suitable for experiments with the system.

The following four subsections provide a concise overview of the preparatory steps. The first subsection focuses on choosing the measurements planes that would best aid in assessing the flow field. The second and third subsections describe the planar and stereo PIV equipment and the corresponding calibration parameters. The section ends by framing the test matrix for each flow case.

3.3.1. Measurement planes

The measurement planes reflect a considerable part of the strategy shaped to fulfill the research objectives. More specifically, their location and orientation reveal different insights of the flow field, thus choosing them carefully can lead to satisfying results. Figure 3.7 illustrates the five planes chosen for this experiment, commented in the following.

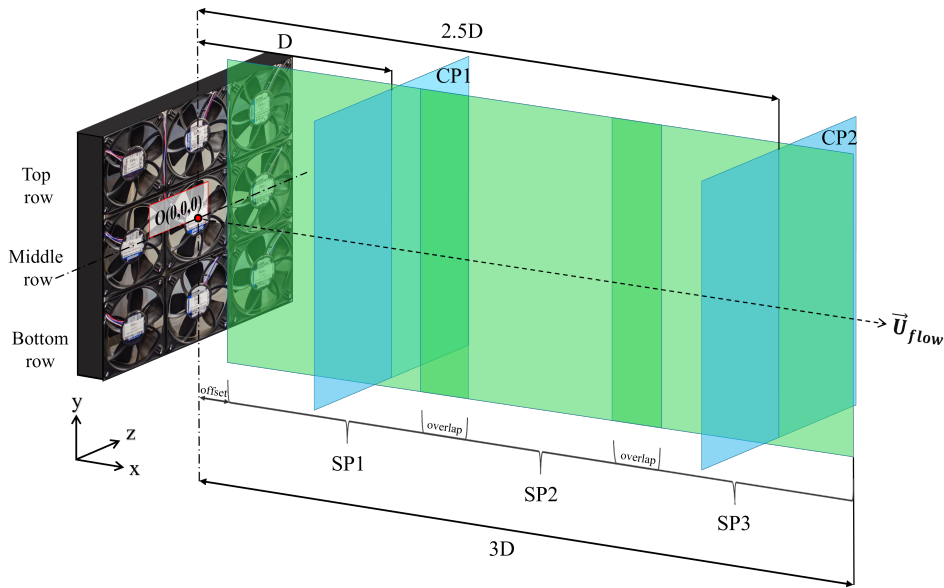


Figure 3.7: Measurement planes

The first three green vertical planes placed at the centerline of the MFS are the *streamwise planes* (*SP*), and the velocity fields are recorded here with planar PIV. Furthermore, the different regions of the flow field corresponding to the location of the vertical streamwise planes will be later mentioned as: the near field (*SP1*); the middle field (*SP2*); the far field (*SP3*). Similarly, the two blue planes parallel to the MFS are denoted as *cross planes* (*CP*), and the flow fields measured here are reconstructed with stereo PIV. The positions of the cross planes were proposed after visualizing the preliminary mean velocity fields of the streamwise planes. Due to time constraints, a cross plane in the middle field was skipped.

As mentioned, the planes were selected based on the flow data intended to be analyzed. To learn about the spatial evolution of the flow in the downstream direction (mean velocity distributions, vertical streamwise velocity and turbulence intensity profiles), the three vertical streamwise planes can offer extensive such information. To gain insights on the spatial uniformity in cross-stream section or the swirl induced by the fans, the two cross planes are used.

Knowing the test cases and the measurement planes allows us to set up the experiment layout accordingly. This stage is covered in the next subsection.

3.3.2. Planar PIV setup

With planar PIV we aimed to recreate a panoramic view of the vertical streamwise plane crossing the center-line of the MFS. Figure 3.8 shows the planar PIV setup. The contraction zone of the wind tunnel was removed to make more space for the desired layout.

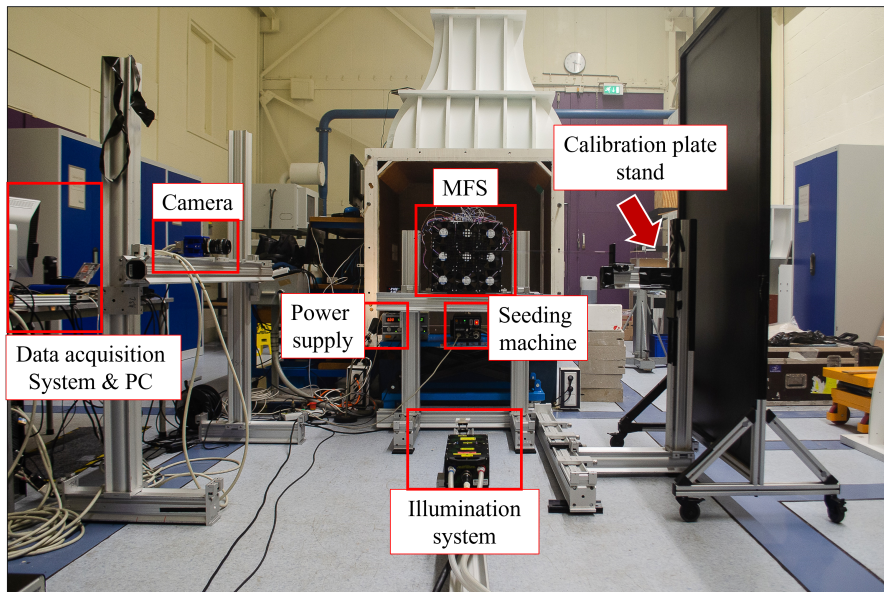


Figure 3.8: The planar PIV setup and instrumentation.

MFS & support stand

In section 3.1 we presented the array of fans assembled on a metal housing. During the experiment, the outer case was stabilized on the support stand by two corner brackets, as suggested in Figure 3.9. Moreover, to avoid any wall influence, the MFS was lifted at a height of $\approx 95\text{cm}$ from the ground.

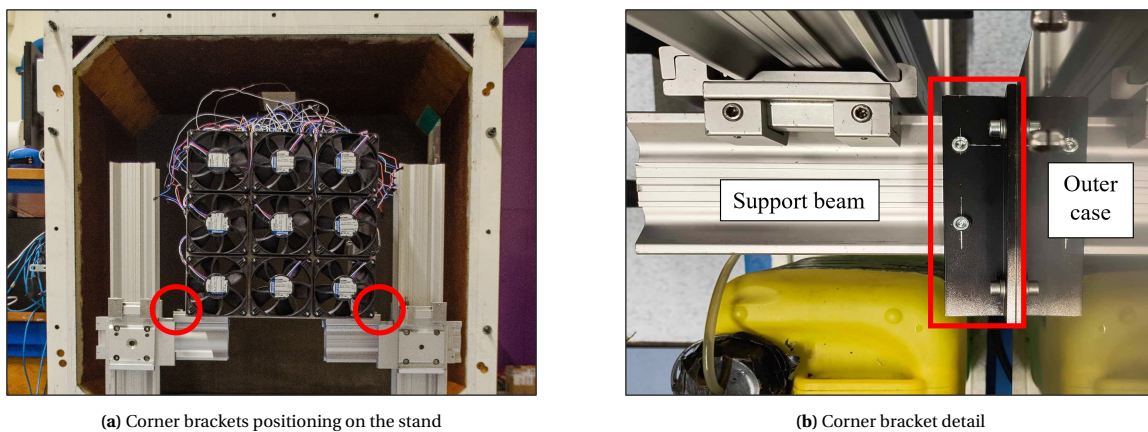


Figure 3.9: Display of the MFS mounted on the support stand with corner brackets

Illumination system

It consists of the *Quantel Evergreen 200* double pulsed Nd:YAG laser. The energy in each laser pulse is 200 mJ at maximum power. The two cavities produce infrared light which is halved to visible green light (532 nm). The maximum repetition rate for each pulse is 15 Hz. A sequence of lenses modeled the exit beam into a thin laser sheet of 3 mm thickness, aligned with the desired measurement plane, and covering the entire field of view. The laser emitter and the lens formation could be translated downstream along with the camera, according to the location of the measurement plane.

Imaging system & camera calibration

The images were acquired with the Imager sCMOS. The sensor has a resolution of 2560 x 2160 pixels with 6.5 microns pixel pitch, and can record 12-bit images. The lens used is a Nikon 35 mm focal length lens.

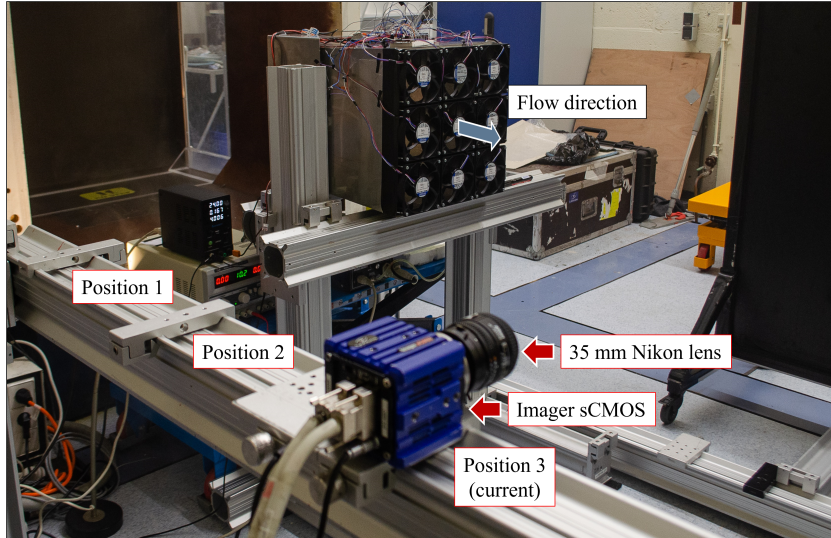


Figure 3.10: Imaging system & positioning for planar PIV

Based on the information provided so far, the imaging measurement parameters were approximated (the magnification factor, the image and object distance), which further allowed us to estimate the $f_{\#}$ yielding good particle imaging. Specifically, to have an image diameter of 2-3 pixels and the depth of field larger than the laser sheet thickness, the lens was set on $f_{\#} = 11$ during the experiments. The imaging parameters were validated with the camera information provided by DaVis 8 after the geometric calibration.

For every planar plane, the camera was translated downstream at the indicated positions in Figure 3.10. Concurrently, the laser and calibration plate were moved, respecting the same translation distance. The geometric calibration was conducted after each translation to account for any disturbance brought to the systems by moving them. Each of the three corrected fields are similar, thus Figure 3.11 displays a representative de-warped field of view scaled with respect to the symmetry axis of the MFS. Furthermore, Table 3.5 summarizes the imaging parameters.

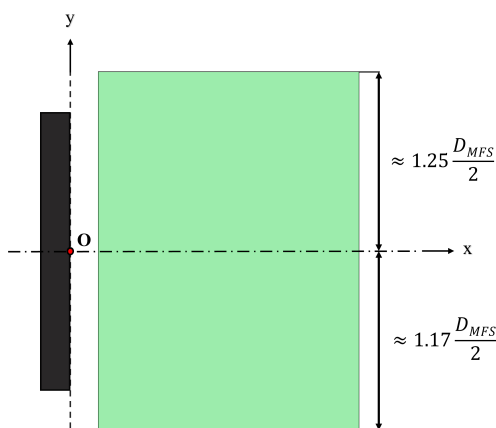


Figure 3.11: Planar PIV setup: the FOV after the geometric calibration, scaled with respect to the symmetry axis of the system

Table 3.5: Planar PIV setup: camera parameters

Parameter	Value/Description
sCMOS sensor resolution	2560 x 2160 pixels
dewarped image resolution	2191 x 2591 pixels
pixel pitch	6.5 x 6.5 microns
digital image resolution	≈ 5.8 pixels/mm

Seeding machine

We used the *SAFEX* fog generator which produces water-glycol based particles with a mean diameter of $\bar{1}$ microns. In typical wind tunnel experiments, the generator is placed upstream of the fan to ensure that seeds are uniformly distributed at the cross-section exit of the tunnel contraction. To achieve a similar uniform distribution in the flow generated by the MFS, the fog generator was positioned underneath it, with its exhaust duct directed toward the settling chamber. By filling this chamber with particles when the MFS is off, they could be evenly dispersed among the nine fans once they start rotating. This experimental seeding strategy was validated and continuously monitored throughout the campaign by observing the particle concentration in DaVis 8.

Data acquisition and processing system & PTU

The measured data was collected and processed in the commercial software DaVis 8 from LaVision. Here, we also conducted the geometric calibration and self-calibration (for stereo PIV), and set the acquisition parameters (provided for each flow case in section 3.2). This information is usually sent to the programmable time unit (PTU) which syncs the triggering signals for the laser and the camera.

3.3.3. Stereo PIV setup

In addition to the second sCMOS camera, which can be seen in Figure 3.12, the laser sheet was turned 90° to illuminate the cross-stream plane. The location of the laser respected the streamwise distances of the stereo planes illustrated in Figure 3.7.

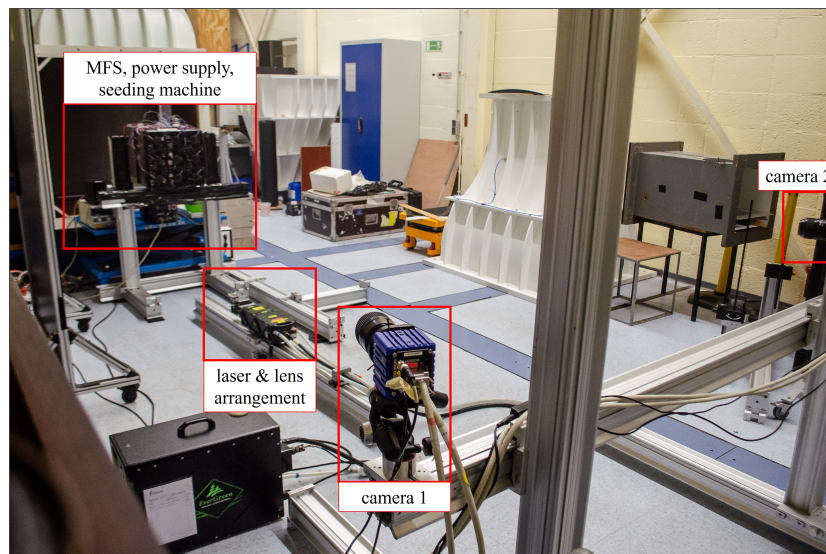


Figure 3.12: The stereo PIV setup and instrumentation

Imaging system & camera calibration

The camera equipment is shown in Figure 3.13. This time, a Nikon lens with a 105mm focal length was used. To assure the measurement planes are in focus, a Scheimpflug adaptor was fixed between the camera and the lens and adjusted correspondingly. Then, the images from both cameras had to be overlapped in DaVis 8. For better precision and to ease the process, each camera was mounted on a Manfrotto 3-way head. On the right-hand side, Figure 3.14 displays a representative dewarped field of view scaled with respect to the symmetry axis of the MFS. Furthermore, Table 3.5 summarizes the imaging parameters.

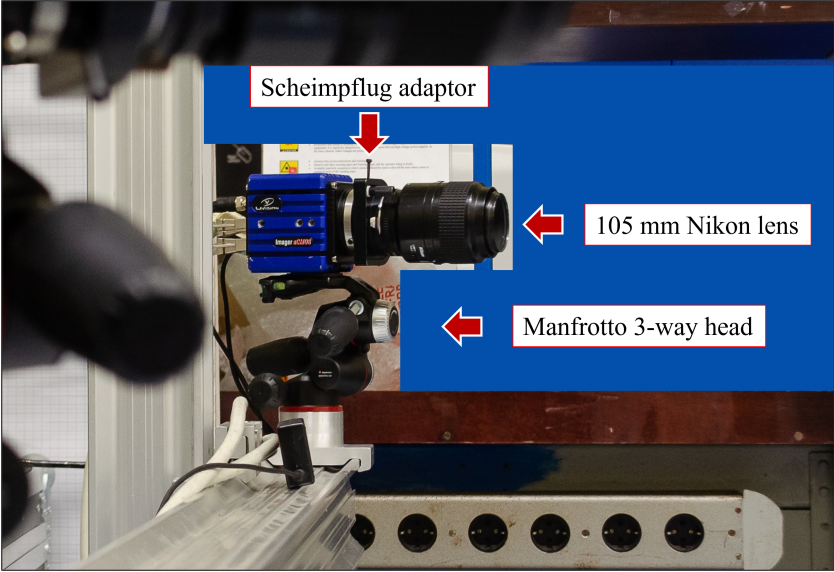


Figure 3.13: Camera equipment

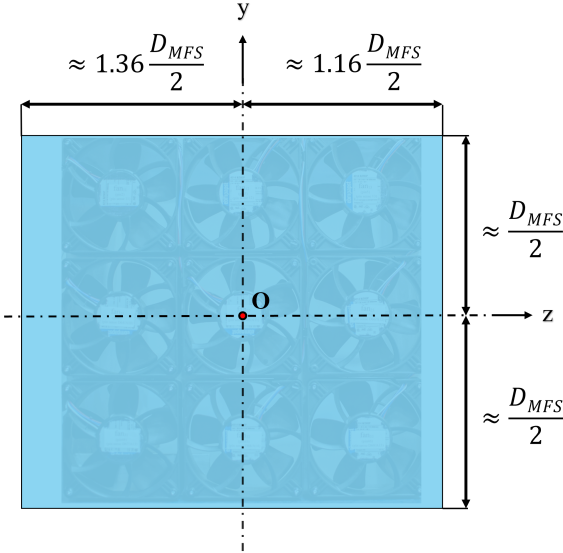


Table 3.6: Stereo PIV setup: camera parameters

Parameter	Value/Description
sCMOS sensor resolution	2560 x 2160 pixels
dewarped image resolution	2701 x 2174 pixels
pixel pitch	6.5 x 6.5 microns
digital image resolution	≈ 5.9 pixels/mm
angle between cameras	$\approx 41^\circ$

Figure 3.14: Stereo PIV setup: the FOV after the geometric calibration, scaled with respect to the symmetry axis of the system

3.3.4. Image acquisition parameters & Test matrix

For each flow case, the test matrix is presented. It includes the previously discussed information, such as the test cases and the measurement planes, and additionally, the image acquisition parameters, such as the time step between pulses and the number of samples acquired per recording. The time step between pulses was approximated with the in-plane optimization rule for planar PIV, and the out-of-plane optimization rule for stereo PIV. Preliminary measurements of the dynamic pressure at $2d_{fan}$ were conducted with a Pitot probe, from which the velocity was computed and used for this purpose (Appendix C).

Uniform flow

Duty Cycle [%]	10	20	30	40	50	60	70	80	90	100
$\Delta t_{\text{planar}} [\mu\text{s}]$	793	524	433	361	325	263	249	209	208	207
$\Delta t_{\text{stereo}} [\mu\text{s}]$	457	302	250	208	188	152	144	121	120	119
# Samples	100									
Measurement planes	SP1, SP2, SP3, CP1, CP2									

Table 3.7: Uniform flow test matrix showing the duty cycle values, the time step between pulses for the corresponding PIV method, the number of samples acquired and the measurement planes

Linear boundary layer

	Step 1 [%]	Step 2 [%]	Step 3 [%]	$\Delta t [\mu\text{s}]$	# Samples	Measurement planes
Baseline 1: 40%	± 2.5	± 5	± 10	361	100	SP1, SP2, SP3
Baseline 2: 70%	± 2.5	± 5	± 10	249	100	SP1, SP2, SP3

Table 3.8: Boundary layer test matrix showing the baseline cases and their corresponding steps, the time step between pulses for the corresponding PIV method, the number of samples acquired and the measurement planes

Gust

The acquisition frequency for recording the oscillating flow field should be done such that 10 ideally-equidistant phases are captured per cycle. In this case, since the maximum repetition rate of the laser is limited at 15 Hz, the highest operating frequency of the fans should be 1.5 Hz. However, we observed an abnormal communication between the triggers of the camera and the laser at sampling frequencies above 8 Hz, and thus set the acquisition frequency at this value, and limited the highest operating fan frequency at 0.8 Hz. As mentioned in Table 3.4, the chosen values are also found in literature. Moreover, we intend to capture 50 cycles, resulting in a total number of 500 samples.

Operating frequency [Hz]	Operating amplitude [%]	Mean operating amplitude [%]	$\Delta t_{\text{planar}} [\mu\text{s}]$	$\Delta t_{\text{stereo}} [\mu\text{s}]$	Measurement plane
0.2	50	10	325	-	SP2
0.4	60	20	263	-	
0.8	50	30	325	-	
0.2	10	50	325	-	SP3
0.4	20	60	263	-	
0.2	30	50	325	-	
0.2	50	10	-	188	CP2
	60	20	-	276	
	50	30	-	188	

Table 3.9: Gust test matrix showing the operating frequency, mean operating amplitude, operating amplitude, time steps, and measurement planes

The measurement campaign was conducted in the following order: all the test cases planned for SP1, then SP2, then SP3. After that, the stereo PIV layout was employed, and the measurements were conducted on CP1, then on CP2. After the data was acquired, it was processed to obtain the desired vector fields, used for analysis. This part is discussed in the next section.

3.4. Data processing & analysis tools

This section provides an overview of the data processing and analysis tools.

3.4.1. Data processing: DaVis 8

DaVis 8 has high-performance cross-correlation algorithms, thus it was chosen to process the image pairs and obtain the instantaneous fields. For the streamwise planes, a window size of 32 x 32 pixels was used, with an overlap of 75 %. The cross-planes were cross-correlated using a window size of 64 x 64 pixels, and 50 % overlap. The instantaneous fields were then time-averaged to obtain the mean field and the standard deviation.

The mean and instantaneous fields were exported for the uniform and gust cases. Only the mean fields were exported for the boundary layer cases.

3.4.2. Data analysis

The data analysis was conducted in Python. The three streamwise planes were stitched into a single one, using the overlapping region (Figure 3.7) as interpolated connections. There are a few references, notations and illustrations that should be introduced or reiterated to assure clarity in the next chapter: general references, applied to all the flow cases, but also particular ones, characteristic to the uniform flow in the cross-stream planes or to the gust analysis.

General spatial references and notations

Figure 3.15 shows the sketch of the stitched streamwise plane used to visualize the flow field on, with the x and y axis nondimensionalized by the D_{MFS} and d_{fan} , respectively. On the left, outside of the actual measurement plane, the lateral view of the MFS is illustrated, each fan being delimited by the thick black lines. The thin blue lines inside each fan represent the hub. At an offset of $0.14D_{MFS}$ to the right of the system, the measured domain starts. To talk about the development of the flow downstream, we refer to the flow regions as near field, middle field, and far field, as explained in subsection 3.3.1. Lastly, for scaling, a reference velocity is needed. The free stream, or inflow velocity is considered in most applications. In this case, since the flow is expected to be nearly uniform in the far field, we spatially average the mean streamwise velocity, \overline{U}_x , at the most downstream location, denote it by $U_{x, far\ field}$, and refer to it as the reference velocity henceforth. When needed, the mean velocity, mean vorticity and the root-mean-square of the velocity fluctuation fields are scaled by this reference velocity, at the mentioned duty cycle. The area chosen for averaging is represented by the dotted rectangular.

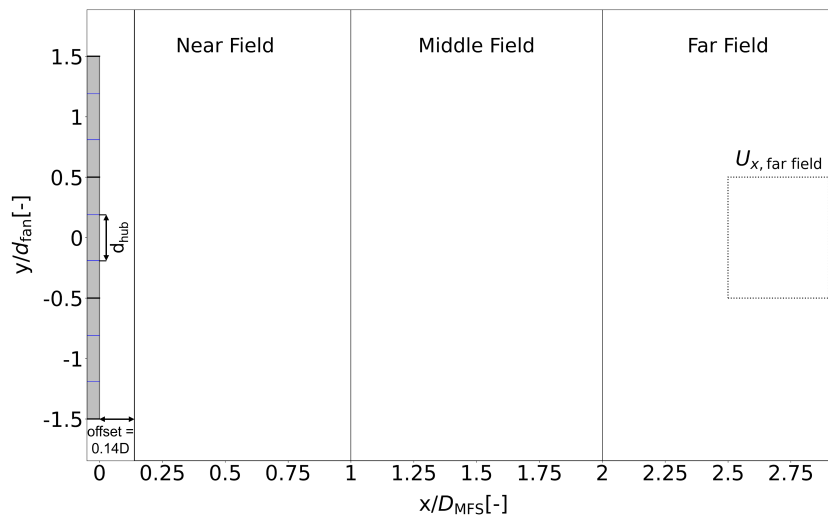


Figure 3.15: Illustration of the stitched streamwise plane containing details of spatial references and notations used throughout this chapter

Spatial references for gust analysis

The evaluation of the gust, both in time domain and frequency domain, is conducted using velocity signals spatially averaged over two areas downstream, at every time step. The areas are depicted as dotted rectangles in Figure 3.16. During the experiments, large recirculation bubbles were observed in the near field, and it was decided not to record measurements for the gust case in this plane.

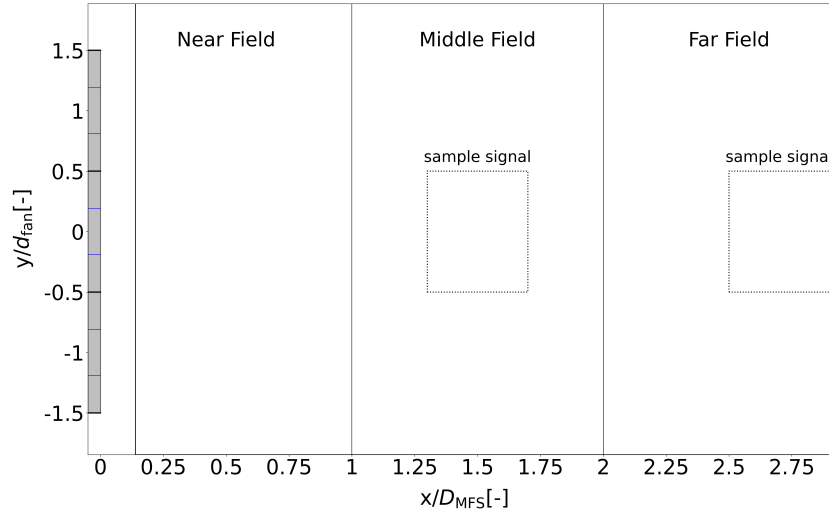


Figure 3.16: Illustration of the stitched streamwise plane containing details of spatial references used in the gust analysis.

The main results of the uniform and boundary layer flow use the vector fields from DaVis 8 for simple plotting of the variables. Moreover, there are three specific analysis measures that were implemented: turbulence intensity, spatial uniformity, and power spectral density (PSD).

Spatial Uniformity

We use the term *uniformity* to describe the level of spatial distribution of the local velocity across an area, relative to the spatially averaged velocity of that area. This can be translated as:

$$\text{uniformity [\%]} = \left(1 - \frac{\sigma}{U_x}\right) \cdot 100 \quad (3.2)$$

This index will be used in understanding the distribution of the streamwise velocity over the core of the cross planes, relative to the spatially averaged velocity at the core.

Turbulence Intensity

Turbulence intensity is a measure to describe the local standard deviation or root-mean-square (RMS) of the fluctuations, relative to the time-averaged velocity:

$$\text{Turbulence Intensity [\%]} = \frac{\sqrt{U_x'^2}}{\bar{U}_x} \cdot 100 \quad (3.3)$$

Another way to analyze the turbulent fluctuations is by normalizing the RMS by the reference velocity, $\frac{\sqrt{U_x'^2}}{U_{x, \text{far field}}}$.

Power Spectral Density

The Power Spectral Density (PSD) is a fundamental tool in signal processing used to analyze the distribution of power across different frequency components in a time series. It provides insight into the dominant frequencies present in a signal, making it particularly useful for identifying turbulence characteristics and oscillatory behavior in velocity measurements.

To compute the PSD in this study, Welch's method is employed ([43]), which enhances spectral estimation by dividing the signal into overlapping segments, applying a window function to reduce spectral leakage, and averaging the results. For the gust signal, a window size of 128 samples was used, with the default overlap of 50% and the default tapering function Hann.

4

Results

This chapter presents the characterization of the flow generated by the MFS. Respecting the order of objectives set in the beginning of the project, the results are revealed. The subject of the first section is the uniform flow, and it covers insights into both the vertical streamwise and the cross-sectional planes. Next, the second section focuses on the shear flow and the observations made for the two baseline cases. The third section provides the findings related to the streamwise sinusoidal gust. Each flow case has two subsections: the results, followed by a short discussion. Finally, the uncertainty of the measured data is discussed in the fourth section.

4.1. Uniform flow

The first research objective is focused on characterizing the flow generated by the MFS when the fans are operating at the same duty cycle. Since the system might represent an alternative solution to the wind tunnel in producing uniform inflow, we are interested in learning about the flow in the far field, and its development up to that region. These findings are addressed in this section.

First, the results in the streamwise plane are interpreted. They highlight the mean streamwise velocity achieved at the most downstream region, the visualization of the mean streamwise velocity field and its fluctuations, and the profiles of turbulence intensity at different locations downstream. Then, the focus shifts on the cross-stream planes, covering the vorticity and streamwise (out-of-plane) velocity fields, and the turbulence intensity and uniformity achieved at the core of the field. The section ends with a discussion including a comparison with another fan array generator, and potential improvements of the flow quality.

4.1.1. Vertical streamwise plane

This subsection covers the following results: the velocity achieved in the far field region, the visualization of the mean streamwise velocity field and its fluctuations, and the profiles of turbulence intensity at different locations downstream.

Far field streamwise reference velocity

In aerodynamic experiments, the free stream velocity of a wind tunnel is a crucial scaling parameter that defines the inflow conditions. Since the MFS is a flow generator itself that might be used in future experiments, we want to know the inflow velocity it can provide at different duty cycles. As explained in Figure 3.15, this is chosen to be $U_{x, \text{far field}}$. Figure 4.1 shows the resulting reference velocity per duty cycle and the corresponding rotational speed.

The mean streamwise velocity in the far field region increases approximately linear with the duty cycle up to 80 %, then it remains nearly constant. This trend matches the evolution of the fan's rotational speed with respect to the duty cycle, a sign that the convective velocity increases almost linearly with the RPM. The relative increase in velocity from one duty cycle to another decreases from 12%, between 10% and 20% to 5%, between 70% and 80%. At maximum performance, between 80% and 100% duty cycle, the reference velocity is around 6.2 m/s.

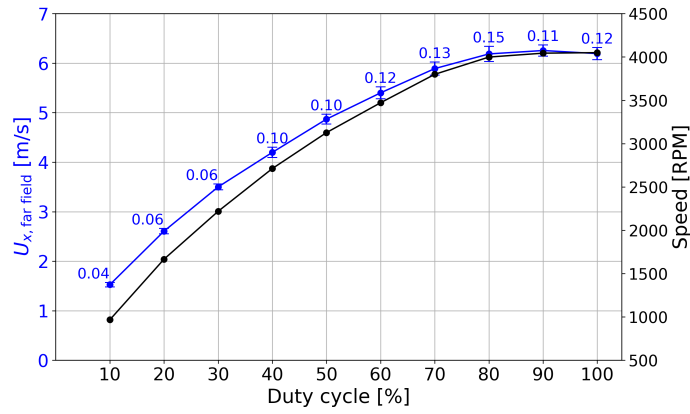


Figure 4.1: Line graph representation of Duty Cycle [%] VS $\bar{U}_{x, far field}$ [m/s] and fan speed [RPM]. The spatial standard deviation corresponding to each spatially averaged velocity is displayed on top of each data point.

Mean streamwise velocity field

In Figure 4.2 we visualize the mean streamwise velocity field, normalized by $U_{x, far field}$, at 50% and 100% duty cycle. The vertical mean streamwise velocity profiles are plotted at several locations.

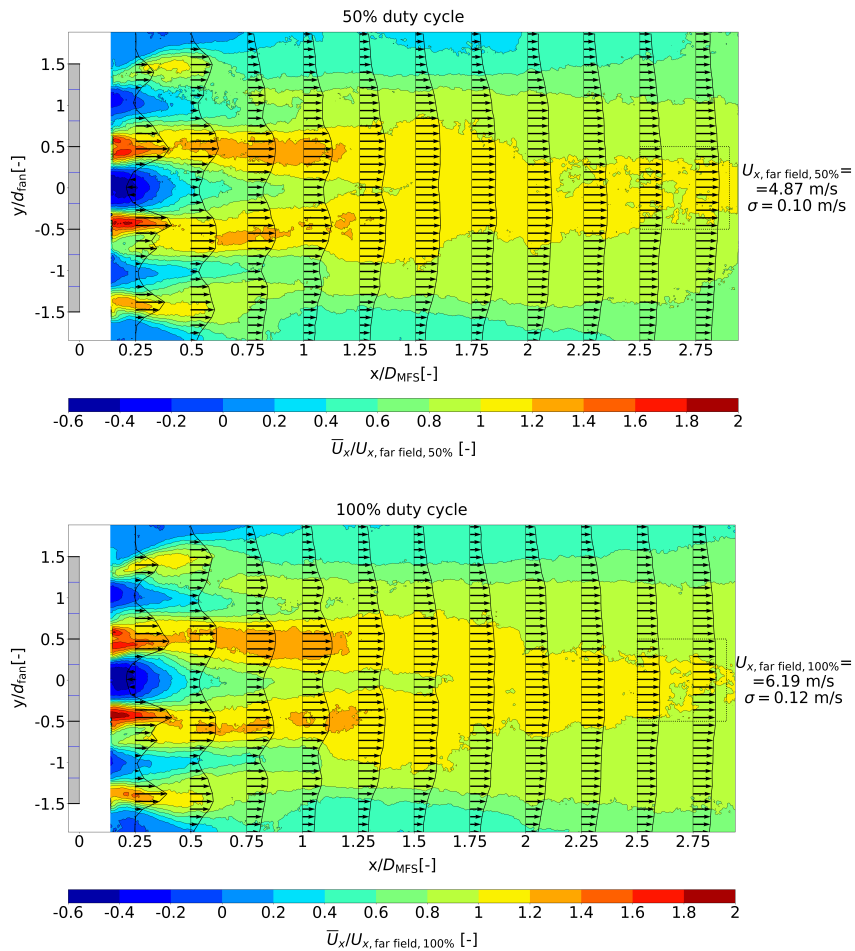


Figure 4.2: Vertical streamwise plane colored by the normalized mean streamwise velocity field. The normalized streamwise velocity vectors are displayed at different locations downstream. The dotted square represents the area over which the reference velocity was averaged. Cases presented: 50% and 100% duty cycle. For $U_{x, far field, 50\%} = 4.87$ m/s, the spatial standard deviation is $\sigma = 0.10$ m/s. For $U_{x, far field, 100\%} = 6.19$ m/s, the spatial standard deviation is $\sigma = 0.12$ m/s.

Both cases present similar characteristics. The near field is dominated by a complex vertical velocity gradient, comprising two alternating phenomena: flow mixing at the fans blades, and recirculation bubbles at the hubs. These steep gradients represents shear layers within the field, which transfer momentum from high to low velocities and cause turbulence mixing. At the edge of the lower and upper fans, corresponding lower and upper shear layers appear to develop and expand downstream (although not fully captured in this field of view), stretching over almost $2/3$ of the vertical streamwise field. The expansion of the shear layer and the high-speed flow mixing in the interacting region between the fans were also reported by [33] and referred to as characteristics similar to small subsonic jets. In the middle field, the vertical velocity gradient tends to stabilize in the range of $y/d_{\text{fan}} = -1$ to $y/d_{\text{fan}} = 1$, while the outer regions are still ruled by the edge shear layers. In the far field, the vertical velocity profile becomes nearly flat over a height almost equal to the height of one fan, at the middle of the field. Here, the deviation from $U_{x, \text{far field}}$ is less than 20%. This area should be called the *core* of the flow hereafter.

In the near field there are three recirculation bubbles which start right at the hub (not shown, due to the offset of the first measurement plane). It is safe to assume they have the same initial diameter, that is the size of the hub, d_{hub} . The fan in the middle exhibits a backflow region whose diameter consistently stretches across a downstream distance of almost $2.5d_{\text{hub}}$. It seems to be preserved by the highly mixed flow between the fans that reach velocities of almost $2U_{x, \text{far field}}$. Meanwhile, the recirculation of the edge fans seems to fade out quicker, both in terms of diameter and length, due to momentum loss in the flow generated by the outer half of the fans.

Root-mean-square of the streamwise velocity fluctuations

Figure 4.3 illustrates the root-mean-square of the streamwise velocity fluctuations field with respect to the reference velocity. The 50% and 100% duty cycle cases are compared.

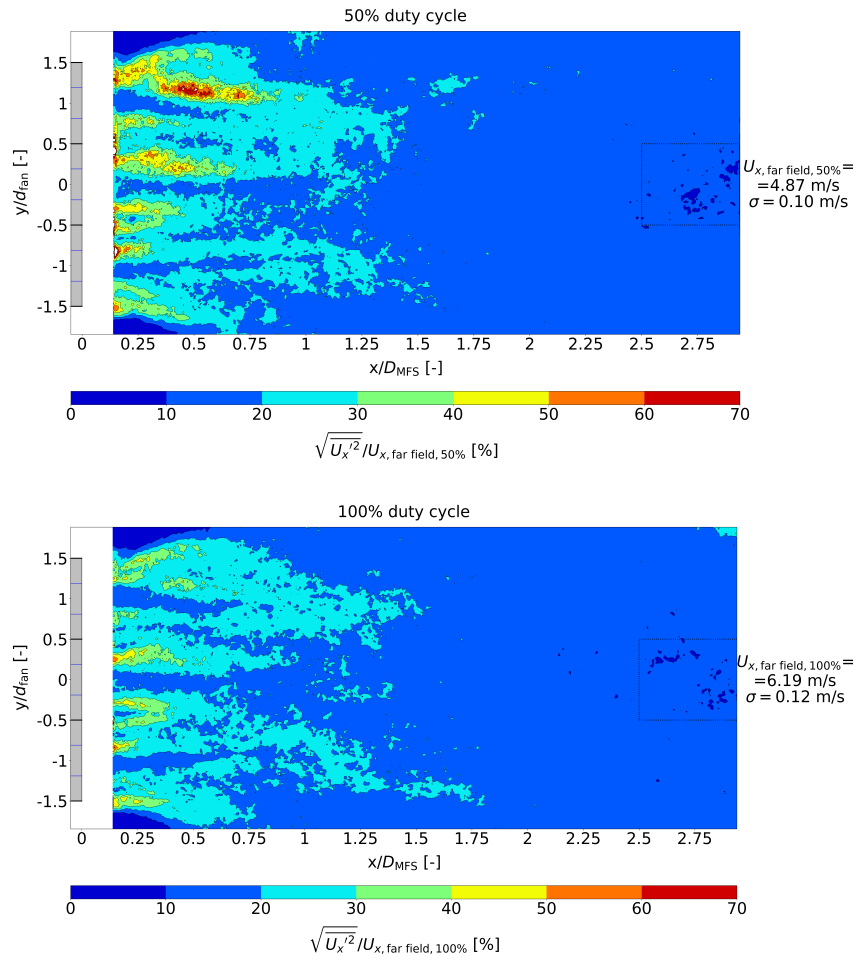


Figure 4.3: Vertical streamwise plane colored by the RMS of the streamwise velocity fluctuations, with respect to the reference velocity, $U_{x, \text{far field}}$. The dimensional $U_{x, \text{far field}}$ is also displayed. The normalized streamwise velocity fluctuation vectors are displayed at different locations downstream. The dotted square represents the area over which the reference velocity was averaged. Cases presented: 50% and 100% duty cycle. For $U_{x, \text{far field}, 50\%} = 4.87$ m/s, the spatial standard deviation is $\sigma = 0.10$ m/s. For $U_{x, \text{far field}, 100\%} = 6.19$ m/s, the spatial standard deviation is $\sigma = 0.12$ m/s.

The highest fluctuations, 30% to 40% of the $U_{x, \text{far field}}$, are in the near field, where strong mixing takes place at the level of the blades. Low fluctuations are encountered at the hub levels, where the flow field smoothly increases from near-0 or negative flow. Because shear layers are formed at the interface between the recirculation region and the small jets, turbulence mixing occurs. The mixing lasts up to and including the middle field. After that, the fluctuations diminish below 20% of the $U_{x, \text{far field}}$.

Turbulence intensity

Comparing the spread of the fluctuations relative to the local mean streamwise velocity, the turbulence intensity profiles are presented in Figure 4.4 for all duty cycle cases at several locations downstream. The vertical red line represents the turbulence intensity of 10%.

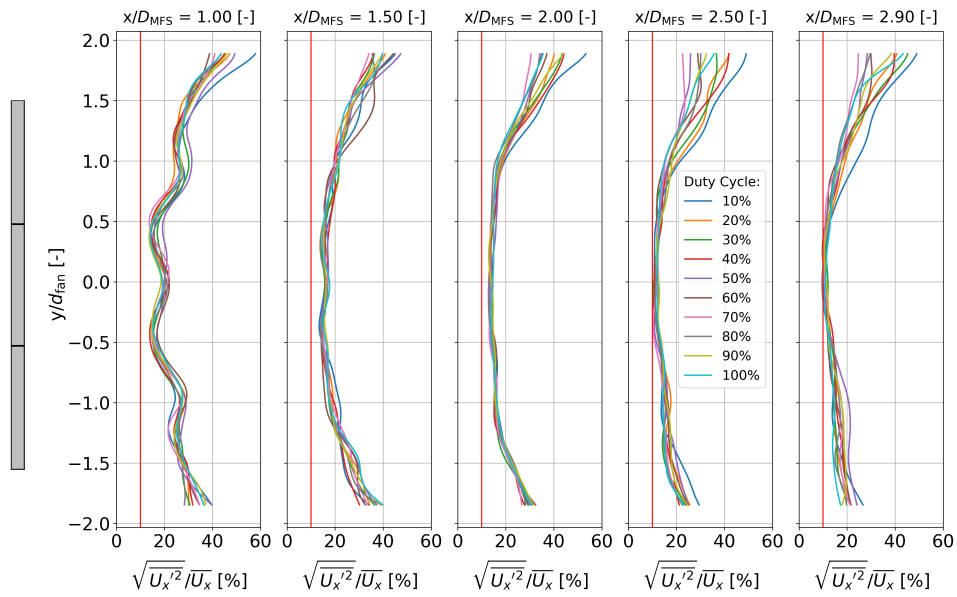


Figure 4.4: Turbulence intensity profiles at different locations downstream. Comparison between all the uniform modes. The vertical red line marks the 10% turbulence intensity

The local turbulence intensities across all the cases present the same evolution downstream. The vertical profile fluctuates around 20% at $x = D_{MFS}$, part of the region where turbulence mixing occurs. Then, it slowly evens out and reaches values of about 10% starting from $x = 2.5D_{MFS}$, mostly at the core of the flow. [33] obtained downstream turbulence intensity around the same value during the aerodynamic characterization of their multi-fan system.

4.1.2. Cross-stream planes

This section covers the following results: the mean streamwise velocity, the mean vorticity, and the turbulence intensity at the two cross-planes for 50% and 100% duty cycles; the turbulence intensity spatially averaged at the core of the flow across the operational duty cycle range; the uniformity of the flow computed at the core of the flow across the operational duty cycle range.

Mean streamwise velocity field

Figure 4.5 displays a comparison between the mean streamwise velocity fields generated at 50% and 100% duty cycle, with overlapped in-plane velocity vectors. As expected, the two fields present similar characteristics.

The CP1 plane shows the complex dynamics of the streamwise flow, where the inner and edge shear layers and the wakes induced by the rotation of the fans contribute to momentum transfer and turbulence mixing within the field. Progressing downstream, to CP2, the entire field is subjected to rotation. Moreover, the outer shear layer stretches and distorts over the plane, becoming asymmetric, characteristics also reported by [33]. The core stretches over the area of a fan, meaning $1/9$ of the system's area, and the mean velocity seems to be evenly distributed due to flow diffusion.

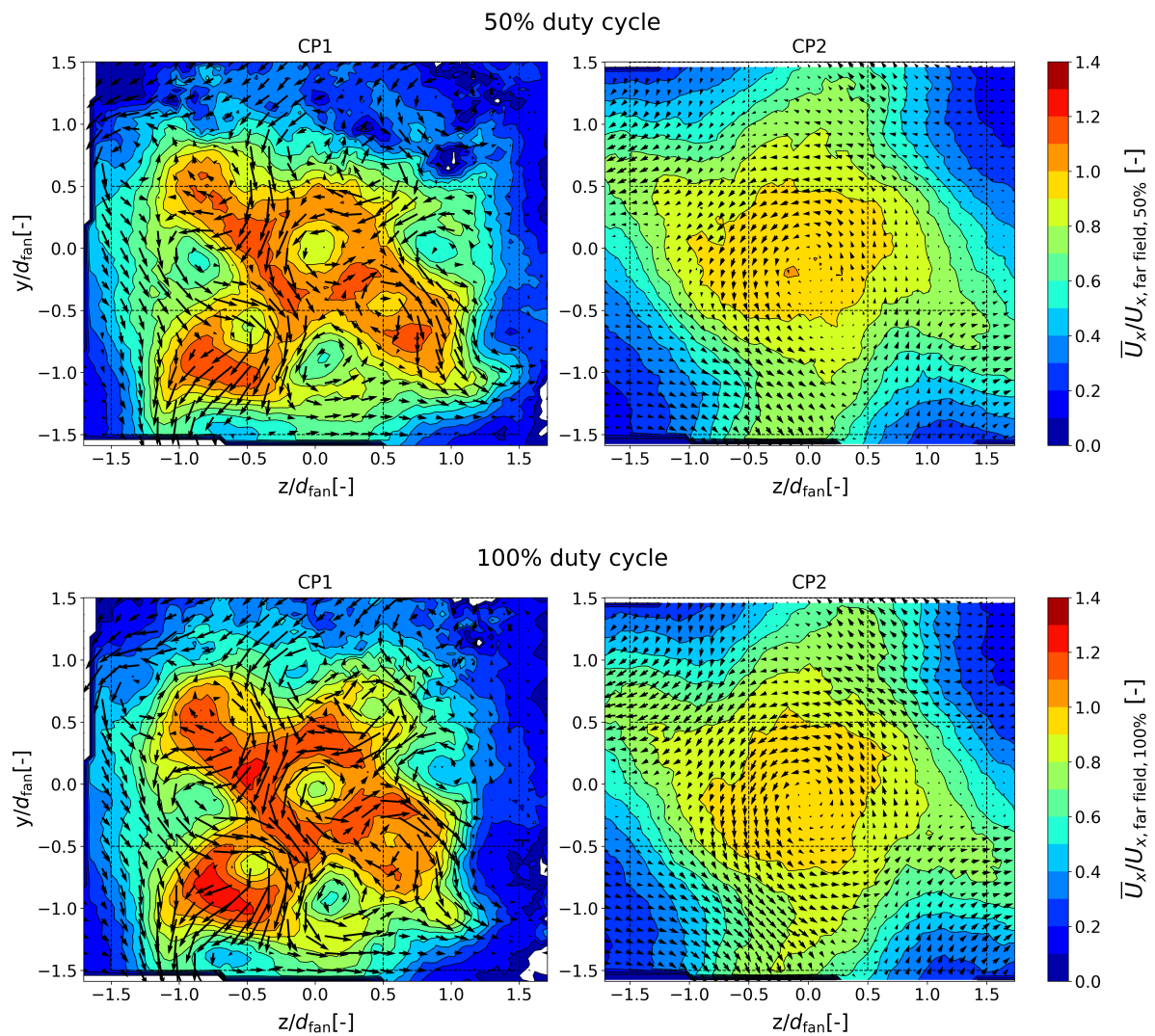


Figure 4.5: Cross-stream planes colored by the mean streamwise velocity normalized by the reference velocity, $\bar{U}_{x, \text{far field}}$. The in-plane velocity vectors (scaled down by a factor of 10) are overlapped. On the left: the cross-stream plane at distance D_{MFS} downstream. On the right: the cross-stream plane at distance $2.5D_{\text{MFS}}$ downstream from the MFS.

Mean vorticity field

Similar to the mean velocity field, Figure D.5 displays a comparison between the mean vorticity fields generated at 50% and 100% duty cycle, with overlapped velocity vectors. The vorticity fields at 50% and 100% duty cycles in CP1 reveal a complex interaction between multiple wakes, where each induces velocity on its neighbors, creating a dynamic and interconnected flow structure. The wakes, or swirling flow, observed at the hub level seem to act as counter-clockwise sources, while secondary wakes form at the gaps between each four neighboring hubs, and act as clockwise sinks. At 100% duty cycle, the normalized vorticity field is more intense than at 50%, likely due to a more aggressive increase of the tangential components with the rotational speed of the fans, compared to the nearly linear variation of the convective component relative to the rotational speed. At the second plane, CP2, the concentrated vorticity diffuses across the plane, merging into a main counter-clockwise swirl of weak intensity in the middle, and four clockwise-rotating ones at the corners.

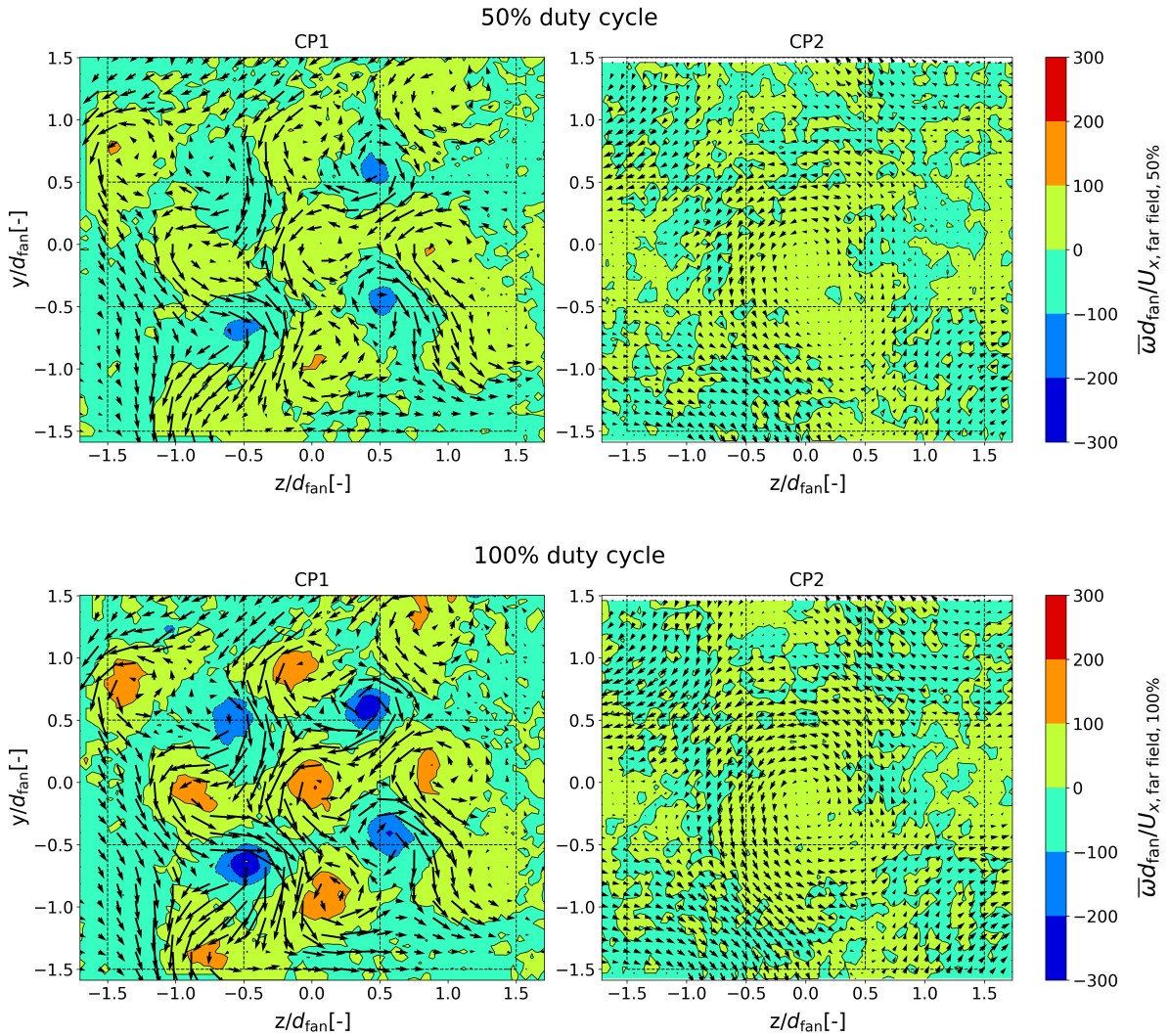


Figure 4.6: Cross-stream planes colored by the mean vorticity normalized by the reference velocity, $\bar{U}_{x, \text{far field}}$, and the fan diameter, d_{fan} . The in-plane velocity vectors (scaled down by a factor of 10) are overlapped. On the left: the cross-stream plane at distance D_{MFS} downstream. On the right: the cross-stream plane at distance $2.5D_{\text{MFS}}$ downstream from the MFS.

Turbulence intensity

The turbulence intensity is presented first as a contour plot comparison between the 50% duty cycle and 100% duty cycle, and then as averaged turbulence intensity at the core of the field across the operating range of duty cycles.

In figure Figure 4.7, the turbulence intensity field is stretched and distorted, as expected, since the resulting mean field displayed the same characteristics. The core presents values primarily in between 10 % and 14%, pointed out by Figure 4.8. The mean values of turbulent intensity fluctuate around 11.5%, with the highest spread relative to its mean at 90% duty cycle, with 15.3% variation from the turbulence intensity mean. It is expected, since the highest standard deviation of the fluctuations was reported for the same duty cycle in Figure 4.1.

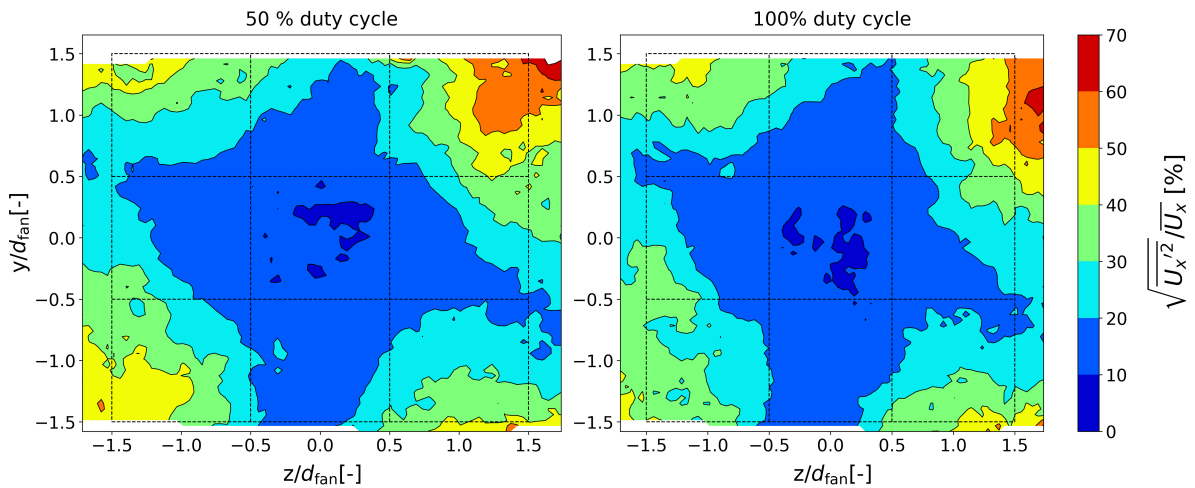


Figure 4.7: CP2 plane colored by turbulence intensity for the 50% and 100% duty cycle cases.

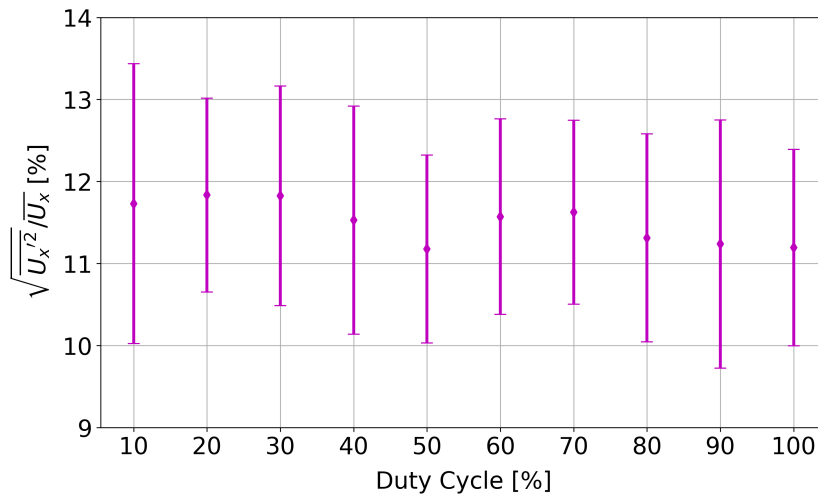


Figure 4.8: Duty cycle VS Turbulence intensity spatially averaged at the core of CP2.

Flow uniformity

We are interested in investigating the influence of duty cycle on the spread of the values across the core, relative to the spatially averaged mean, by plotting the uniformity against the corresponding duty cycles at CP2.

The core of the flow, where the streamwise velocity and turbulence intensity appear to stabilize, unaffected by the edge shear layers and preserved at the middle of the system, is considered to have the size of a fan. The extended core is an arbitrarily enlarged region from the core, included in the analysis to underline the effect of the outer shear layer. Both regions are shown in Figure 4.9.

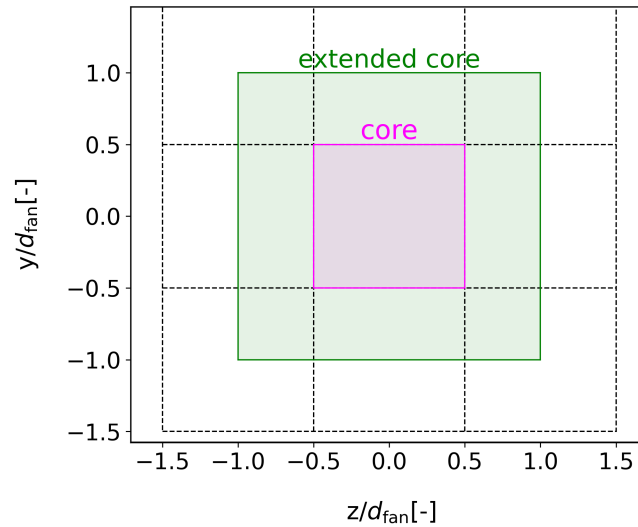


Figure 4.9: Illustration of an arbitrary cross-plane and the two regions of interest: the core, assumed to be equal with the area of a fan, and the extended core.

The plot reveals that for uniform flow generation, the uniformity is independent of the duty cycle of the fans. The core is characterized by a relatively high uniformity, of 96%, meaning that most of the data is found within 4% of the spatially averaged value. As expected, the uniformity at the extended core is reduced due to the influence of the edge shear layer, fluctuating around 86%.

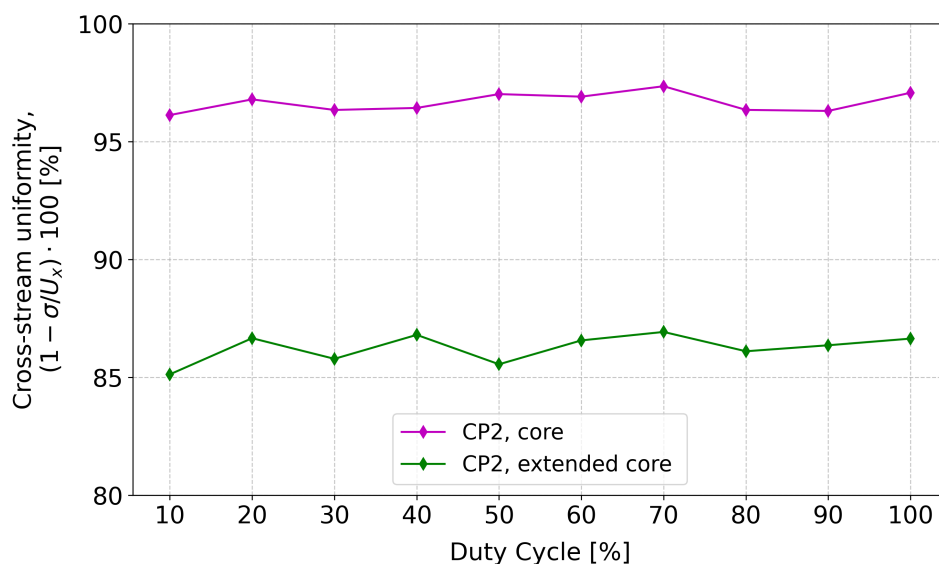


Figure 4.10: Uniformity across the core (purple line) and extended core (green line), at CP1 (x marks) and CP2 (diamond marks), for the entire operating range of duty cycles.

4.1.3. Discussion

The characterization of the flow generated by the MFS operating in uniform mode was conducted in both vertical streamwise and cross-planes.

The core of the flow in the far field, equal to the area of a fan or $1/9$ of the area of the system, is characterized by cross-sectional uniformity of 96% (4% variation from average) and turbulence intensity around 11.5% across all duty cycles. [33] revealed similar values of turbulence intensity at the core of the flow. Low-speed wind tunnels are known to generate uniform, steady flow of 0.2-0.3% spatial variation from average, and turbulence intensity below 0.2% [9]. However, in wind energy aerodynamic applications, this is usually a desired value for the simulated turbulence intensity [20], reflecting the ABL unsteady wind conditions experienced by a wind turbine.

In the current configuration, the core in the far field is too small to fully cover a possible test model, such as a mesh dish or a finite-span wing. Therefore, it needs to be extended to a higher $N_{\text{row}} \times N_{\text{columns}}$ configuration, where N is the number of fans per row and column. In this way, the core would increase to an area of $(N_{\text{row}} - 2)(N_{\text{column}} - 2) \cdot (d_{\text{fan}})^2$, while also accounting for the development of the edge shear layer at the edge fans. For example, in the case of a 9×9 system, the core area would increase by a factor of 49 compared to a single unit of 3×3 fans. Of course, this should be validated by conducting a measurement campaign and investigating further the shear layer and how it affects the extended core.

Besides the flow characteristics downstream of the system, the following flow properties in the near field were observed. Recirculation bubbles of nearly $2.5d_{\text{hub}}$ and small jets with speeds of twice the value of the reference velocity are developing. Because of the steep velocity gradient formed at the interface between the two, momentum transfer occurs which causes turbulence mixing. In turn, this regenerates the flow downstream of the hub. If the recirculation would be reduced to 0 by adding a matching shape (e.g. ellipsoid), the flow, hypothetically attached to this shape, might maintain its higher speed right downstream of the shape, where momentum recovery would have originally begun.

Additionally, the cross-stream planes revealed strong swirls created by the rotation of the fans, defining the flow structures as highly complex and mutually-influencing. It was shown that the tangential components are still relevant in the second plane, by showing the in-plane velocity vectors, scaled down by a factor of 10. Reducing the swirling and the turbulence mixing would decrease the turbulence intensity and would ensure the streamwise component dominates the field, although it might come at the cost of losing momentum. To investigate this, a honeycomb mesh could be placed downstream of the system.

4.2. Linear shear flow

This section aims to assess whether the MFS could generate linear shear flow profiles modeled by six arbitrarily chosen linear variations of duty cycles. For each of the two baseline cases and their corresponding three variations, the vertical profiles are compared. The locations are chosen to be in the far field, between $2.5D_{MFS}$ and $2.9D_{MFS}$, because the turbulence mixing is absent at the core. In addition, an informative table is provided with the expected reference velocities for each duty cycle of the given boundary layer mode. The corresponding velocity of each duty cycle presented in this section is interpolated from Figure 4.1.

4.2.1. Baseline 1: 40 % duty cycle

The streamwise velocity profiles of the three boundary layer cases shaped around the baseline 1 duty cycle are illustrated in Figure 4.11 (with $\pm 2.5\%$ increment), in Figure 4.12 (with $\pm 5\%$ increment), and in Figure 4.13 (with $\pm 10\%$ increment). For each case, the expected reference velocities and their relation to the known baseline 1 reference velocity $U_{x, \text{far field}, 40\%}$ are provided in Table 4.1 (with $\pm 2.5\%$ increment), in Table 4.2 (with $\pm 5\%$ increment), and in Table 4.3 (with $\pm 10\%$ increment).

Overall, linear shear layer profiles could not be obtained, being impeded by the development of the outer shear layer. Regardless of the shear layer mode, the expected streamwise velocities are not reached at the level of the top and bottom rows. The profiles are relatively similar with the uniform cases, presenting the highest velocity at the core, and decreasing toward the edges due to the presence of the outer shear layer. Nevertheless, these cases provide valuable insights, as the flow response becomes more pronounced with larger step changes, particularly at $\pm 5\%$ and $\pm 10\%$. Although dampened out by the shear layer, the upper edge flow still shows clear efforts to reach the expected velocity. In the upper half of the bottom region, from $y/d_{MFS} = -1$ to $y/d_{MFS} = -0.5$, the flow slowed by the bottom row duty cycle condition appears to interact with the faster flow of the core, forming a more steep velocity gradient, especially at $x/D_{MFS} = 2.9$. Again, this is more noticeable for the cases of -5% and -10% duty cycle steps (Figure 4.12, Figure 4.13).

Baseline 1: 40% duty cycle; case 1: $\pm 2.5\%$ duty cycle variation

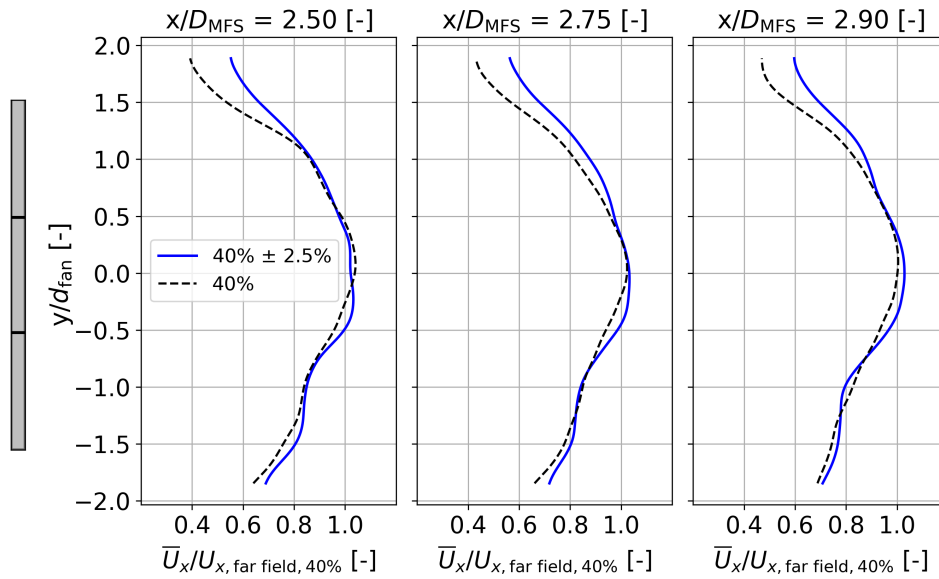


Figure 4.11: Vertical profiles of the streamwise velocity at different locations in the far field. Comparison between the uniform flow case generated at 40% duty cycle and the baseline 1 case 1 variations: 37.5% (bottom row), 40% (middle row), 42.5% (top row)

Fan location	Duty Cycle [%]	$U_{x,\text{far field, duty cycle}}$ [m/s]	$\frac{U_{x,\text{far field, duty cycle}}}{U_{x,\text{far field, 40\%}}}$ [-]	$\frac{U_{x,\text{far field, duty cycle}} - U_{x,\text{far field, 40\%}}}{U_{x,\text{far field, 40\%}}} \times 100$ [%]
Top row	42.5	4.36	1.04	+ 4
Middle row	40	4.20	1.00	0.00
Bottom row	37.5	4.00	0.95	- 4.15

Table 4.1: Baseline 1, case 1: duty cycle variations (first column), expected streamwise velocity (dimensional, second column), expected streamwise velocity (normalized, third column), expected relative variation from the baseline 1 reference velocity (fourth column)

Baseline 1: 40% duty cycle; case 2: $\pm 5\%$ duty cycle variation

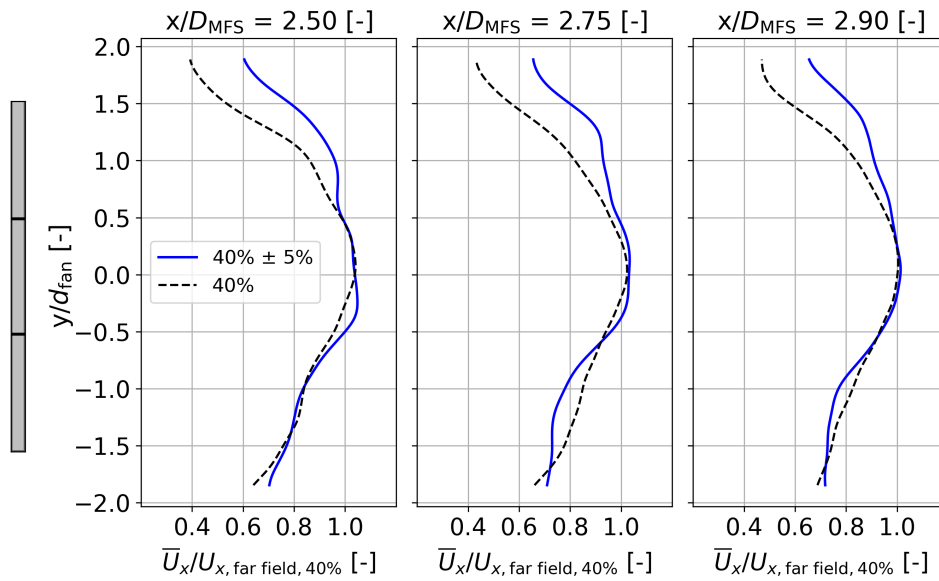


Figure 4.12: Vertical profiles of the streamwise velocity at different locations in the far field. Comparison between the uniform flow generated at 40% duty cycle and the baseline 1 case 2 variations: 35% (bottom row), 40% (middle row), 45% (top row)

Fan location	Duty Cycle [%]	$U_{x,\text{far field, duty cycle}}$ [m/s]	$\frac{U_{x,\text{far field, duty cycle}}}{U_{x,\text{far field, 40\%}}}$ [-]	$\frac{U_{x,\text{far field, duty cycle}} - U_{x,\text{far field, 40\%}}}{U_{x,\text{far field, 40\%}}} \times 100$ [%]
Top row	45	4.53	1.08	+ 8
Middle row	40	4.20	1.00	0.00
Bottom row	35	3.85	0.91	- 8.3

Table 4.2: Baseline 1, case 2: duty cycle variations (first column), expected streamwise velocity (dimensional, second column), expected streamwise velocity (normalized, third column), expected relative variation from the baseline 1 reference velocity (fourth column)

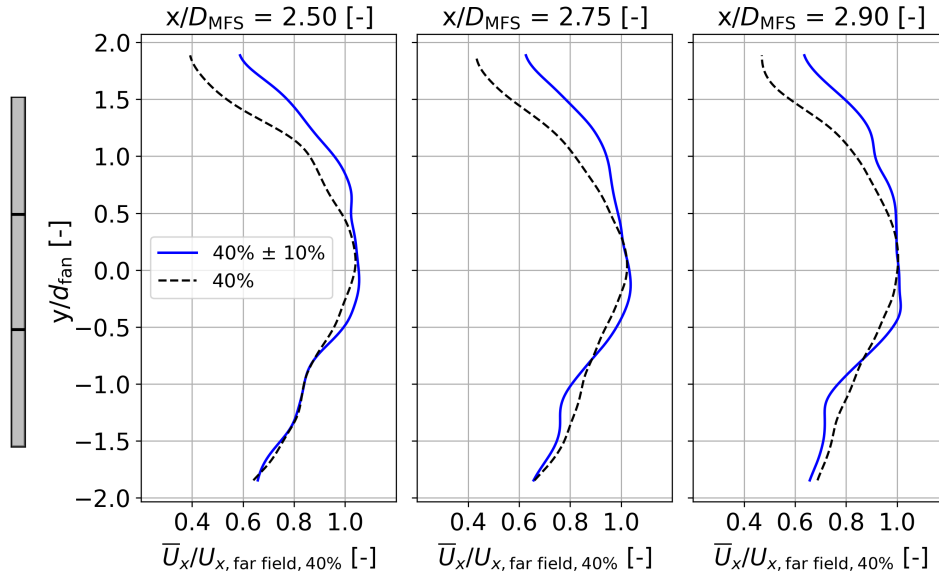
Baseline 1: 40% duty cycle; case 3: $\pm 10\%$ duty cycle variation

Figure 4.13: Vertical profiles of the streamwise velocity at different locations in the far field. Comparison between the uniform flow generated at 40% duty cycle and the baseline 1 case 3 variations: 30% (bottom row), 40% (middle row), 50% (top row)

Fan location	Duty Cycle [%]	$U_{x, \text{far field, duty cycle}}$ [m/s]	$\frac{U_{x, \text{far field, duty cycle}}}{U_{x, \text{far field, 40\%}}}$ [-]	$\frac{U_{x, \text{far field, duty cycle}} - U_{x, \text{far field, 40\%}}}{U_{x, \text{far field, 40\%}}} \times 100$ [%]
Top row	50	4.87	1.16	+ 16
Middle row	40	4.20	1.00	0.00
Bottom row	30	3.5	0.83	- 16.61

Table 4.3: Baseline 1, case 3: duty cycle variations (first column), expected streamwise velocity (dimensional, second column), expected streamwise velocity (normalized, third column), expected relative variation from the baseline 1 reference velocity (fourth column)

4.2.2. Baseline 2: 70 % duty cycle

Similarly, the streamwise velocity profiles formed by the three boundary layer modes shaped around the baseline 2 duty cycle are illustrated in Figure 4.14 (with $\pm 2.5\%$ increment), in Figure 4.15 (with $\pm 5\%$ increment), and in Figure 4.16 (with $\pm 10\%$ increment). For each case, the expected reference velocities and their relation to the baseline 1 reference velocity $U_{x, \text{far field, 70\%}}$ are provided in Table 4.4 (with $\pm 2.5\%$ increment), in Table 4.5 (with $\pm 5\%$ increment), and in Table 4.6 (with $\pm 10\%$ increment).

In the case of baseline 2, the flow response is less pronounced. The low relative difference of the expected reference velocity at the top and bottom fans is even more diminished by the influence of the shear layer, causing the flow to remain nearly unchanged throughout the duty cycle variations. The only observable behavioral change of the flow is for the increment of -10% , in Figure 4.16.

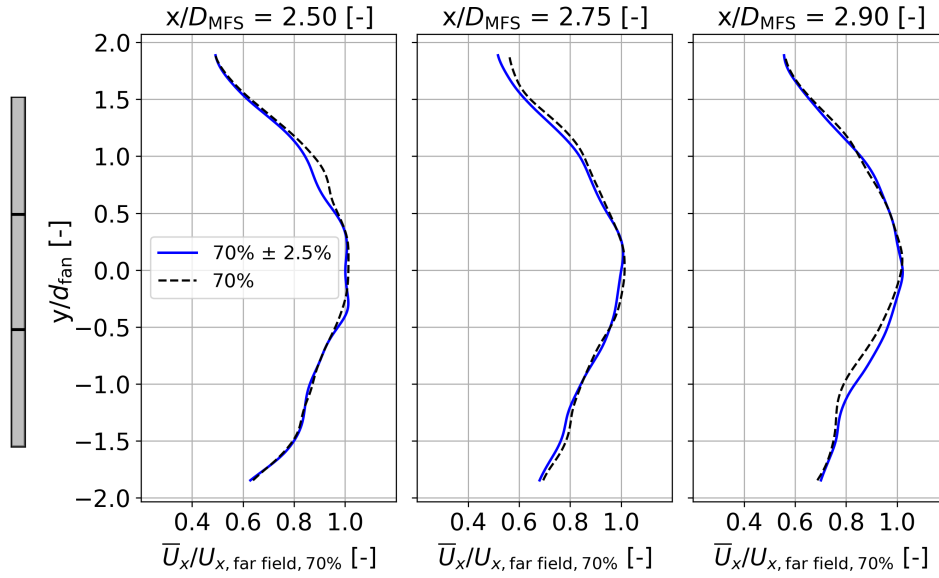
Baseline 2: 70% duty cycle; case 1: $\pm 2.5\%$ duty cycle variation

Figure 4.14: Vertical profiles of the streamwise velocity at different locations in the far field. Comparison between the uniform flow case generated at 70% duty cycle and the baseline 2 case 1 variations: 67.5% (bottom row), 70% (middle row), 72.5% (top row).

Fan location	Duty Cycle [%]	$U_{x, \text{far field, duty cycle}}$ [m/s]	$\frac{U_{x, \text{far field, duty cycle}}}{U_{x, \text{far field, 70\%}}}$ [-]	$\frac{U_{x, \text{far field, duty cycle}} - U_{x, \text{far field, 70\%}}}{U_{x, \text{far field, 70\%}}} \times 100$ [%]
Top row	72.5	6	1.01	+ 1.25
Middle row	70	5.89	1.00	0.00
Bottom row	67.5	5.76	0.97	- 2

Table 4.4: Baseline 2, case 1: duty cycle variations (first column), expected streamwise velocity (dimensional, second column), expected streamwise velocity (normalized, third column), expected relative variation from the baseline 1 reference velocity (fourth column)

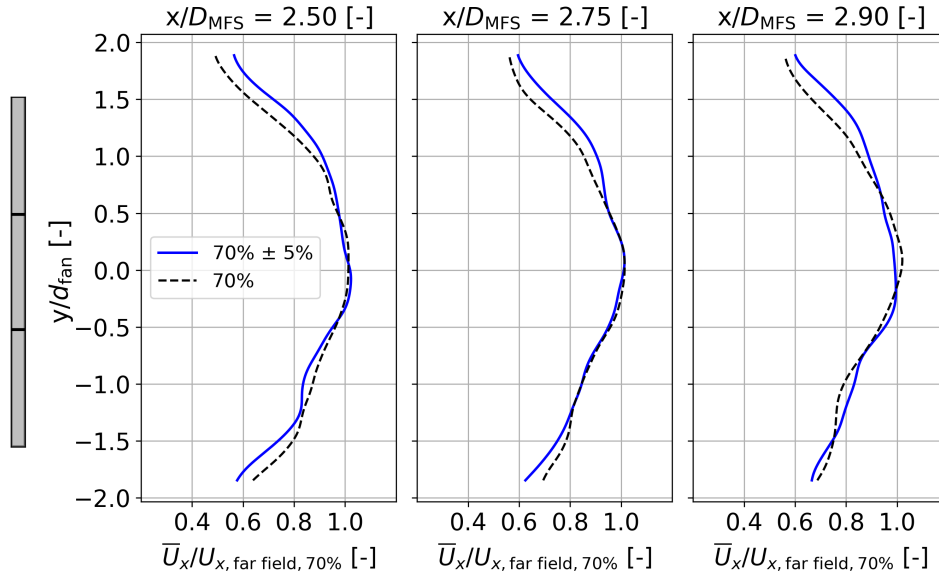
Baseline 2: 70% duty cycle; case 2: $\pm 5\%$ duty cycle variation

Figure 4.15: Vertical profiles of the streamwise velocity at different locations in the far field. Comparison between the uniform flow case generated at 70% duty cycle and the baseline 2 case 2 variations: 65% (bottom row), 70% (middle row), 75% (top row)

Fan location	Duty Cycle [%]	$U_{x, \text{far field, duty cycle}}$ [m/s]	$\frac{U_{x, \text{far field, duty cycle}}}{U_{x, \text{far field, 70\%}}}$ [-]	$\frac{U_{x, \text{far field, duty cycle}} - U_{x, \text{far field, 70\%}}}{U_{x, \text{far field, 70\%}}} \times 100$ [%]
Top row	75	6.03	1.02	+ 2.51
Middle row	70	5.89	1.00	0.00
Bottom row	65	5.64	0.95	- 4.15

Table 4.5: Baseline 2, case 2: duty cycle variations (first column), expected streamwise velocity (dimensional, second column), expected streamwise velocity (normalized, third column), expected relative variation from the baseline 1 reference velocity (fourth column)

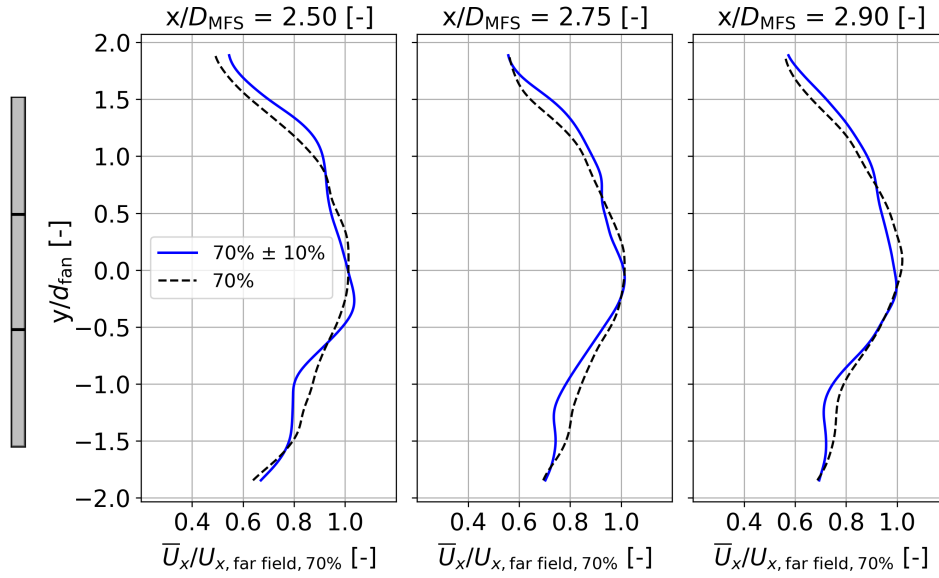
Baseline 2: 70% duty cycle; case 3: $\pm 10\%$ duty cycle variation

Figure 4.16: Vertical profiles of the streamwise velocity at different locations in the far field. Comparison between the uniform flow case generated at 70% duty cycle and the baseline 2 case 1 variations: 60% (bottom row), 70% (middle row), 80% (top row)

Fan location	Duty Cycle [%]	$U_{x, \text{far field, duty cycle}}$ [m/s]	$\frac{U_{x, \text{far field, duty cycle}}}{U_{x, \text{far field, 70\%}}}$ [-]	$\frac{U_{x, \text{far field, duty cycle}} - U_{x, \text{far field, 70\%}}}{U_{x, \text{far field, 70\%}}} \times 100$ [%]
Top row	80	6.1	1.05	+ 5
Middle row	70	5.89	1.00	0.00
Bottom row	60	5.4	0.91	- 8

Table 4.6: Baseline 2, case 3: duty cycle variations (first column), expected streamwise velocity (dimensional, second column), expected streamwise velocity (normalized, third column), expected relative variation from the baseline 1 reference velocity (fourth column)

4.2.3. Discussion

The generation of linear boundary layer profiles for each presented case is difficult to obtain with this configuration of fans. This is because two thirds of the velocity field in the vertical streamwise plane are dominated by the edge shear layers, impeding the flow in these regions to achieve the expected velocity. Therefore, a suggestion would be to add at least one unit along the height. Extending the configuration, and consequently, the core, might allow the flow to develop according to the predefined profile, while also taking into account the contribution of the shear layers. Considering the size of the core equals the size of one fan, adding extra rows extends the area of the core to $(N_{\text{row}} - 2)(N_{\text{column}} - 2) \cdot (d_{\text{fan}})^2$. The validation of this setup should be investigated.

Concurrently, a profiling strategy should be adapted. [17] reported on the discrepancy between the generated and the prescribed profiles given as input to the fans of an open test facility, due to the visible influence of the edge shear layers. [28] revealed as well the lack of correlation between the predefined ABL profile and the resulted one, in the characterization of the multi-jet system. As a solution, the fans or jets were adjusted until they fit the desired profile. For this project, the boundary layer modes were arbitrarily chosen and tested without previous knowledge of the flow characteristics specific to this multi-fan system. Now that the flow behavior and the reference streamwise velocities are known (Figure 4.1), a desirable future work could include the development of a code that predefines the boundary layer based on the known velocity data and on the number of fans that mark the core, accounting for the edge fans as well. Additional tuning of the duty cycles might be needed.

Finally, although linear boundary layer profiles could not be developed under these shear layer modes, the insights learned from the streamwise velocity profiles might help in creating strategies to expand the uniform flow core for a single fan unit. It should be assessed whether increasing the duty cycles of the edge fans by higher values from the middle fan could extend the core over a larger region, as well as how this adjustment would affect the uniformity and turbulence intensity of the extended core.

4.3. Gust

This part of chapter 4 investigates the capability of the system to generate gust at several predefined frequencies and amplitudes. First, the raw signals of each case are shown in comparison with the predefined mean and amplitude. Next, to check whether the stream oscillates at the predefined frequency, the PSD of each signal is consulted. The final subsection opens a discussion about the fidelity of the generated gust with respect to the initial conditions, and the degree of utility in possible future aerodynamic experiments.

4.3.1. Time evolution of the streamwise velocity component

This subsection aims to qualitatively compare the mean and the spread of the fluctuations with the reference mean velocity and reference amplitude range corresponding to the operating duty cycles. The comparison is done between the operating frequencies of each amplitude case, at the middle field and far field locations. Due to the qualitative purpose of this subsection, the signals are filtered using a low-pass filter, which eliminates frequencies above 50% of the Nyquist frequency.

There are two important mentions to make. First, the minimum and maximum expected velocity amplitudes are not equally apart from the mean, as foreseen in Table 3.4. This is because of the relatively nonlinear nature of the variation of rotational speed across the operating duty cycle range, reflected by the convective velocity as well. The second aspect is the lack of measurement data on the far field for the 0.8 Hz gust, for all the amplitude cases, due to lack of time. Additionally, measurement data for 0.4 Hz and 30% amplitude was cut out as well.

For each amplitude case, Figure 4.17, Figure 4.18 and Figure 4.19 illustrate the time evolution of the streamwise velocity (U_x), generated by the fans operating at 0.2 Hz, 0.4 Hz and 0.8 Hz. The signal is averaged at every time step, at the middle field and far field locations. Additionally, the plots contain information about the mean velocity of the signal (in red text and symbolized by the red dotted line), the expected mean velocity (in black text and symbolized by the middle black dotted line), and the minimum and maximum expected values (in black text, found above and below the expected mean). In the far field, the expected mean, minimum and maximum reference velocities are $U_{\text{far field, duty cycle}}$. Similarly, these were computed for the middle field.

The observations are general, and cover all the presented cases. The mean streamwise velocity remains very close to the expected reference velocity from the uniform flow across all cases, suggesting that the mean flow remains consistent regardless of the measurement position or frequency. This holds for both 0.2 Hz and 0.4 Hz, and it is reasonable to assume the same trend persists at 0.8 Hz. Another general aspect is the spread of the velocity fluctuations that appears to decrease as the frequency increases, compared to the lower and upper bounds. Later, the PSD could confirm this. It might indicate that the fans are not reaching the minimum and maximum duty cycles of the duty cycle discrete wave due to inertial limitations.

$A_{\text{mean, MFS}} = 50\%$; $A_{\text{MFS}} = 10\%$

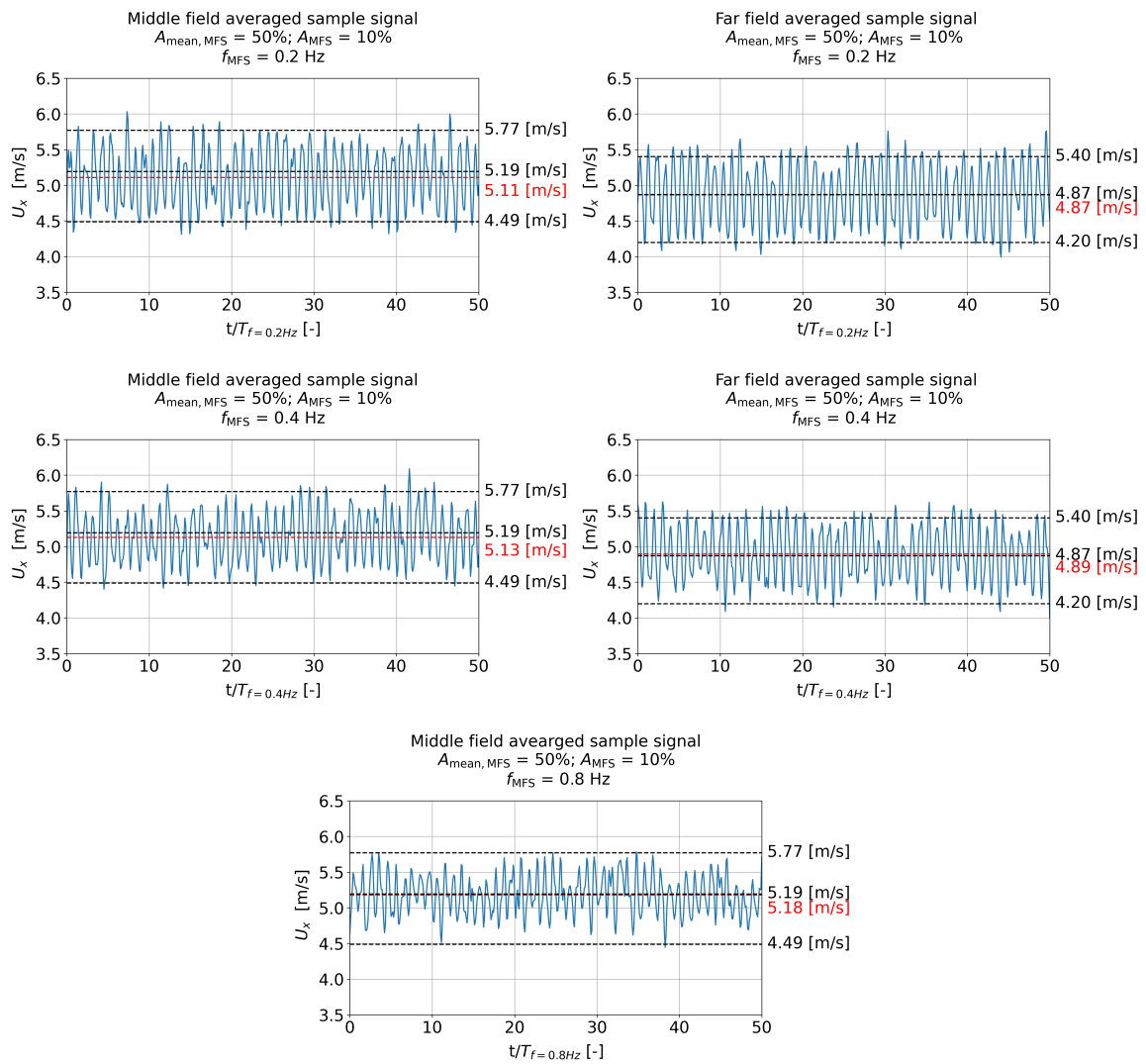


Figure 4.17: Streamwise velocity signal spatially averaged at each time step, with a comparison to the reference velocity at 40%, 50%, and 60% duty cycle for $A_{\text{mean, MFS}} = 50\%$ and $A_{\text{MFS}} = 10\%$. The comparison is made between the middle field and the far field.

The mean velocity of the signal (in red text and symbolized by the red dotted line), the expected mean velocity (in black text and symbolized by the middle black dotted line), and the minimum and maximum expected values (in black text, found above and below the expected mean) are marked. First row: 0.2 Hz. Second row: 0.4 Hz. Third row: 0.8 Hz.

$A_{\text{mean, MFS}} = 60\%$; $A_{\text{MFS}} = 20\%$

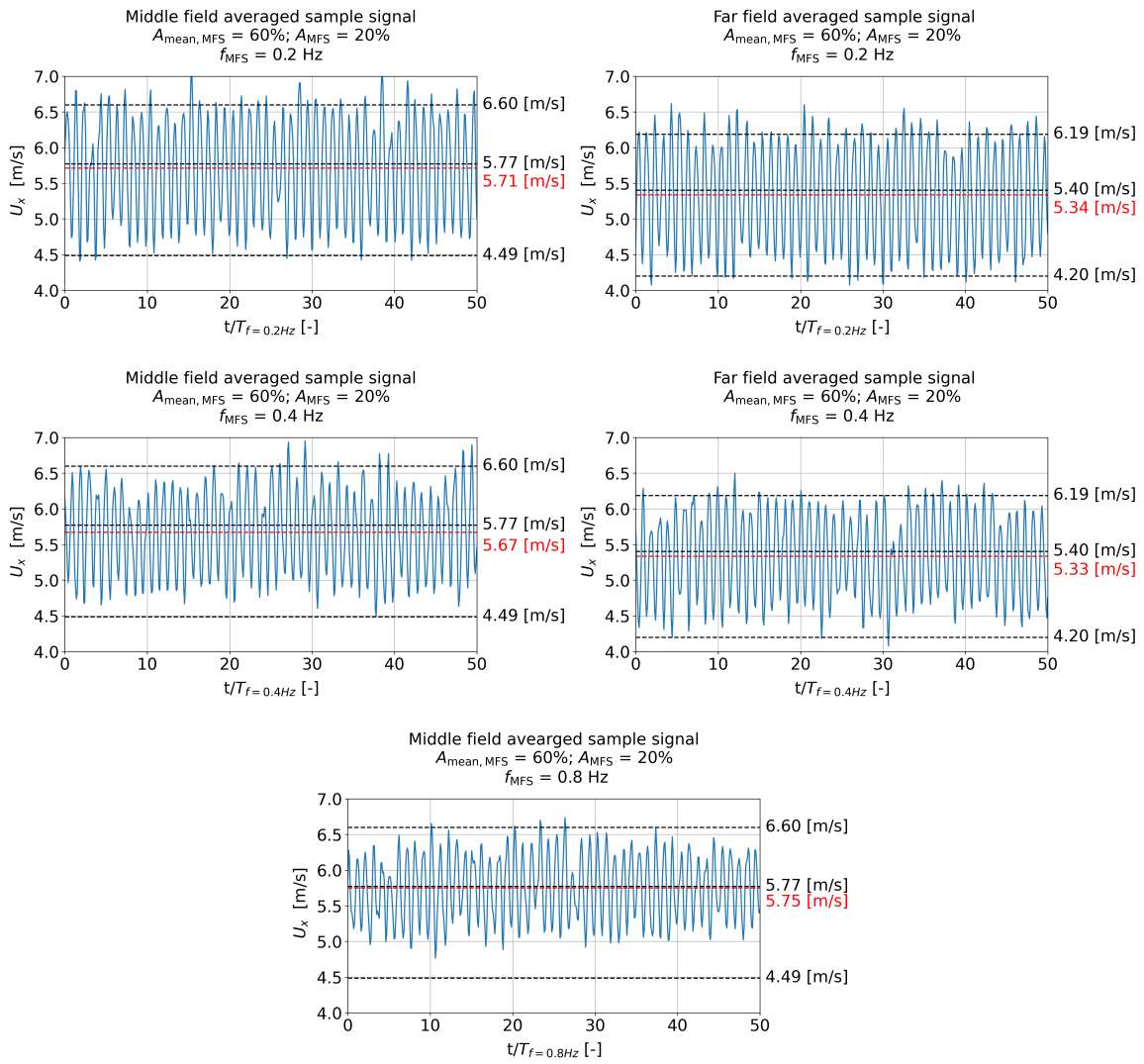


Figure 4.18: Streamwise velocity signal spatially averaged at each time step, with a comparison to the reference velocity at 40%, 60%, and 80% duty cycle for $A_{\text{mean, MFS}} = 60\%$ and $A_{\text{MFS}} = 20\%$. The comparison is made between the middle field and the far field. The mean velocity of the signal (in red text and symbolized by the red dotted line), the expected mean velocity (in black text and symbolized by the middle black dotted line), and the minimum and maximum expected values (in black text, found above and below the expected mean) are marked. First row: 0.2 Hz. Second row: 0.4 Hz. Third row: 0.8 Hz.

$A_{\text{mean, MFS}} = 50\%$; $A_{\text{MFS}} = 30\%$

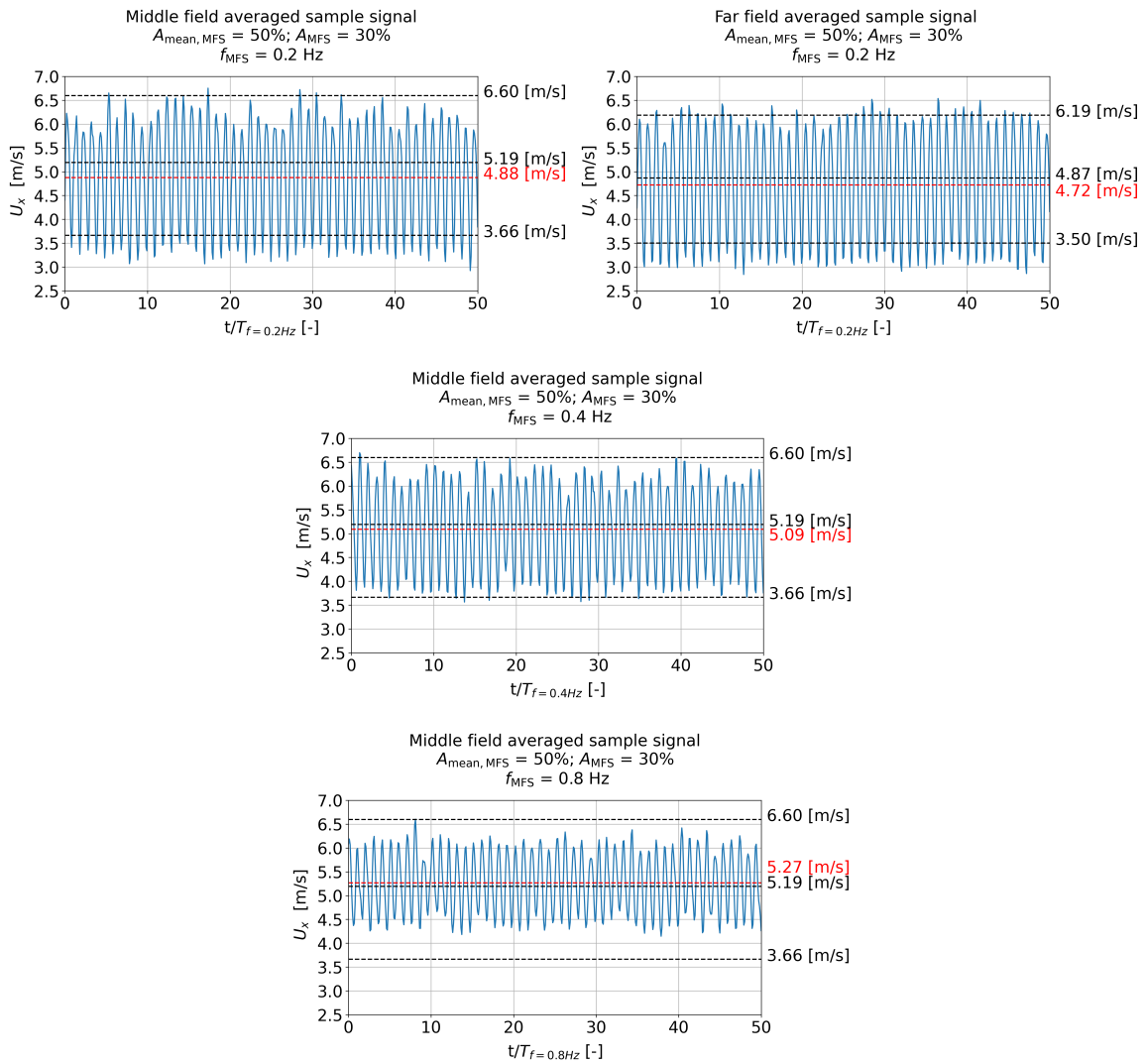


Figure 4.19: Streamwise velocity signal spatially averaged at each time step, with a comparison to the reference velocity at 20%, 50%, and 80% duty cycle for $A_{\text{mean, MFS}} = 50\%$ and $A_{\text{mean, MFS}} = 30\%$. The comparison is made between the middle field and the far field. The mean velocity of the signal (in red text and symbolized by the red dotted line), the expected mean velocity (in black text and symbolized by the middle black dotted line), and the minimum and maximum expected values (in black text, found above and below the expected mean) are marked. First row: 0.2 Hz. Second row: 0.4 Hz. Third row: 0.8 Hz.

4.3.2. Power Spectral Density

In this subsection, the distribution of the energy across all the frequencies of the signal up to the Nyquist frequency are presented for every amplitude case. Per case, a comparison is made between the resulting signals at 0.2 Hz, 0.4 Hz, 0.8 Hz. Similar to the comparison conducted in the previous subsection, the plots also display the PSD of the uniform flow signal at the corresponding duty cycle. The PSD is normalized by the mean streamwise velocity of each signal, meaning that the integral of the normalized PSD gives the normalized variance of the velocity fluctuations with respect to the corresponding mean velocity. The main observations can be generally applied for each amplitude case.

The dominant frequency for each signal is concentrated at the base frequency of 0.2 Hz, 0.41 Hz and 0.81 Hz respectively, suggesting that the flow responds according to the operating frequency of the fans. At the highest amplitude, 30%, energy peaks at double the base frequency are spotted, indicating that the oscillations have a second harmonica component as well. Flat energy is spread over the lowest frequencies of each signal, until the distinctive peaks arise, and lower fluctuating energies are spread over the higher frequencies. The uniform flow has no dominant peak, and the fluctuations are more random and spread across different frequencies.

The power decreases as frequency increases, meaning that velocity fluctuations contain less energy with increasing frequency, for the same amplitude. This was observed in subsection 4.3.1 through the reduction in the spread of the fluctuations along the mean. Comparing the amplitude cases, the power of the dominant frequencies increases with amplitude.

$A_{\text{mean, MFS}} = 50\%$; $A_{\text{mean, MFS}} = 10\%$

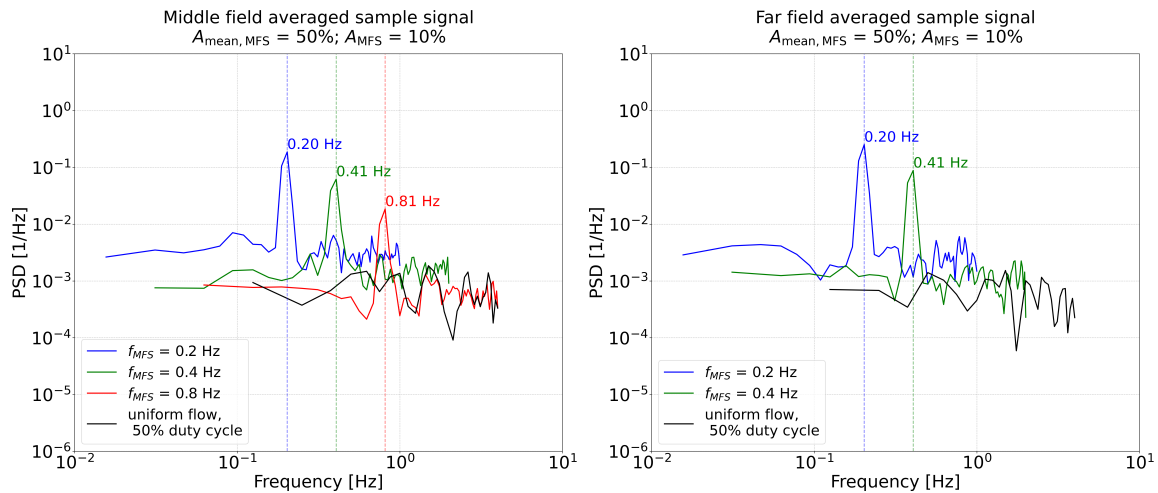


Figure 4.20: PSD for the gust case: $A_{\text{mean, MFS}} = 50\%$ and $A_{\text{mean, MFS}} = 10\%$, and uniform case: 50%. The left figure shows the energy distribution of the middle field signal at 0.2 Hz, 0.4 Hz, 0.8 Hz, and the uniform case. The right figure shows the energy distribution of the far field signal at 0.2 Hz, 0.4 Hz and the uniform case.

$A_{\text{mean, MFS}} = 60\%$; $A_{\text{mean, MFS}} = 20\%$

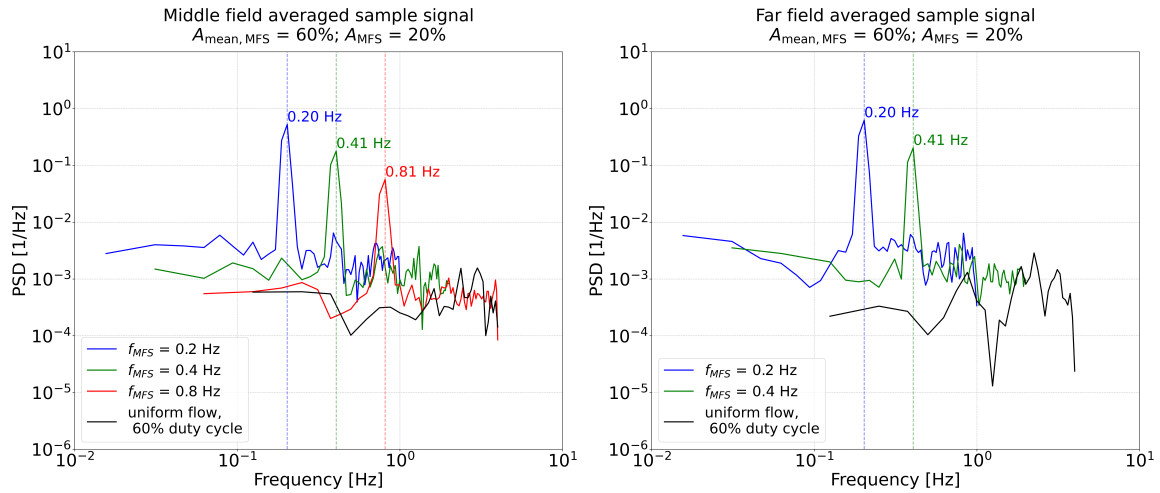


Figure 4.21: PSD for the gust case: $A_{\text{mean, MFS}} = 60\%$ and $A_{\text{mean, MFS}} = 20\%$, and uniform case: 60%. The left figure shows the energy distribution of the middle field signal at 0.2 Hz, 0.4 Hz, 0.8 Hz, and the uniform case. The right figure shows the energy distribution of the far field signal at 0.2 Hz, 0.4 Hz and the uniform case.

$A_{\text{mean, MFS}} = 50\%$; $A_{\text{mean, MFS}} = 30\%$

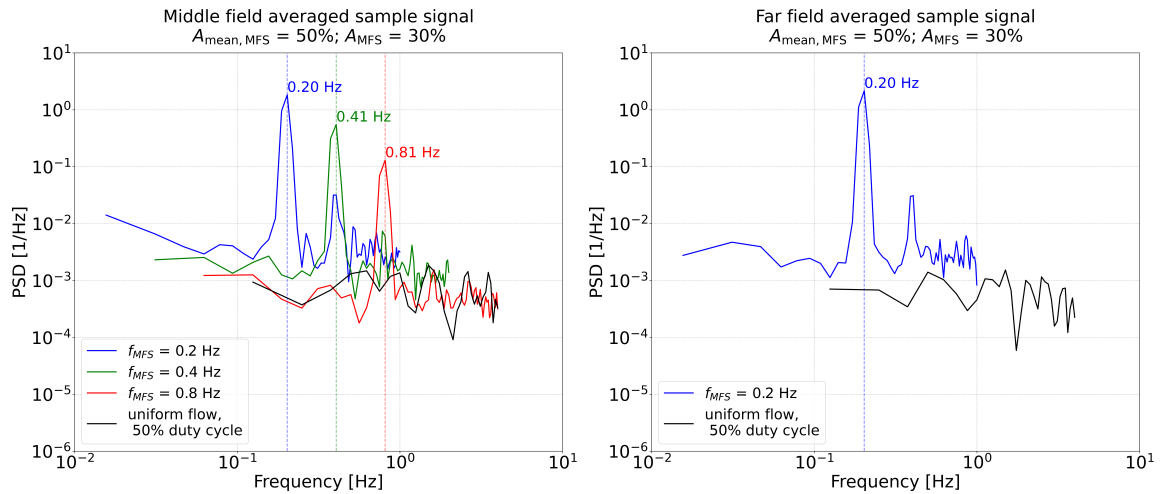


Figure 4.22: PSD for the gust case: $A_{\text{mean, MFS}} = 50\%$ and $A_{\text{mean, MFS}} = 30\%$, and uniform case: 50%. The left figure shows the energy distribution of the middle field signal at 0.2 Hz, 0.4 Hz, 0.8 Hz, and the uniform case. The right-hand side figure shows the energy distribution of the far field signal at 0.2 Hz and the uniform case.

4.3.3. Discussion

The key insight of the gust analysis is that the generated gusts are indeed oscillating at the operating frequencies of the fans, since most of the energy is concentrated at these frequencies, as shown by the PSD graphs. This is generally true for all three amplitude cases. Moreover, the PSD analysis also showed that the energy content decreases with increasing frequency, meaning that the fluctuations spread less from the mean at higher operating frequencies. Confirming the observations made by inspecting the raw signal, this might indicate that the fans are not reaching the minimum and maximum duty cycles from the discrete sinusoidal sequence fed in Arduino, due to inertial limitations. Regardless of this, the mean of the fluctuations seems to remain close to the uniform flow reference values in both the middle field and far field, independent of the frequency.

The suitability of the selected operating frequencies for aerodynamic and aeroelastic experiments involving structures exposed to gusty inflow conditions depends on the reduced frequency k and on the length

of the test model. The values for k found in studies about the characterization of gust-inducing devices, gust-modeling multi-fan systems or applications involving gusty inflows were all reported to be in the range of the unsteady flow condition subsection 2.1.2: $0.05 \leq k \leq 0.2$. In our case, with the current configuration, available inflow area (the core) of length 0.119 m ($= d_{fan}$), and inflow velocity of 6.2 m/s, the reduced frequencies corresponding to 0.2 Hz, 0.4 Hz and 0.8 Hz would be 0.012, 0.024 and 0.048, characteristic to quasi-steady flow. However, the model should be smaller than the length of the core, so full coverage would be assured. Instead, if the core is extended by adding extra modules to the system, the characteristic length could be larger and the reduced frequencies would reach the unsteady range.

Although a conclusion about the frequencies could be drawn, the amplitude is still not concisely characterized. This could be done statistically, by reconstructing the average cycle of the oscillation by averaging the ten phases across all cycles. Therefore, learning about the average amplitude defining the gust remains an open objective.

A proper characterization of the oscillatory motion of the fans should be conducted as well, independent of the aerodynamic characterization of the flow field. Knowing the operating frequency range and the actual duty cycles the fans achieve when accelerating and decelerating could close the gap between the expected and the actual amplitude of the gust, for every predefined frequency.

4.4. A-posteriori uncertainty quantification between planar and stereo PIV measurements

The identification of systematic and random sources in PIV measurements is not a trivial task. However, to ensure the reliability of the data measured with both planar and stereo PIV, a quantification measure of the uncertainty is adopted as follows. The vertical profiles of the mean streamwise velocity are extracted at the same location for both sets of PIV measurements, namely: at the center of the second cross-sectional plane, and at the corresponding distance of $2.5D_{MFS}$ in the vertical streamwise plane. They should approximately reflect the same velocity values, since they both represent the flow at the center of the system, $2.5D_{MFS}$ downstream from it, where diffusion dominates. To evaluate this correlation, the absolute error was computed between the two and plotted as vertical profiles for all duty cycles. An important note is that the vertical range was narrowed after the minimum and maximum height of the calibrated cross-sectional planes (Figure 3.14) from approximately $-1.8 \leq \frac{y}{d_{fan}} \leq 1.8$ to approximately $-1.5 \leq \frac{y}{d_{fan}} \leq 1.5$.

Figure 4.23 shows the two vertical profiles, and Figure 4.24 presents the corresponding absolute error. Overall, the difference between the two mean velocity profiles at the core are below an error of 0.4 m/s, considered relatively low. Towards the edge, however, the deviations increase with the duty cycle up to the order of 1 m/s, and slightly higher for 100%. This can be attributed to several error sources of the measurement chain, such as: differences in laser sheet coverage over the edges of measurement planes resulting in distinct distorted image planes and higher magnification factors; lack of flow calibration, since the flow was generated by operating the fans at the respective duty cycles only once, and on two distinct days; slight dissimilarities in the environmental conditions; finally, the physical justification of the edge shear layers that become more prominent with increasing duty cycles, affecting the local distribution of velocity.

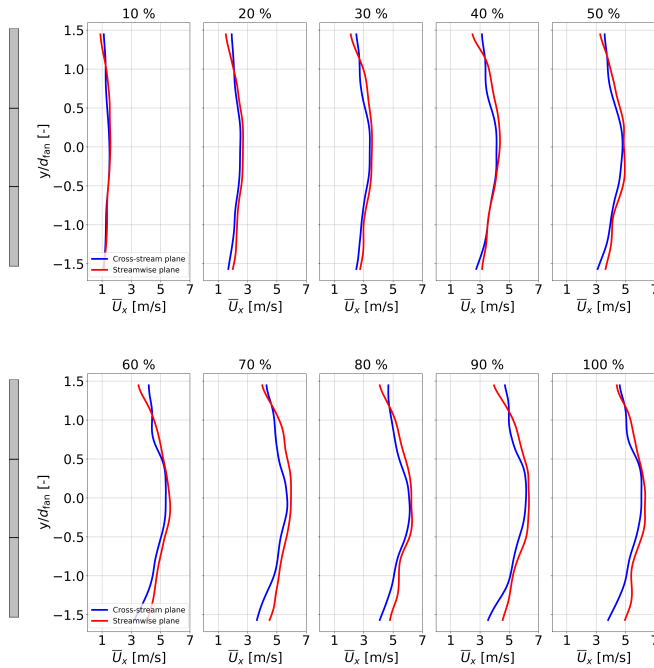


Figure 4.23: The vertical profiles of mean the streamwise velocity at the center of CS2 (blue) and at the corresponding location on the vertical streamwise plane (red)

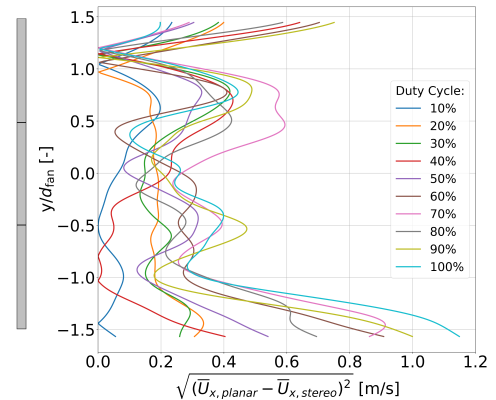


Figure 4.24: The absolute error [m/s] between the mean streamwise velocity vertical profiles measured with planar and stereo PIV at $2.5D_{MFS}$, at the center of the system

5

Conclusions & Outlook

This thesis attempted the aerodynamic characterization of the uniform flow, shear flow and gust generated by a 3 x 3 multi-fan wind generator, through PIV measurements of the flow field. First, the methodology was presented in chapter 3. In (section 3.1), the reader was familiarized with the MFS configuration and the duty cycle control routines in Arduino IDE. Then (section 3.2) introduced the flow cases and the corresponding test cases. After that, (section 3.3) detailed the setup of the experiment layout for the planar PIV measurements on three vertical streamwise planes and for the stereo PIV measurements on two cross-sectional planes. (section 3.4) presented the tools used to analyze the acquired data. The results for each flow case were showcased and discussed in chapter 4. In the following, the breakdown of each research question and the corresponding conclusions are brought together. Finally, the author of this report offers several recommendations and the future perspective of the multi-fan system.

5.1. Conclusions

1. What are the properties (velocity and vorticity distributions, turbulence intensity, and uniformity) of the flow produced by the 3 x 3 multi-fan system with all the fans operating at the same rotational speed?

1.1 How do these properties vary at different distances downstream from the system?

Recirculation bubbles of nearly $2.5 d_{fan}$ and jet-like flow regions are dominating the near field. At the edge of the system, an outer, asymmetric shear layer is formed, reducing the core to 1/9 of the MFS area. Strong wakes are induced by the rotation of the fans, adding complexity to the flow structures. In the far field, the core is characterized by 96% flow uniformity and around 11.5% turbulence intensity across the duty cycle operational range.

With a $N_{row} \times N_{column}$ square configuration, where N is the number of fans per row or column, and considering the size of the core of the flow equals the size of one fan, the core would be enlarged $(N_{row} - 2)(N_{column} - 2)$ times more than by having only one unit of 3 X 3 fans. The flow quality could be enhanced as well by adding hub extensions to keep the flow attached, and possibly maintain the high velocities defining the near field. Moreover, a honeycomb mesh could be added to eliminate the tangential velocity components and, by that, to reduce the swirling flow and turbulence intensity.

2. Is the 3 x 3 multi-fan system able to produce different predefined linear wind shear profiles?

The MFS was not able to reproduce ABL profiles given the chosen boundary layer modes, due to the effect of the strong shear layer developed at the edges. However, it was observed that by increasing the duty cycle of the edge fans by more than 5% duty cycle from the middle fan, more energy is introduced into the flow, resulting in a reduction of the shear layer in the observable frame. This might help as a strategy in increasing the length of the core for only one unit, and should be investigated. To achieve boundary layer profiles, the core should be enlarged by extending the height of the system with several rows of fans.

3. To what extent could the 3 x 3 multi-fan system generate a flow field that oscillates at the same operating frequency and amplitude of the fans?

3.1 How does the uniformity change depending on the frequency and amplitude?

The flow is periodic and oscillates at the selected operating frequencies of the fans at 0.2 Hz, 0.4 Hz and 0.8 Hz. The PSD plots confirmed that the dominant frequency of the generated signal is identical to the selected operating frequency of the fans for each operating amplitude. At the highest amplitude, 30% duty cycle, second harmonics of the 0.2 Hz and 0.4 Hz signals were identified at 0.4 Hz and 0.8 Hz, respectively. With the current system configuration ($d_{\text{fan}} = 0.119\text{m}$, $U_{\text{inflow}} = 6.2\text{ m/s}$), the corresponding reduced frequencies are 0.012, 0.024 and 0.048. Regarding the amplitude, both the PSD and the raw signals suggested that for the same operating amplitude, the amplitude of the fluctuations decreases as the frequency increases. This could be related to the inertial limitations of the fans that should be assessed in order to map the mechanical capabilities of the fans. Finally, the sub-question remains an open question for future investigations.

5.2. Limitations, recommendations & outlook

In the experimental phase, an unknown miscommunication between the camera and the laser triggers exhibited unwanted fluctuations in the maximum repetition rate of the laser during the measurements. For the measurement of the periodic flow, it had to be reduced from 15 Hz to 8 Hz to ensure steady pulsing. Therefore, considering we wanted to obtain 10 phases per cycle, the operational frequency of the system was limited to 0.8 Hz.

Considering this thesis is in the incipient stage of developing a multi-fan wind array, plenty of knowledge was gathered in guiding the next research at a more efficient, qualitative level of both the workflow strategy and the research target. The overall output of this work constitutes a solid base for future enhancements and investigations, such as:

1. Increasing the flow quality. Some suggestions include:
 - reducing the recirculation region by attaching a surface to the hub. The surface should follow the dimensions and shape of the bubble in order to keep the wake attached.
 - reducing the swirling structures induced by the rotation of the fans by filtering the tangential components through a honeycomb mesh; the turbulence intensity would also be reduced.
2. Extending the MFS by at least one unit to achieve a larger area characterized by high uniformity. This would allow a test model of reasonable dimensions to be subjected to the inflow the system generates.
3. Measuring the uniform, boundary layer and oscillating fields with hot wire anemometry, as it records the signal at higher sampling frequencies. Higher frequencies on the frequency spectrum would be captured, offering details up to the dissipative scales. Additionally, higher operating frequencies of the fans could be experimented with.
4. Experimenting strategies to generate boundary layer profiles.
 - developing a code based on the reference streamwise velocities in the far field and the number of fans that constitute the system.
 - live visualization during the experiments and instantaneous duty cycle adjustments until the desired profile is reached.
 - investigating the employment of tunnel floor and passive devices in aiding the formation of boundary layer.
5. Characterizing the oscillatory capabilities of the multi-fan system. Each combination of operating frequency and amplitude gives a unique response, and, as demonstrated, different from the expected signal. By documenting these aspects, an envelope of the operational frequency and amplitude range could be mapped. Moreover, since the reference velocity corresponding to the duty cycles is now known, the expected velocity amplitude could be predicted. This could close the gap between the expected flow behavior, dictated by the operation of the fans, and what is actually measured.

In conclusion, the multi-fan module developed and characterized in this thesis project exhibits aerodynamic properties that could be explored in simulating unsteady ABL conditions. The potential of this wind generation system should be further explored through its application in wind engineering studies and validated against wind tunnel and numerical data.

Bibliography

- [1] Giovanni Solari. *Wind Science and Engineering: Origins, Developments, Fundamentals and Advancements*. Springer Tracts in Civil Engineering. Springer Cham, 2019. ISBN: 978-3-030-18815-3. DOI: 10.1007/978-3-030-18815-3. URL: <https://link.springer.com/book/10.1007/978-3-030-18815-3#bibliographic-information>.
- [2] E. Halley. “An Historical Account of the Trade Winds and the Monsoons, Observable in the Seas Between and Near the Tropicks, with an Attempt to Assign the Physical Cause of the Said Winds”. In: *Philosophical Transactions of the Royal Society of London* 16 (1686), pp. 153–168.
- [3] Kite.org contributors. *History of Kites*. Kite.org. Accessed: Feb. 9, 2025. 2025. URL: <https://www.kite.org/about-kites/history-of-kites/>.
- [4] E. D. Archibald. “An Account of Some Preliminary Experiments with Biram’s Anemometers, Attached to Kite Strings”. In: *Nature* 31 (1885), pp. 66–68.
- [5] Th. Theodorsen. *General Theory of Aerodynamic Instability and the Mechanism of Flutter*. Tech. rep. 496. NACA, 1935, p. 103. URL: <https://ntrs.nasa.gov/citations/19930090935>.
- [6] I. E. Garrick and Wilmer H. Reed III. “Historical Development of Aircraft Flutter”. In: *Journal of Aircraft* 18.11 (Nov. 1981). NASA Langley Research Center, Hampton, Va.
- [7] J. C. Kaimal and J. J. Finnigan. *Atmospheric Boundary Layer Flows: Their Structure and Measurement*. Oxford University Press, 1994. ISBN: 978-0-19-506239-7. URL: <https://link.springer.com/article/10.1007/BF00712396>.
- [8] Roland Stull. *Practical Meteorology: An Algebra-based Survey of Atmospheric Science*. University of British Columbia, 2015.
- [9] J. B. Barlow, W. H. Rae Jr, and A. Pope. *Low-Speed Wind Tunnel Testing*. 3rd. John Wiley & Sons, 1999.
- [10] Flavio Noca et al. “Wind and Weather Facility for Testing Free-Flying Drones”. In: *AIAA Aviation 2019 Forum*. 2019, p. 2861. DOI: 10.2514/6.2019-2861.
- [11] Aurélien Walpen, Guillaume Catry, and Flavio Noca. “Real-Scale Atmospheric Wind and Turbulence Replication using a Fan-Array for Environmental Testing and UAV/AAM Validation”. In: *AIAA AVIATION 2022 Forum*. 2022. DOI: 10.2514/6.2022-3151.
- [12] Yang Yang et al. “Experimental investigation on the unsteady lift of an airfoil in a sinusoidal streamwise gust”. In: *Physics of Fluids* 29.5 (2017). URL: <https://doi.org/10.1063/1.4984243>.
- [13] D.A. Olejnik et al. “An Experimental Study of Wind Resistance and Power Consumption in MAVs with a Low-Speed Multi-Fan Wind System”. In: *2022 IEEE International Conference on Robotics and Automation (ICRA)*. 2022. DOI: 10.1109/ICRA46639.2022.9811834.
- [14] A. Nishi et al. “Turbulence control in multiple-fan wind tunnels”. In: *Journal of Wind Engineering and Industrial Aerodynamics* 67 (1997), pp. 861–872. DOI: [https://doi.org/10.1016/S0167-6105\(97\)00124-4](https://doi.org/10.1016/S0167-6105(97)00124-4).
- [15] J. T. Smith et al. “A simplified approach to simulate prescribed boundary layer flow conditions in a multiple controlled fan wind tunnel”. In: *Journal of Wind Engineering and Industrial Aerodynamics* 144 (2015), pp. 156–165.
- [16] Jia-Ying Wang et al. “A multiple-fan active control wind tunnel for outdoor wind speed and direction simulation”. In: *Review of Scientific Instruments* 89.3 (2018), p. 035108. DOI: 10.1063/1.5009897.
- [17] Eric Johnson and Jamey D. Jacob. “Development and Testing of a Gust and Shear Tunnel for NAVs and MAVs”. In: Jan. 2009. URL: <https://doi.org/10.2514/6.2009-64>.
- [18] P. J. Tavner et al. “Influence of Wind Speed on Wind Turbine Reliability”. In: *Wind Engineering* 30.1 (Jan. 2006), pp. 55–72. DOI: 10.1260/030952406777641441.

- [19] Tony Burton et al. *Wind Energy Handbook*. 2nd. John Wiley & Sons, 2011. ISBN: 978-0-470-69975-1. DOI: 10.1002/9781119992716.
- [20] International Electrotechnical Commission. *Wind turbines - Part 1: Design requirements*. Geneva, Switzerland: IEC, 2005.
- [21] R. Isaacs. "Airfoil theory for flows of variable velocity". In: *Journal of the Aeronautical Sciences* 12 (1945), p. 113. DOI: 10.2514/8.1127.
- [22] B. G. van der Wall and J. G. Leishman. "On the Influence of Time-Varying Flow Velocity on Unsteady Aerodynamics". In: *Journal of the American Helicopter Society* ().
- [23] A. Azzam and P. Lavoie. "Unsteady flow generation in a wind tunnel using an active grid". In: *Experiments in Fluids* 64 (2023), p. 29. DOI: 10.1007/s00348-023-03571-5.
- [24] P. R. Owen and H. K. Zienkiewicz. "The production of uniform shear flow in a wind tunnel". In: *Mechanics of Fluids Department, University of Manchester* (1957).
- [25] Dan Hlevca and Mircea Degeratu. "Atmospheric boundary layer modeling in a short wind tunnel". In: *Journal of Wind Engineering and Industrial Aerodynamics* 97.9-10 (2009), pp. 472–481. DOI: 10.1016/j.jweia.2009.07.012.
- [26] Jan Bartl and Lars Sætran. "Blind test comparison of the performance and wake flow between two in-line wind turbines exposed to different turbulent inflow conditions". In: *Wind Energy Science* 2 (2017), pp. 55–76. DOI: 10.5194/wes-2-55-2017.
- [27] Xingduo Guo et al. "A Wind Tunnel Experimental Study on the Wake Characteristics of a Horizontal Axis Wind Turbine". In: *Journal of Thermal Science* 34.1 (2025), pp. 145–158. DOI: 10.1007/s11630-024-2074-1.
- [28] H. W. Teunissen. "Simulation of the Planetary Boundary Layer in a Multiple-Jet Wind Tunnel". In: *Journal of Fluid Mechanics* 64 (1975), pp. 145–174. DOI: 10.1016/0004-6981(75)90065-7. URL: <https://www.sciencedirect.com/science/article/pii/0004698175900657?via%3Dihub>.
- [29] Paul M.G.J. Lancelot et al. "Design and testing of a low subsonic wind tunnel gust generator". In: *Advances in Aircraft and Spacecraft Science* 4.2 (2017), pp. 125–138. DOI: 10.12989/aas.2017.4.2.125.
- [30] J. Geertsen. "Development of a Gust Generator for a Low Speed Wind Tunnel". Master thesis. 2020.
- [31] ProCap Technology. *ProCap System*. 2025. URL: <https://www.procap.tech/>.
- [32] Modern Device. *Wind Sensor Rev. P*. URL: <https://moderndevice.com/products/wind-sensor-rev-p>.
- [33] Li et al. "Aerodynamic Characterization of a Fan-Array Wind Generator". In: *AIAA Journal* 62 (2024), pp. 9–10.
- [34] Flavio Noca et al. "Flow Profiling in a Windshaper for Testing Free-Flying Drones in Adverse Winds". In: *AIAA Aviation 2021 Forum*. AIAA, Aug. 2021. DOI: 10.2514/6.2021-2579.
- [35] Aurélien Walpen, Guillaume Catry, and Flavio Noca. "Real-Scale Atmospheric Wind and Turbulence Replication using a Fan-Array for Environmental Testing and UAV/AAM Validation". In: *AIAA SCITECH 2023 Forum*. National Harbor, MD & Online: American Institute of Aeronautics and Astronautics, 2023. ISBN: 978-1-62410-699-6. DOI: 10.2514/6.2023-0812. URL: <https://arc.aiaa.org/doi/10.2514/6.2023-0812>.
- [36] Guillaume Catry et al. "Performance Analysis of Rotorcraft Propulsion Units in a Combination of Wind and Icing Conditions". In: *AIAA Aviation 2021 Forum*. 2021. DOI: 10.2514/6.2021-2677. URL: <https://doi.org/10.2514/6.2021-2677>.
- [37] Cyprien de Sepibus and Flavio Noca. "Boundary layer tuning using PIV data in an open-jet multi-fan facility for ground-effect research". In: *Proceedings of the 15th International Symposium on Particle Image Velocimetry (ISPIV) 2023*. Presented at ISPIV 2023, 19-21 June 2023. San Diego, CA, USA: International Symposium on Particle Image Velocimetry (ISPIV), June 2023, p. 7.
- [38] F. Scarano J. Westerweel. *Handbook of Experimental Fluid Mechanics*. Springer, 2007.
- [39] M. Raffael et al. *Particle Image Velocimetry, A practical Guide*. 3rd ed. Springer, 2018.
- [40] B. Wieneke. "Stereo-PIV using self-calibration on particle images". In: *Experiments in Fluids* 39 (2005), pp. 267–280. DOI: 10.1007/s00348-005-0962-z.

-
- [41] R. D. Keane and R. J. Adrian. "Optimization of particle image velocimeters: II. Multiple pulsed systems". In: *Measurement Science and Technology* 2.10 (1991), p. 963. DOI: 10.1088/0957-0233/2/10/013. URL: <http://stacks.iop.org/0957-0233/2/i=10/a=013>.
- [42] *Product Data Sheet 4314 N/2H3P*. Tech. rep. ebmpapst.
- [43] P.D. Welch. "The use of fast Fourier transform for the estimation of power spectra: A method based on time averaging over short, modified periodograms". In: *IEEE Transactions on Audio and Electroacoustics* 15.2 (1967), pp. 70–73.

A

Electrical Installation

As mentioned in subsection 3.1.1, the wiring diagram and the current and power consumption of the MFS are displayed in this chapter.

A.1. Circuit diagram

The electrical circuit of the nine fans and the Arduino board is displayed in Figure A.1.

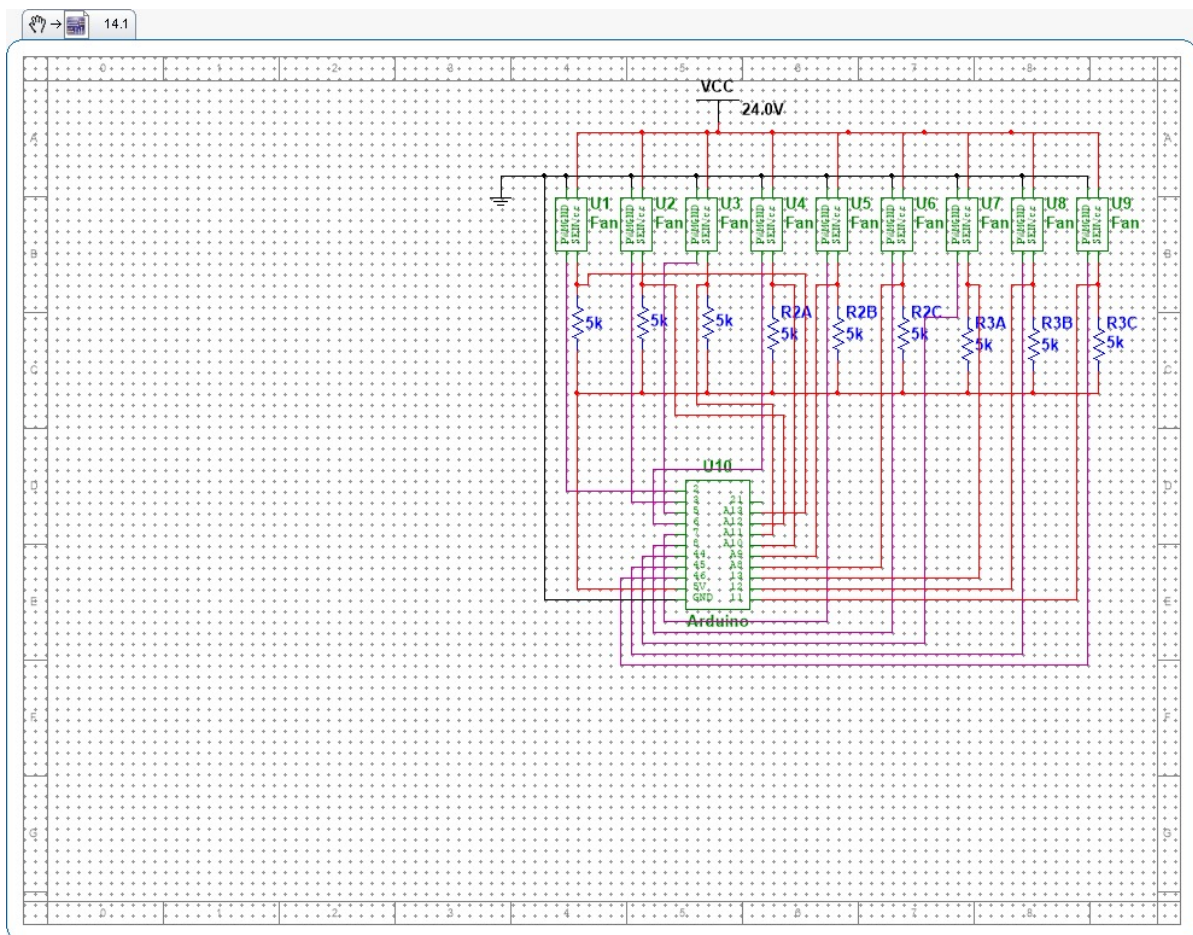


Figure A.1: Circuit diagram of the 9 fans and Arduino

A.2. Current & power consumption

The current and power consumption of the MFS were recorded at different duty cycles, to insure the fans are operating within safety limits during the experiments. The data represents the visually approximated mean values of the current and power displayed on the power source.

Duty Cycle [%]	Mean Current [A]	Mean Power [W]
10	0.34	8.3
20	0.65	15.7
30	1.09	26.1
40	1.63	39.3
50	2.27	54.5
60	1.96	71.8
70	3.68	88.2
80	4.32	103.2
90	4.33	103.8
100	4.33	104

Table A.1: Current and power consumption of the prototype

B

Multi-fan System Control

The current chapter provides the Arduino sketches used to control the fans for each flow case, as indicated in subsection 3.1.2.

B.1. Arduino Sketch for Constant Duty Cycle Control

```
1 // The purpose of this code is to control the fans for the uniform and shear flow cases
2
3 #include <TimerThree.h> // Library to control Timer3
4 #include <TimerFour.h> // Library to control Timer4
5 #include <TimerFive.h> // Library to control Timer5
6 #include <PinChangeInterrupt.h> // Library to handle pin change interrupts
7
8 // Define pin numbers for fans
9 int Fan1Pin = 2; // Fan 1 control pin
10 int Fan2Pin = 3; // Fan 2 control pin
11 int Fan3Pin = 5; // Fan 3 control pin
12 int Fan4Pin = 6; // Fan 4 control pin
13 int Fan5Pin = 7; // Fan 5 control pin
14 int Fan6Pin = 8; // Fan 6 control pin
15 int Fan7Pin = 44; // Fan 7 control pin
16 int Fan8Pin = 45; // Fan 8 control pin
17 int Fan9Pin = 46; // Fan 9 control pin
18
19 // Variables for user inputs and duty cycles
20 int a, b, c; // Flags to track user input steps
21 float dutyCycle1; // Duty cycle for row 1
22 float dutyCycle2; // Duty cycle for row 2
23 float dutyCycle3; // Duty cycle for row 3
24
25 // Sense pins for RPM measurement
26 const int PIN_SENSE[9] = {11, 12, 13, 64, 65, 66, 67, 68, 69};
27 #define DEBOUNCE 0 // Debounce time to filter signal noise
28 #define FANSTUCK_THRESHOLD 500 // Threshold in ms to detect fan stuck condition
29
30 // Timestamps for interrupts (used to calculate RPM)
31 unsigned long volatile ts1 = 0, ts2 = 0, ts3 = 0, ts4 = 0, ts5 = 0, ts6 = 0;
32 unsigned long volatile ts7 = 0, ts8 = 0, ts9 = 0, ts10 = 0, ts11 = 0, ts12 = 0;
33 unsigned long volatile ts13 = 0, ts14 = 0, ts15 = 0, ts16 = 0, ts17 = 0, ts18 = 0;
34
35 // Interrupt Service Routines (ISRs) for RPM sensing
36 void tachISR0() {
37     unsigned long m=millis();
38     if((m-ts2)>DEBOUNCE){
39         ts1=ts2;
40         ts2=m;
41     }
42 }
```

```
43
44 void tachISR1() {
45     unsigned long m=millis();
46     if((m-ts4)>DEBOUNCE){
47         ts3=ts4;
48         ts4=m;
49     }
50 }
51
52 void tachISR2() {
53     unsigned long m=millis();
54     if((m-ts6)>DEBOUNCE){
55         ts5=ts6;
56         ts6=m;
57     }
58 }
59
60 void tachISR3() {
61     unsigned long m=millis();
62     if((m-ts8)>DEBOUNCE){
63         ts7=ts8;
64         ts8=m;
65     }
66 }
67
68 void tachISR4() {
69     unsigned long m=millis();
70     if((m-ts10)>DEBOUNCE){
71         ts9=ts10;
72         ts10=m;
73     }
74 }
75
76 void tachISR5() {
77     unsigned long m=millis();
78     if((m-ts12)>DEBOUNCE){
79         ts11=ts12;
80         ts12=m;
81     }
82 }
83
84 void tachISR6() {
85     unsigned long m=millis();
86     if((m-ts14)>DEBOUNCE){
87         ts13=ts14;
88         ts14=m;
89     }
90 }
91
92 void tachISR7() {
93     unsigned long m=millis();
94     if((m-ts16)>DEBOUNCE){
95         ts15=ts16;
96         ts16=m;
97     }
98 }
99
100 void tachISR8() {
101     unsigned long m=millis();
102     if((m-ts18)>DEBOUNCE){
103         ts17=ts18;
104         ts18=m;
105     }
106 }
107
108 // Function to calculate RPM for each fan using timestamps
109 unsigned long calcRPMf1(){
110     if(millis()-ts2<FANSTUCK_THRESHOLD&&ts2!=0){
111
112         return (60000/(ts2-ts1))/2;
113     }else return 0;
```

```

114 }
115
116 unsigned long calcRPMF2(){
117     if(millis()-ts4<FANSTUCK_THRESHOLD&&ts4!=0){
118
119         return (60000/(ts4-ts3))/2;
120     }else return 0;
121 }
122
123 unsigned long calcRPMF3(){
124     if(millis()-ts6<FANSTUCK_THRESHOLD&&ts6!=0){
125
126         return (60000/(ts6-ts5))/2;
127     }else return 0;
128 }
129
130 unsigned long calcRPMF4(){
131     if(millis()-ts8<FANSTUCK_THRESHOLD&&ts8!=0){
132
133         return (60000/(ts8-ts7))/2;
134     }else return 0;
135 }
136
137 unsigned long calcRPMF5(){
138     if(millis()-ts10<FANSTUCK_THRESHOLD&&ts10!=0){
139
140         return (60000/(ts10-ts9))/2;
141     }else return 0;
142 }
143
144 unsigned long calcRPMF6(){
145     if(millis()-ts12<FANSTUCK_THRESHOLD&&ts12!=0){
146
147         return (60000/(ts12-ts11))/2;
148     }else return 0;
149 }
150
151 unsigned long calcRPMF7(){
152     if(millis()-ts14<FANSTUCK_THRESHOLD&&ts14!=0){
153
154         return (60000/(ts14-ts13))/2;
155     }else return 0;
156 }
157
158 unsigned long calcRPMF8(){
159     if(millis()-ts16<FANSTUCK_THRESHOLD&&ts16!=0){
160
161         return (60000/(ts16-ts15))/2;
162     }else return 0;
163 }
164
165 unsigned long calcRPMF9(){
166     if(millis()-ts18<FANSTUCK_THRESHOLD&&ts18!=0){
167
168         return (60000/(ts18-ts17))/2;
169     }else return 0;
170 }
171
172
173 void setup() {
174     Serial.begin(9600); // Initialize serial communication at 9600 baud
175     Timer3.initialize(40); // Initialize Timer3 for PWM
176     Timer4.initialize(40); // Initialize Timer4 for PWM
177     Timer5.initialize(40); // Initialize Timer5 for PWM
178
179     // Configure sense pins as input with pull-up resistors
180     for (int i = 0; i < 9; i++) {
181         pinMode(PIN_SENSE[i], INPUT_PULLUP);
182     }
183
184     // Attach interrupt handlers for each fan

```

```

185   attachPCINT(digitalPinToPCINT(PIN_SENSE[0]), tachISR0, FALLING);
186   attachPCINT(digitalPinToPCINT(PIN_SENSE[1]), tachISR1, FALLING);
187   attachPCINT(digitalPinToPCINT(PIN_SENSE[2]), tachISR2, FALLING);
188   // Repeat for all fans...
189
190   Serial.println("Set Duty Cycle of Row 1:");
191 }
192
193 void loop() {
194   // User input for duty cycle of row 1
195   if (Serial.available() > 0 && a != 1) {
196     String str1 = Serial.readString();
197     a = 1;
198     dutyCycle1 = str1.toFloat();
199     Serial.print("Duty cycle set to ");
200     Serial.println(dutyCycle1);
201     Serial.println("Set Duty Cycle of Row 2:");
202   }
203   delay(500);
204
205   // User input for duty cycle of row 2
206   if (Serial.available() > 0 && b != 1 && a == 1) {
207     String str2 = Serial.readString();
208     b = 1;
209     dutyCycle2 = str2.toFloat();
210     Serial.print("Duty cycle set to ");
211     Serial.println(dutyCycle2);
212     Serial.println("Set Duty Cycle of Row 3:");
213   }
214   delay(500);
215
216   // User input for duty cycle of row 3
217   if (Serial.available() > 0 && c != 1 && b == 1) {
218     String str3 = Serial.readString();
219     c = 1;
220     dutyCycle3 = str3.toFloat();
221     Serial.print("Duty cycle set to ");
222     Serial.println(dutyCycle3);
223   }
224
225   // Once all duty cycles are set, apply PWM to fans
226   if (a == 1 && b == 1 && c == 1) {
227     Timer3.pwm(Fan1Pin, (dutyCycle1 / 100) * 1023);
228     Timer3.pwm(Fan2Pin, (dutyCycle1 / 100) * 1023);
229     Timer3.pwm(Fan3Pin, (dutyCycle1 / 100) * 1023);
230     Timer4.pwm(Fan4Pin, (dutyCycle2 / 100) * 1023);
231     Timer4.pwm(Fan5Pin, (dutyCycle2 / 100) * 1023);
232     Timer4.pwm(Fan6Pin, (dutyCycle2 / 100) * 1023);
233     Timer5.pwm(Fan7Pin, (dutyCycle3 / 100) * 1023);
234     Timer5.pwm(Fan8Pin, (dutyCycle3 / 100) * 1023);
235     Timer5.pwm(Fan9Pin, (dutyCycle3 / 100) * 1023);
236
237     // Display RPM for each fan
238     Serial.println("Calculating RPM...");
239     delay(3000);
240     Serial.print("RPM Fan1: "); Serial.println(calcRPMF1());
241     // Repeat for all fans...
242     a = b = c = 0; // Reset input flags
243     Serial.println("Reset Duty Cycle of Fans if needed");
244   }
245 }

```

B.2. Sine Wave Definition & Arduino Sketch for Oscillating Duty Cycle Control

This section provides the Arduino sketch that allows a duty cycle sequence to be given as input, as introduced in subsection 3.1.2. The sequence can be obtained in a different programming language by creating a sinusoidal profile, characterized by the desired frequency and amplitude range. This profile should be discretized

into a number of samples distributed based on a sampling frequency. The resulting sequence of duty cycle values that shape the discrete sinusoidal profile, followed by the sampling period, are given as the single input line to control all the fans.

```

1 // The purpose of this code is to control the fans using sinusoidal duty cycle
  variation for gust generation.
2
3 #include <TimerThree.h>
4 #include <TimerFour.h>
5 #include <TimerFive.h>
6 #include <PinChangeInterrupt.h>
7
8 int Fan1Pin = 2; // fan_11, 11
9 int Fan2Pin = 3; // fan_12, 12
10 int Fan3Pin = 5; // fan_13, 13
11 int Fan4Pin = 6; // fan21, D64/A10
12 int Fan5Pin = 7; // fan22, D65/A11
13 int Fan6Pin = 8; // fan23, D66/A12
14 int Fan7Pin = 44; // fan31, D67/A13
15 int Fan8Pin = 45; // fan32, D68/A14
16 int Fan9Pin = 46; // fan33, D69/A15
17
18 const int PIN_SENSE[9] = {11,12,13,64,65,66,67,68,69}; // Where the fan sense pin is
  connected. Must be an interrupt cable pin (2 or 3 on Arduino Uno)
19 #define DEBOUNCE 0
20 #define FANSTUCK_THRESHOLD 500 // If no interrupts were received for 500ms, consider
  the fan as stuck and report 0 RPM
21
22 unsigned long volatile ts1=0,ts2=0,ts3=0,ts4=0,ts5=0,ts6=0;
23 unsigned long volatile ts7=0,ts8=0,ts9=0,ts10=0,ts11=0,ts12=0;
24 unsigned long volatile ts13=0,ts14=0,ts15=0,ts16=0,ts17=0,ts18=0;
25
26 const int maxValues = 1000; // Maximum number of duty cycle values
27 float dutyCycleValues[maxValues]; // Array to store the duty cycle values
28 int numValues = 0; // Number of duty cycle values entered
29 int index = 0;
30 int userDelay = 4000; // Default delay value
31 bool shouldPrint = true;
32
33 void tachISR0() {
34     unsigned long m=millis();
35     if((m-ts2)>DEBOUNCE){
36         ts1=ts2;
37         ts2=m;
38     }
39 }
40
41 void tachISR1() {
42     unsigned long m=millis();
43     if((m-ts4)>DEBOUNCE){
44         ts3=ts4;
45         ts4=m;
46     }
47 }
48
49 void tachISR2() {
50     unsigned long m=millis();
51     if((m-ts6)>DEBOUNCE){
52         ts5=ts6;
53         ts6=m;
54     }
55 }
56
57 void tachISR3() {
58     unsigned long m=millis();
59     if((m-ts8)>DEBOUNCE){
60         ts7=ts8;
61         ts8=m;
62     }
63 }
64

```

```
65 void tachISR4() {
66     unsigned long m=millis();
67     if((m-ts10)>DEBOUNCE){
68         ts9=ts10;
69         ts10=m;
70     }
71 }
72
73 void tachISR5() {
74     unsigned long m=millis();
75     if((m-ts12)>DEBOUNCE){
76         ts11=ts12;
77         ts12=m;
78     }
79 }
80
81 void tachISR6() {
82     unsigned long m=millis();
83     if((m-ts14)>DEBOUNCE){
84         ts13=ts14;
85         ts14=m;
86     }
87 }
88
89 void tachISR7() {
90     unsigned long m=millis();
91     if((m-ts16)>DEBOUNCE){
92         ts15=ts16;
93         ts16=m;
94     }
95 }
96
97 void tachISR8() {
98     unsigned long m=millis();
99     if((m-ts18)>DEBOUNCE){
100         ts17=ts18;
101         ts18=m;
102     }
103 }
104
105 unsigned long calcRPMF1(){
106     if(millis()-ts2<FANSTUCK_THRESHOLD&&ts2!=0){
107         return (60000/(ts2-ts1))/2;
108     }else return 0;
109 }
110
111 unsigned long calcRPMF2(){
112     if(millis()-ts4<FANSTUCK_THRESHOLD&&ts4!=0){
113         return (60000/(ts4-ts3))/2;
114     }else return 0;
115 }
116
117 unsigned long calcRPMF3(){
118     if(millis()-ts6<FANSTUCK_THRESHOLD&&ts6!=0){
119         return (60000/(ts6-ts5))/2;
120     }else return 0;
121 }
122
123 unsigned long calcRPMF4(){
124     if(millis()-ts8<FANSTUCK_THRESHOLD&&ts8!=0){
125         return (60000/(ts8-ts7))/2;
126     }else return 0;
127 }
128
129 unsigned long calcRPMF5(){
130     if(millis()-ts10<FANSTUCK_THRESHOLD&&ts10!=0){
131         return (60000/(ts10-ts9))/2;
132     }else return 0;
133 }
134
135 unsigned long calcRPMF6(){
```

```

136     if(millis()-ts12<FANSTUCK_THRESHOLD&&ts12!=0){
137         return (60000/(ts12-ts11))/2;
138     }else return 0;
139 }
140
141 unsigned long calcRPMF7(){
142     if(millis()-ts14<FANSTUCK_THRESHOLD&&ts14!=0){
143         return (60000/(ts14-ts13))/2;
144     }else return 0;
145 }
146
147 unsigned long calcRPMF8(){
148     if(millis()-ts16<FANSTUCK_THRESHOLD&&ts16!=0){
149         return (60000/(ts16-ts15))/2;
150     }else return 0;
151 }
152
153 unsigned long calcRPMF9(){
154     if(millis()-ts18<FANSTUCK_THRESHOLD&&ts18!=0){
155         return (60000/(ts18-ts17))/2;
156     }else return 0;
157 }
158
159 void setup() {
160     Serial.begin(9600);
161     Serial.setTimeout(10);
162     Timer3.initialize(40);
163     Timer4.initialize(40);
164     Timer5.initialize(40);
165
166     pinMode(PIN_SENSE[0], INPUT_PULLUP);
167     pinMode(PIN_SENSE[1], INPUT_PULLUP);
168     pinMode(PIN_SENSE[2], INPUT_PULLUP);
169     pinMode(PIN_SENSE[3], INPUT_PULLUP);
170     pinMode(PIN_SENSE[4], INPUT_PULLUP);
171     pinMode(PIN_SENSE[5], INPUT_PULLUP);
172     pinMode(PIN_SENSE[6], INPUT_PULLUP);
173     pinMode(PIN_SENSE[7], INPUT_PULLUP);
174     pinMode(PIN_SENSE[8], INPUT_PULLUP); //set the sense pin as input with pullup
        resistor
175
176     attachPCINT(digitalPinToPCINT(PIN_SENSE[0]), tachISR0, FALLING);
177     attachPCINT(digitalPinToPCINT(PIN_SENSE[1]), tachISR1, FALLING);
178     attachPCINT(digitalPinToPCINT(PIN_SENSE[2]), tachISR2, FALLING);
179     attachPCINT(digitalPinToPCINT(PIN_SENSE[3]), tachISR3, FALLING);
180     attachPCINT(digitalPinToPCINT(PIN_SENSE[4]), tachISR4, FALLING);
181     attachPCINT(digitalPinToPCINT(PIN_SENSE[5]), tachISR5, FALLING);
182     attachPCINT(digitalPinToPCINT(PIN_SENSE[6]), tachISR6, FALLING);
183     attachPCINT(digitalPinToPCINT(PIN_SENSE[7]), tachISR7, FALLING);
184     attachPCINT(digitalPinToPCINT(PIN_SENSE[8]), tachISR8, FALLING);
185
186     Serial.println("Enter duty cycle values followed by the delay in milliseconds,
        separated by spaces (max 10 values):");
187     Serial.println("Example: 50 70 50 30 50 4000");
188 }
189
190 void loop() {
191     // Read duty cycle values and delay from serial monitor
192     if (Serial.available() > 0) {
193         String input = Serial.readStringUntil('\n'); // Read input from the serial
            monitor
194         char inputArray[input.length() + 1];
195         input.toCharArray(inputArray, input.length() + 1); // Convert input to a
            character array
196
197         // Split the input 60 Ostring into individual values
198         char *token = strtok(inputArray, " ");
199         numValues = 0; // Reset numValues for new input
200         while (token != NULL && numValues < maxValues) {
201             dutyCycleValues[numValues] = atof(token); // Convert each token to a float
                and store it in the array

```

```

202     numValues++;
203     token = strtok(NULL, " ");
204 }
205
206 // The last token should be the delay value
207 if (numValues > 0) {
208     userDelay = dutyCycleValues[numValues - 1];
209     numValues--; // Decrease the count of duty cycle values
210 }
211
212 Serial.print("Duty cycle values received: ");
213 for (int i = 0; i < numValues; i++) {
214     Serial.print(dutyCycleValues[i]);
215     if (i < numValues - 1) {
216         Serial.print(", ");
217     }
218 }
219 Serial.println();
220 Serial.print("Delay received: ");
221 Serial.println(userDelay);
222 index = 0; // Reset index for the new set of values
223 }
224
225 // Set the PWM for fans based on duty cycle values in sequence
226 if (numValues > 0) {
227     float dutyCycle1 = dutyCycleValues[index];
228     if (shouldPrint) {
229         Serial.print("PWM Fan, Duty Cycle = ");
230         Serial.println(dutyCycle1);
231
232         Timer3.pwm(Fan1Pin, (dutyCycle1 / 100) * 1023);
233         Timer3.pwm(Fan2Pin, (dutyCycle1 / 100) * 1023);
234         Timer3.pwm(Fan3Pin, (dutyCycle1 / 100) * 1023);
235         Timer4.pwm(Fan4Pin, (dutyCycle1 / 100) * 1023);
236         Timer4.pwm(Fan5Pin, (dutyCycle1 / 100) * 1023);
237         Timer4.pwm(Fan6Pin, (dutyCycle1 / 100) * 1023);
238         Timer5.pwm(Fan7Pin, (dutyCycle1 / 100) * 1023);
239         Timer5.pwm(Fan8Pin, (dutyCycle1 / 100) * 1023);
240         Timer5.pwm(Fan9Pin, (dutyCycle1 / 100) * 1023);
241
242         //Serial.print("RPM: ");
243         //Serial.println(calcRPMF3());
244     }
245
246     delay(userDelay); // Wait for the specified delay before updating to the next
                       // value
247     index = (index + 1) % numValues; // Move to the next value in the sequence,
                                       // wrapping around if necessary
248 }
249 }

```

C

Preliminary Speed Approximation

In anticipation of the PIV measurements, the preliminary speed was approximated and used in computing the time separation between the pulses for each duty cycle, and under the corresponding optimization rule. The resulting time steps are presented in subsection 3.3.4. For this, the total and static pressure were measured using a Pitot-static probe, and the converted dynamic pressure was used to determine the velocity at different duty cycles. The resulting dependency is shown in Appendix C

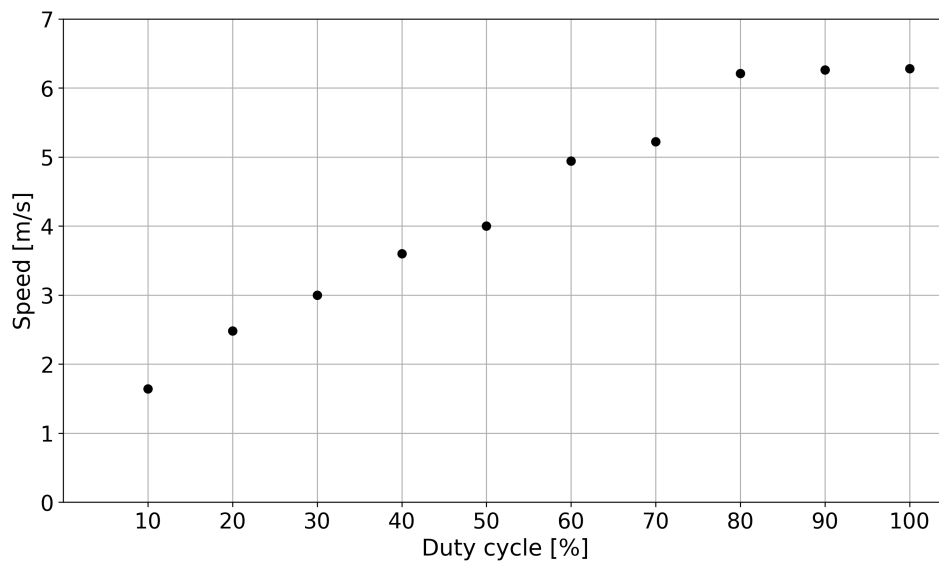


Figure C.1: Duty Cycle [%] vs Flow Speed [m/s] (measurements with Pitot-static probe)

D

Uniform field results

One of the goals in section 4.1 was to compare the flow field generated by the fans operating at 50% and 100%, observed to be similar. The conclusion can be extended to the other duty cycles as well. The aim of this chapter is to present the flow fields colored by the mean streamwise velocity (in vertical streamwise plane) and mean vorticity (in cross-sectional plane).

D.1. Vertical streamwise plane

Mean streamwise velocity field

Here, the mean streamwise velocity fields normalized by $\bar{U}_{x, \text{far field}, 100\%}$ are presented to show the field evolution with respect to the maximum velocity.

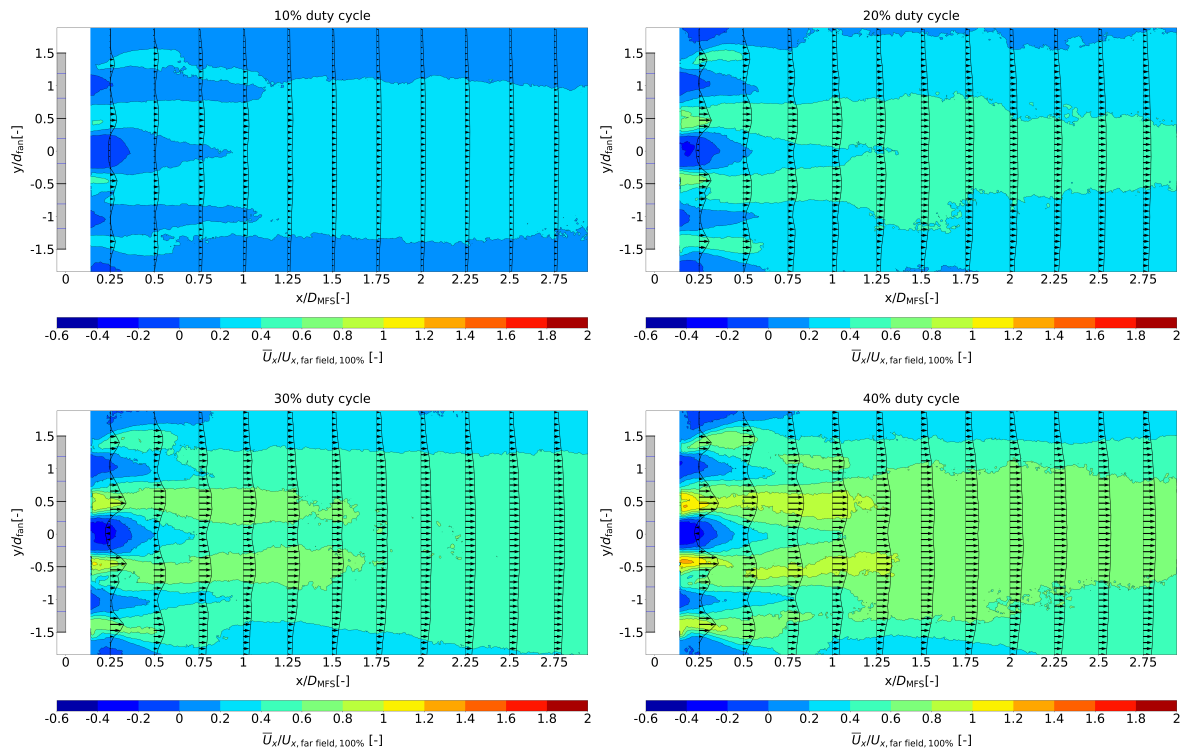


Figure D.1: Vertical streamwise plane colored by the mean streamwise velocity normalized by $\bar{U}_{x, \text{far field}, 100\%}$. The normalized streamwise velocity vectors are displayed at different locations downstream. Duty cycles: 10%-40%.

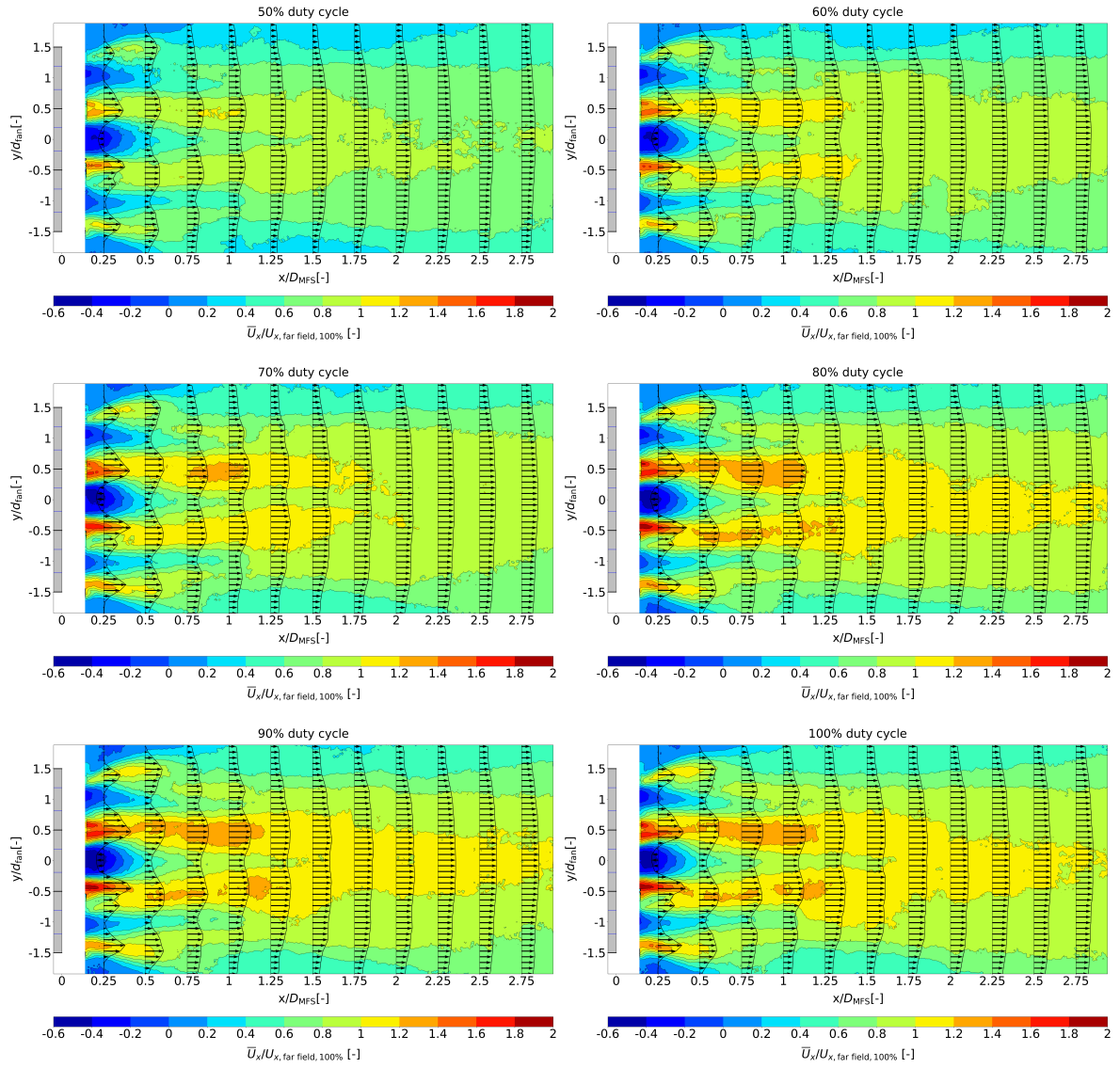


Figure D.2: Vertical streamwise plane colored by the mean streamwise velocity normalized by $\bar{U}_{x, \text{far field}, 100\%}$. The normalized streamwise velocity vectors are displayed at different locations downstream. Duty cycles: 50%-100%.

D.2. Cross-stream planes

Mean vorticity

As seen in Figure 4.1.2, the normalized mean vorticity appears to increase with the duty cycle, possibly because of a rapid increase of the tangential component with the rotational speed. This part provides the evolution of the normalized mean vorticity field with increasing duty cycle.

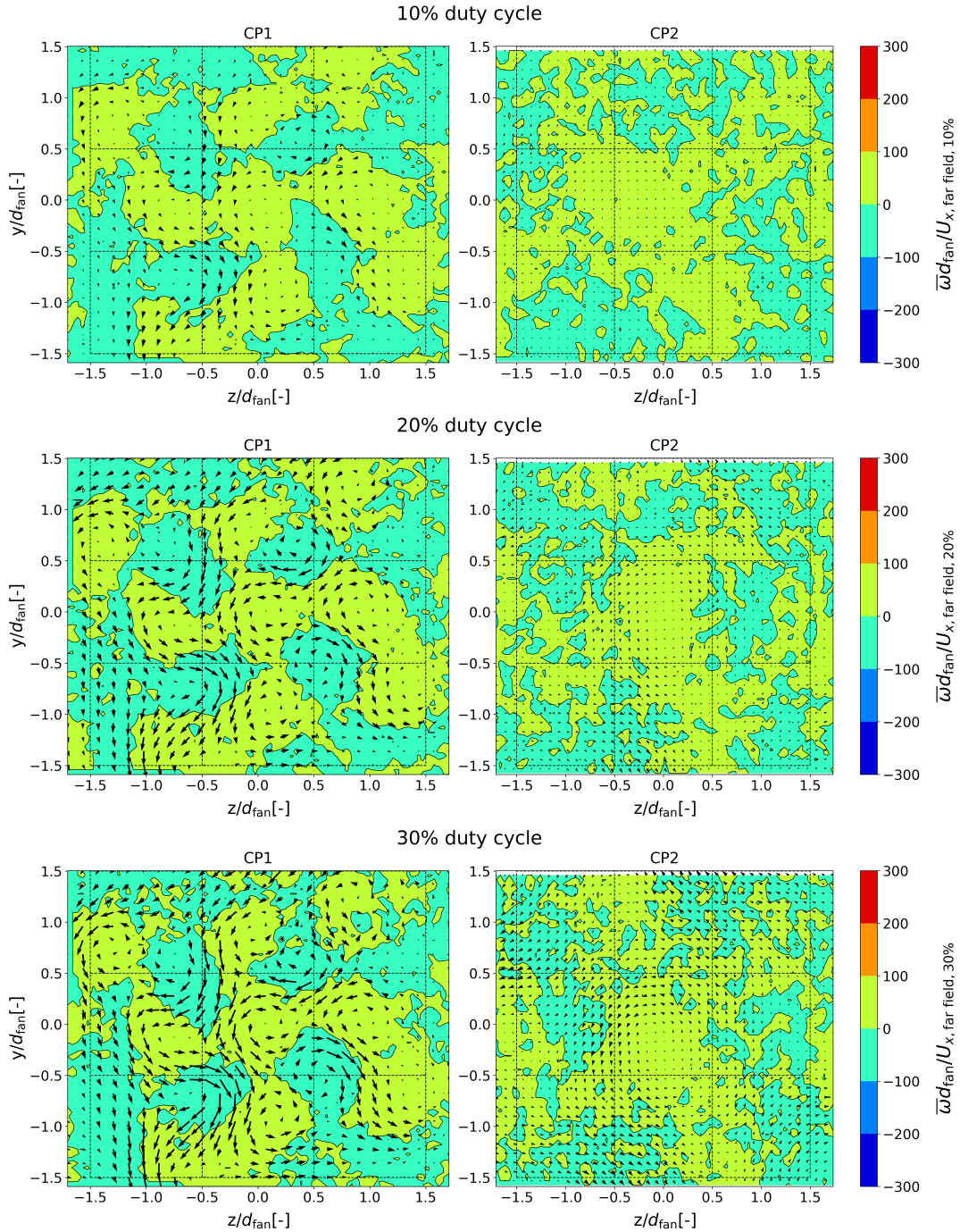


Figure D.3: Cross-stream planes colored by the mean vorticity normalized by the reference velocity, $\bar{U}_{x, far field}$, and the fan diameter, d_{fan} . The in-plane velocity vectors (scaled down by a factor of 10) are overlapped. On the left: the cross-stream plane at distance D_{MFS} downstream. On the right: the cross-stream plane at distance $2.5D_{MFS}$ downstream from the MFS. Duty cycles: 10%-30%

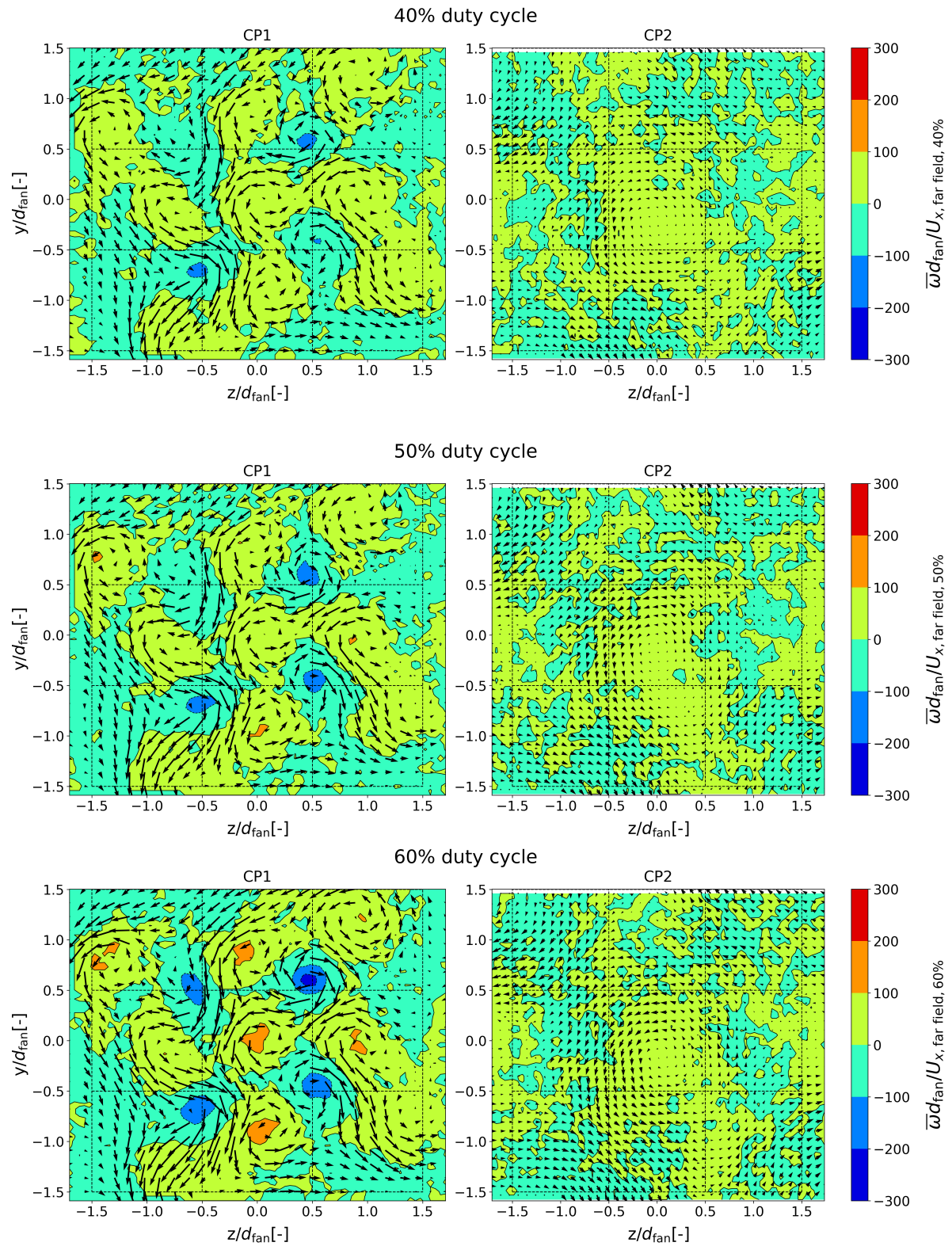


Figure D.4: Cross-stream planes colored by the mean vorticity normalized by the reference velocity, $\bar{U}_{x, far field}$, and the fan diameter, d_{fan} . The in-plane velocity vectors (scaled down by a factor of 10) are overlaid. On the left: the cross-stream plane at distance D_{MFS} downstream. On the right: the cross-stream plane at distance $2.5D_{MFS}$ downstream from the MFS. Duty cycles: 40%-60%

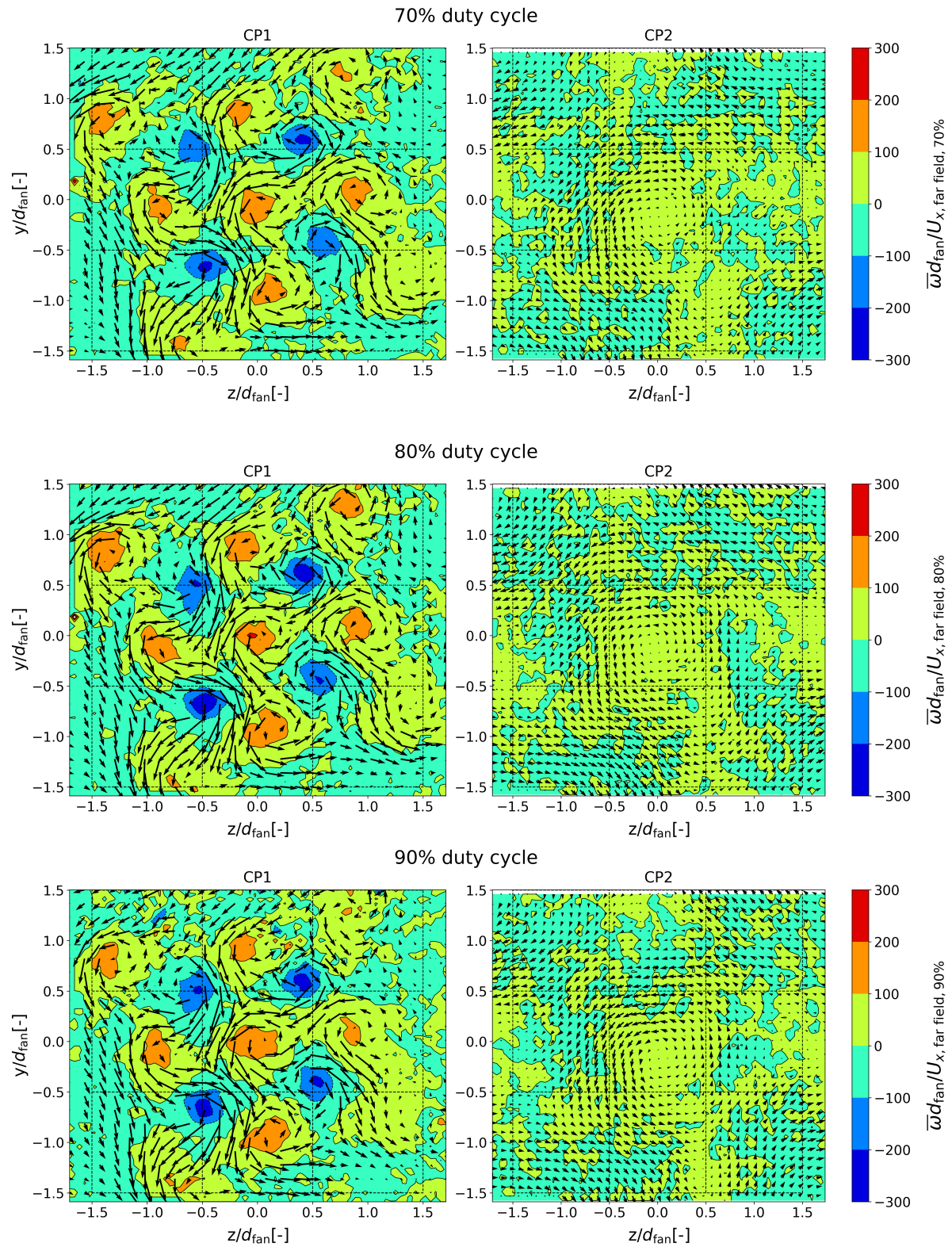


Figure D.5: Cross-stream planes colored by the mean vorticity normalized by the reference velocity, $\bar{U}_{x, far field}$, and the fan diameter, d_{fan} . The in-plane velocity vectors (scaled down by a factor of 10) are overlaid. On the left: the cross-stream plane at distance D_{MFS} downstream. On the right: the cross-stream plane at distance $2.5D_{MFS}$ downstream from the MFS. Duty cycles: 70%-90%